Turbine Passage Vortex Response to Upstream Periodic Disturbances

A thesis submitted in partial fulfillment of the requirements for the degree of

Master of Science in Mechanical Engineering

By

MITCHELL LEE SCOTT

B.S.M.E., Wright State University, 2019

2020

Wright State University

WRIGHT STATE UNIVERSITY
GRADUATE SCHOOL

December 10th, 2020

I HEREBY RECOMMEND THAT THE THESIS PREPARED UNDER MY SUPERVISION BY MITCHELL LEE SCOTT ENTITLED TURBINE PASSAGE VORTEX RESPONSE TO UPSTREAM PERIODIC DISTURBANCES BE ACCEPTED IN PARTIAL FULFILLMENT OF THE REQUIREMENTS FOR THE DEGREE OF Master of Science in Mechanical Engineering.

Committee on Final Examination

_____
Mitch Wolff, Ph.D.

_____
Rolf Sondergaard, Ph.D., PE

_____
Christopher Marks, Ph.D.

_____
Barry Milligan, Ph.D.
Interim Dean of the Graduate School

_____
Mitch Wolff, Ph.D.
Thesis Director

_____
Raghavan Srinivasan, Ph.D., P.E.
Chair, Department of Mechanical and Materials Engineering

ABSTRACT

Scott, Mitchell Lee, M.S.M.E. Department of Mechanical and Materials Engineering, Wright State University, 2020, Turbine Passage Vortex Response to Upstream Periodic Disturbances.

Flow through the turbine section of gas turbine engines is inherently unsteady due to a variety of factors, such as the relative motion of rotors and stators. In low pressure turbines, periodic wake passing has been shown to impact boundary layer separation, blade surface pressure distribution, and loss generation. The effect of periodic disturbances on the endwall flow is less understood. Endwall flow in a low-pressure turbine occurs in the boundary layer region of the flow through the blade passage where the blade attaches to the hub in the turbine. The response of an endwall vortical structure, the passage vortex, to various upstream disturbances is considered in this investigation. The passage vortex is a three-dimensional unsteady flow feature which generates aerodynamic losses as it interacts with the flow along the blade suction surface. High-speed velocimetry and numerical simulations have shown that the vortex intermittently loses coherence and varies in strength and position over time. The intermittent loss of coherence of the passage vortex is believed to be related to the leading-edge junction flow dynamics. An array of pneumatic devices was installed upstream of a linear cascade of low-pressure turbine blades to produce periodic disturbances that impact the blade leading edge region. A small disturbance and a

large disturbance were created and characterized by their maximum velocity deficit and nondimensionalized solenoid valve on time using a plane of particle image velocimetry. A plane of high-speed stereoscopic particle image velocimetry data was collected inside the blade passage to examine how the disturbances impacted the vortex. Surface-mounted hot-film data was collected near the leading edge and in passage region to help relate flow behavior in both locations. The size and frequency of the disturbances had a nonlinear impact on the vortex size and strength. Fourier analysis revealed that the actuation frequency caused a harmonic response, and a change in the temporal behavior of the passage vortex. Each actuation frequency caused a different response from the vortex, but the vortex dynamics did not lock-on to the disturbance frequency.

Table of Contents

List of Figures

List of Tables

Acknowledgments

I would like to thank my family especially my wife for supporting me throughout my academic career. I could not have done this without their help, and I owe a lot to their work. I would especially like to thank my wife for putting up with my crazy schedule and late nights while attending college.

I would also like to thank Dr. Mitch Wolff who first introduced to research after taking his Thermodynamic I course. He has provided fantastic advice as an advisor and professor on any topic I asked.

I would like to thank Drs. Christopher Marks and Rolf Sondergaard for their key input on my research and offering me the opportunity to do research at the AFRL Low Speed Wind Tunnel Facility. Dr. Marks deserves an extra special thank you for all the work he does around the lab including constantly answering my questions and offering insightful feedback on my work.

I would like to thank Nathan Fletcher for being a key resource during my time at AFRL. Nathan's thoroughness and attention to every minute detail makes him an incredible researcher.

I would like to thank Jack Chalker and Stephen Shock for helping me become the student and worker that I am today. My time spent working with these two was the happiest time of my college career. Also, I would like to thank the folks in RC21 for allowing me to work in their lab and always be willing to lend a hand.

Nomenclature

2D2C	Two-Dimensional Two-Component
2D3C	Two-Dimensional Three-Component
AFRL	Air Force Research Laboratory
AR	Aspect Ratio, Ratio of Span to Axial Chord, S/C_x
CV	Corner Vortex
C_x	Axial Chord [m]
D	Diameter, Maximum Thickness [cm]
DC	Duty Cycle, $DC = \text{Pulse Width (sec)} * f * 100$
f	Frequency [Hz]
F^+	Reduced Frequency, $F^+ = \frac{f \cdot SSL}{\overline{U_P}}$
FSTI	Free Stream Turbulence Intensity, u_{rms}/U_∞
H	Span [m]
HPT	High-Pressure Turbine
HV	Horseshoe Vortex
ILES	Implicit Large Eddy Simulation
LE	Leading-Edge
LPT	Low-Pressure Turbine
LSWT	Low Speed Wind Tunnel
M	Number of Phases
mV	Millivolt
N	Number of Samples, Number of Samples in Ensemble

p	Pressure [psi]
P	Passage
PIV	Particle Image Velocimetry
PS	Pressure Side, Pressure Surface
PSD	Power Spectral Density
PSHV	Pressure-Side Horseshoe Vortex
PTU	Programmable Timing Unit
PUG	Periodic Unsteadiness Generator
PV	Passage Vortex
Q	Q-Criterion, $Q = -\frac{1}{2}\left[\left(\frac{\partial u}{\partial x}\right)^2 + \left(\frac{\partial v}{\partial y}\right)^2\right] - \frac{\partial u}{\partial y}\frac{\partial v}{\partial x}$
Re	Reynolds Number, $Re_{Cx} = \frac{U_\infty C_x}{\nu}$
RMS	Root-Mean-Square, $RMS(x) = \sqrt{\frac{1}{n}(x_1^2 + x_2^2 + \cdots + x_n^2)}$
S	Pitch/Spacing [m]
SPIV	Stereoscopic Particle Image Velocimetry
SS	Suction Side/Surface
SSCSV	Suction Side Corner Separation Vortex
SSHV	Suction side Horseshoe Vortex
SSL	Suction side Length [m]
STKE	Secondary Turbulent Kinetic Energy
SV	Shed Vortex
T	Period [s]
t	Time [s]
TE	Trailing-Edge

Tu	Turbulence Intensity, $Tu = \frac{\sqrt{\frac{1}{2}(u_{rms}^2 + v_{rms}^2)}}{U_\infty} \cdot 100\%$
U	Velocity Magnitude [m/s]
u	Axial Velocity [m/s]
u_p	Peak Velocity Deficit [m/s]
U^*	Nondimensionalized velocity, $U^* = U/U_\infty$
U_δ	Ratio of velocity deviation from baseline case, $U_\delta = \frac{U^*_{baseline} - U^*}{U^*_{baseline}}$
v	Pitchwise Velocity [m/s]
V'	Filtered voltage by subtracting the moving mean
VITA	Variable-Interval Time Average
w	Out-of-Plane Velocity [m/s]
x	Axial Coordinate [m]
y	Pitchwise Coordinate [m]
z	Spanwise Coordinate [m]

Greek

α	Flow Angle [deg]
Δ	Difference
ρ	Density [kg/m^3]
σ	Standard Deviation
Φ	Incidence Angle
ω	Vorticity [1/s]

Subscripts

∞	Freestream/Undisturbed
avg	Average
i	Index, Index of Phase
in	Inlet Condition
j	Index of Sample in Ensemble
k	Index
max	Maximum
min	Minimum
out	Outlet Condition
ref	Reference
rms	Root-Mean-Square
s	Streamwise
t	Total
x	Axial

Superscripts

–	Overbar, Time-Averaged
~	Phase-Locked Ensemble Averaged
‘	Fluctuating Component, Secondary Coordinate

1 Introduction

1.1 Motivation

Gas turbine engines (GTEs) typically use a multishaft design with one shaft driven by a high-pressure turbine (HPT) and another shaft driven by a low-pressure turbine (LPT). The low-pressure turbine often powers a low-pressure compressor and, for a turbofan engine, the fan, or it can be connected to a drive shaft for power applications. Turbines transform fluid potential and kinetic energy to mechanical shaft work by using a series of rotor and stator blades. Rotor blades are pushed by the incoming air converting flow momentum to rotation of the shaft. Stator blades are stationary and work to expand the fluid to increase its velocity by converting potential and thermal energy to kinetic energy. The HPT is located just after the combustion chamber and typically powers the high-pressure compressor. The LPT is located downstream of the HPT, it typically powers the low-pressure compressor and fan, can amount to 30% of the total weight of an aircraft engine [36], and can possess as many as 2000 individual airfoils [37]. Current LPTs have an operating efficiency above 90%, which makes increases in efficiency using aerodynamic design incredibly difficult [38]. Instead, a focus of LPT research is on reducing the blade count per stage, which would then reduce overall weight/part count. NASA performed a system study that showed how a 10% reduction in weight of the LPT is more cost effective at reducing the direct operating cost of the engine than any other component [38].

One method to reduce the overall footprint and part count of LPTs is to increase the blade aerodynamic loading by including high lift blades. Depending on the peak loading location, high-lift blades can experience a strong adverse pressure gradient on the suction side (SS) of the airfoil due to the use of a highly curved geometry. The stronger adverse pressure gradient can result in laminar boundary layer separation in low Reynolds number flow conditions, which can increase the stall Reynolds number. By moving the pressure minimum forward on the profile, this unfavorable characteristic can be improved. Front loading at the midspan (MS) can provide better MS performance, but it can result in increased losses in the endwall region.

Secondary flow losses in the endwall region represent an important loss of efficiency in these types of turbine blades. Prakash et al. [39] analyzed the impact of loading level and distribution for LPT profile losses. Their results showed that, as the loading level increased, the peak loading moved further aft, or the Reynolds number decreased, the suction side separation and losses increased. The authors did not analyze endwall losses in their study, but they did comment that front-loaded blades typically have improved MS performance with increased secondary losses. Denton [40] found that endwall secondary flow causes approximately one-third of the loss of an axial turbine using high-lift front-loaded blades. Sharma et al. [41] found endwall losses to be between 30-50% of the total loss, which agrees with a review conducted by Langston [30].

With high-lift front-loaded blade geometry offering superior MS performance and potential system level benefits, investigating ways to decrease endwall losses has been heavily researched [2-4,42]. These investigations all used steady inlet flow conditions in their experiments, but flow through an actual LPT is unsteady due to the relative motion

of rotors and stators and the high levels of incoming turbulence. Researchers have started to incorporate unsteady flow conditions into experimental and numerical studies of endwall flows and loss generation [20, 43-45]. This topic still has large knowledge gaps especially surrounding the relationship between the LE junction and secondary flow behavior. A deeper understanding of the impact of upstream on endwall flow physics and loss generation is needed to thoroughly describe flow phenomena in the LPT endwall.

1.2 Background

1.2.1 Junction and Secondary Flow Description of a Low-Pressure Turbine

"Junction flows occur when a boundary layer encounters an obstacle attached to the same surface" Simpson [5]. The resulting effect causes horseshoe-vortices (HVs) to roll up in front of the LE that extend on either side of the barrier. In low-pressure turbines, this junction flow occurs at the LE junction with the endwall. The pressure gradients around the blade produce an upstream separation creating a three-dimensional HV that wraps around the blade and extends into the passages on both sides of the blade. The primary flow features for secondary flow consist of the passage vortex (PV), the HV, and a corner vortex [47]. These flow features are strongly influenced by the blade geometry, blade loading, load distribution, and by the inlet boundary layer [12]. Additional vortical structures are present for different types of blade geometries.

Significant research has been devoted to better characterizing and understanding junction and secondary flows. Davenport and Simpson [6] thoroughly analyzed junction flow for a turbulent boundary layer encountering a cylindrical wing. Both Wang et al. [28] and Sharma [14] provided an in-depth analysis of the turbine secondary flowfield, which largely agree with the formation of the horseshoe vortex (HV), the passage vortex (PV), a

counter-rotating corner vortex (CV), and shed vortices. Differences in their results were largely centered on flow features along the SS of the blade. These are likely caused by differences in the experimental configuration of the wind tunnels, specifically the blade geometries.

A description of the endwall flow based on the high-lift front-loaded L2F blade is provided. One leg of the HV extends along the suction surface of the blade, and it forms the suction side HV (SSHV). The SSHV dissipates near the mid-chord point, but the other leg of the HV extends towards the pressure-side and forms the pressure-side HV (PSHV). Under the influence of the passage pressure gradient, the PSHV extends across the blade passage from the PS near the LE to the SS at the TE and is strengthened by secondary flow forming the passage vortex (PV). Eventually, the PV lifts-off from the endwall. Along the SS, the strong corner separation forms the Suction Side Corner Separation Vortex (SSCSV), which has the same rotation as the PV (clockwise). The corner vortex (CV) is an additional vortical structure present in the endwall region, and it has the opposite sense of rotation to the PV (counterclockwise). High shear near the SSCSV region forms the shed vortex (SV). Figure 1.1 shows ILES data that helps to visualize these vortical flow structures [29].

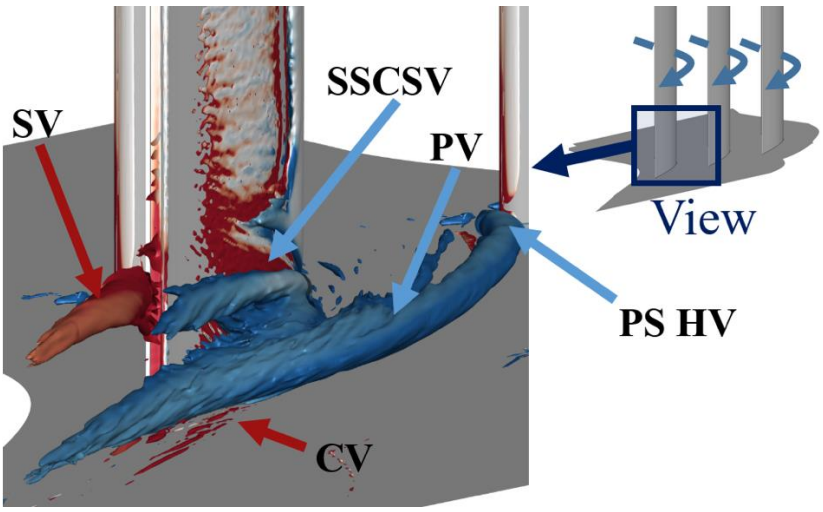

Figure 1.1 ILES results that depicts the vortical flow structures in the endwall region of L2F LPT blades at $RE_{Cx} = 100,000$. Isosurfaces of Q-criterion=1 with blue regions representing clockwise rotation and red regions represent counter-clockwise rotation [29].

Previous investigations have found that the HV has a bimodal behavior with a backflow mode and a zero-flow mode [7-9]. The backflow mode is characterized by negative values of streamwise velocity at the wall-body junction, and the zero-flow mode is characterized by near-zero values of stream velocity at the wall-body junction. The two modes have slightly different spatial locations representing an inherent instability frequency that can be utilized and studied. Veley et al. [25] used surface-mounted hot-film sensors to measure the unsteady characteristics of endwall vortices, namely the PV. The PV is one of the most significant secondary flow features in the turbine passage. They acquired concurrent hot-film and flow visualization data that helped identify a link between the PV moving towards the SS and a loss of strength and coherence of the PV. Gross et al. [9] hypothesized that the intermittent loss of coherence of the PV is caused by the bimodal behavior of the HV, and that the LE junction flow impacts the unsteady behavior of the PV. Secondary flow through a high-lift front-loaded L2F LPT blade contain multiple complex vortical structures with a possible link to the LE junction.

1.2.2 Unsteady Turbomachinery Environment

The main cause of periodic unsteadiness in LPTs is relative motion between adjacent rotors and stators, all of which shed wakes. Periodic wakes impact the boundary layer, surface pressure, loss generation, flow angles, and secondary flow. Research in this area has primarily focused on analyzing the impact of periodic wakes on the MS flow. Hodson and Howell discuss blade boundary layer transition in the context of blade row interactions for high-lift airfoils in LPTs [11]. Periodic unsteadiness can increase or decrease profile losses depending on the Reynolds number, pressure distribution, wake passing frequency, and wake strength.

Mechelassia et al. conducted a computational investigation using Direct Numerical Simulations of the flow through a linear cascade that included a simulated bar wakes at multiple Reynolds numbers, background turbulence levels, and reduced frequencies [31]. Their results determined that the wakes either reduced the size of laminar separation bubbles or completely suppressed them altogether, but the reduction in separation bubble size was dependent on the Reynolds number and reduced frequency. Additionally, the highest reduced frequency tested essentially increased the background turbulence because the wakes merged before having a noticeable effect on the boundary layer. Schobeiri et al. performed hotwire measurements along the SS of highly-loaded LPT blades [33]. They found passing wakes elicited a periodic contraction and expansion of the separation bubble and reduced the separation bubble height. As the wake passing frequency increased, it increased the turbulent kinetic energy that resulted in suppression of a strong separation bubble. Volino et al. [32] investigated boundary layer separation on high-lift LPT blades

and found that wakes caused separation to largely be suppressed, especially for large passing frequencies. For lower frequencies, the boundary layer separated between wakes.

Steurer et al. [45] performed experiments investigating the effect of endwall boundary layer thickness on losses in a LPT cascade using L2F blades and unsteady wakes. Their results showed a direct correlation between the size of the inlet boundary layer and the size of the PV/associated endwall losses. Unsteady wakes could have positive or negative effects on the endwall and MS losses. The results were heavily dependent on the characteristics of the BL. Ciorciari et al. [12] used experimental and numerical tools to investigate how unsteady wakes affected secondary flows in a linear turbine cascade. Their data showed a periodic reduction of the PV strength, TE wake, and corner vortices, and a link between higher wake passing frequency to a more significant reduction in the secondary vortex strength. Gross et al. [27] used ILES simulations of a low-pressure turbine stage of L2F airfoils to understand how the relative rotor-stator interaction impacts performance. They found that the wakes shed from the upstream vanes sweep over the SS of the downstream blades, suppress laminar separation away from the endwall, and curb the formation of the HV. Fletcher et al. [20] used a periodic unsteadiness generator (PUG) to study the effect of various disturbances on the dynamics of the passage vortex. The temporal response of the PV in a low-speed linear cascade passage was studied using high-speed stereo PIV. They found that the PV's strength decreased as reduced frequency was increased from 0.2 to 0.6. Previous research has investigated and hypothesized multiple factors that can influence the secondary flow characteristics including the BL size, wake passing frequency, and LE junction flow.

1.3 Purpose

The overall purpose of this research is to develop a fundamental understanding of how upstream periodic unsteadiness impacts the secondary flow in a linear cascade. High-lift front-loaded blade geometries like the L2F produce complex flowfields with multiple vortical structures. Vortical structures especially along the SS are heavily dependent on the type of blade used. Previous work heavily analyzed the MS flow region with the effects of unsteadiness, and researchers have hypothesized what upstream characteristics can influence the secondary flow. They have hypothesized the relationship of BL size, wake passing frequency, and LE junction flow as methods of controlling the secondary losses for high-lift front-loaded blades. This study used a pneumatic periodic unsteadiness generator (PUG) to create multiple disturbances with different velocity deficit, turbulence intensities, and spanwise vorticity characteristics that impact the LE junction flow. The goal of this work was to develop a deeper understanding of how the characteristics of each disturbance can change the secondary flow behavior by analyzing one its prominent vortical structures: the passage vortex. The PUG used solenoid valves to pulse air out into the freestream that form each disturbance. Frequency and duty cycle (DC) settings control the size and shape of the disturbance. Disturbance frequencies of 0.41, 0.85, and 1.25 were utilized to investigate how frequencies impact the secondary flow of a low-pressure turbine cascade. Disturbance frequencies above and below one presented an interesting concept to study since a new disturbance will enter the blade passage in close proximity to the previous disturbance exiting. Disturbance frequencies greater than one were expected to cause multiple disturbances to exist inside the passage at any given time and decrease the amount of time for the LE junction to recover between disturbances. The disturbance

frequency of 0.85 case provided more time for the LE junction to recover between disturbances, but multiple disturbances were not expected to be found in the blade passage at any given time. A disturbance frequency of 0.41 provided more time for the LE junction to recover between disturbances, and a greater time delay for disturbances impacting the secondary flow. Two disturbances magnitudes were created, each with a disturbance duration less than one convective time. One size disturbance was used to investigate whether a small amplitude disturbance could influence the behavior of the PV. The other disturbance had a larger amplitude and a longer disturbance duration to examine a more forceful approach. Each disturbance was characterized using 2D2C PIV upstream of the blade LE and downstream of the pneumatic periodic unsteadiness generator (PUG). Each disturbance was characterized based off the on-time of the solenoid valves, which should all closely match for each frequency based on the size of the disturbance. To analyze how the disturbance impacted the temporal response of the PV, a plane of high-speed SPIV was captured in the blade passage. Additionally, hot-film sensors were installed upstream of the LE and downstream of the SPIV plane to help further analyze how the disturbances influenced the junction flow and PV. This type of measurement provides insight into how the LE junction flow region is related to the secondary flow inside the passage.

2 Experimental Setup

2.1 Wind Tunnel Configuration

All experiments presented were conducted in the Air Force Research Laboratory's (AFRL) Low Speed Wind Tunnel (LSWT). The wind tunnel was configured as an open loop seven blade LPT linear cascade with an upstream splitter plate to develop a clean and controllable inlet boundary layer. At the tunnel inlet, a honeycomb flow straightener minimizes the lateral velocity components caused by the swirling motion of air entering. Figure 2.1 shows an overhead view of the wind tunnel configuration. Upstream of the splitter plate, a turbulence grid increases the free-stream turbulence intensity (FTSI) to 3.0%. A variable speed motor connected to an axial fan downstream of the test section sets the air's velocity through the test section. The seven blades installed in the LSWT are high-lift, front-loaded L2F blades designed at AFRL [18]. Specific parameters describing the linear cascade and experimental conditions can be found in Table 2.1, and Figure 2.2 shows an overhead view of the linear cascade wind tunnel. A Reynolds number of 50,000, based on the incoming flow velocity and the axial chord length (C_x), was used for all of the experiments. A pitot-static probe located $2C_x$ upstream of the blade row connected to a 0-

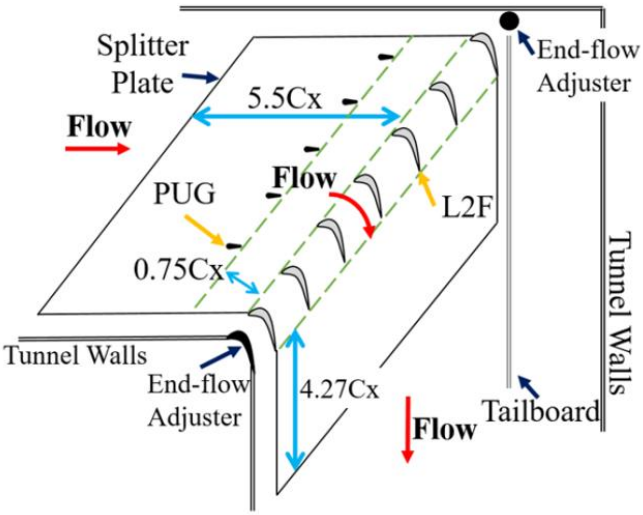

Figure 2.1 Overhead view of test section with PUGs installed

0.4 inH2O Druck pressure transducer was used to measure the incoming dynamic pressure to calculate the Reynolds number.

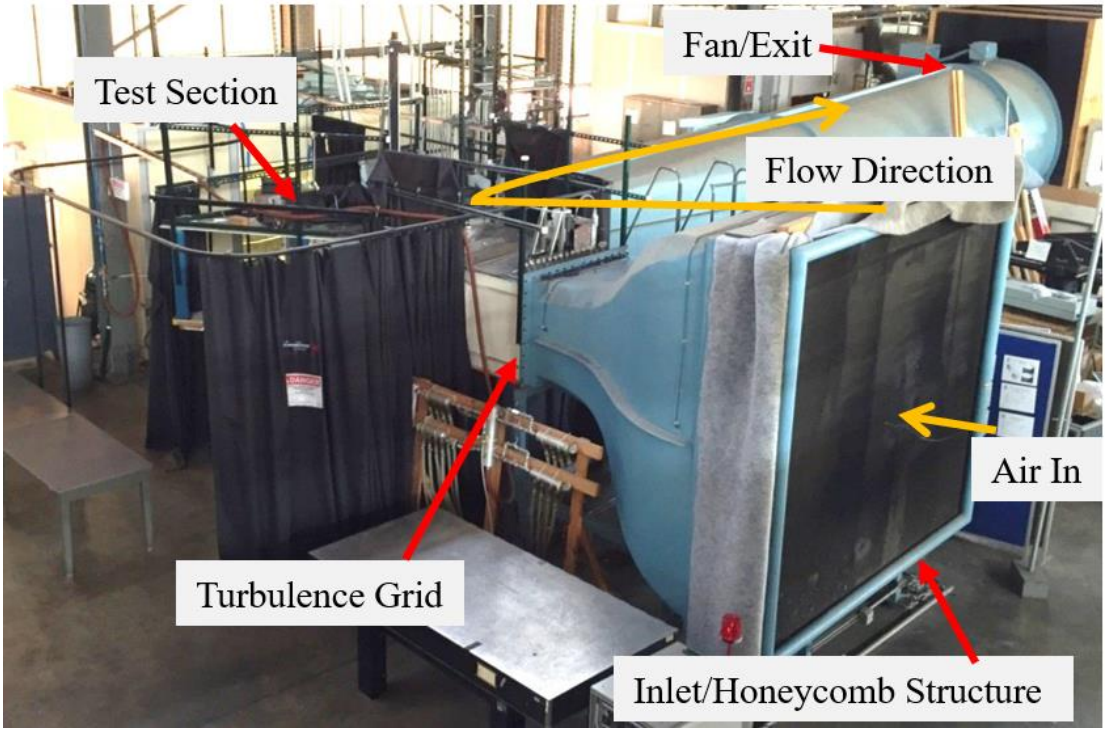

Figure 2.2 Overhead view of the linear cascade wind tunnel

Table 2.1 Linear cascade parameters and experimental test conditions

Axial Chord, C_x	15.24 cm
Pitch/Axial Chord, S/C_x	1.221
Span/Axial Chord, H/ C_x	4.17
Inlet Flow Angle (from axial), α_{in}	35°
Mean Profile Exit Angle [46], α_{ex}	-58°
FSTI	3.0%
Zweifel Coefficient, Z_w	1.59
Reynolds Number, Re_{Cx}	50,000

2.2 Periodic Unsteadiness Generator (PUG) Configuration

Previous work examined how upstream unsteadiness generated from a new periodic unsteadiness generator (PUG) impacted the secondary flow [20]. The PUG is a stationary pneumatic device that periodically ejects compressed air upstream of the blades at user-controlled frequencies and duty cycles. Using this design provides significant advantages over a full moving wake generator; specifically, minimal footprint in the wind tunnel, preservation of the incoming boundary layer, ease of adjusting pulsing characteristics, and ease of incorporating the device into the wind tunnel.

The PUG was designed to create disturbances that simulate the effect of periodic wake passing produced by the relative motion of rotors and stators in a turbine. These disturbances are characterized by velocity deficit, vorticity, turbulence intensity, and momentum deficit. The disturbances generated by the PUG are most appropriate for fundamental studies of the unsteady endwall flow dynamics because they were not designed to exactly simulate the wake passing characteristics in LPTs. The PUGs were placed in the same locations as described in Ref. 20. This placement allows the disturbances to convect downstream and perturb the flow near the LE region of the blades.

Figure 2.3a shows the CAD model of the PUG, and 2.3b shows its placement relative to the blade LE. In total, five PUGs were placed upstream of the five innermost blades in the LSWT. A 3-D printed streamlined plastic body joins the LE and TE jet arrays. The PUG LE pulsed jet consists of a tube-in-tube design that ejects air at a controlled angle relative to the incoming flow. The tube-in-tube design creates a small cavity that helps create a more uniform jet outlet distribution. Compressed air is fed into both ends of the

tube, and the flow is actuated using solenoid valves. When the solenoid valves pulse, compressed air is ejected into the incoming flow creating a region of reduced velocity and increased turbulence. To fill in the trailing edge wake produced by the stationary device and minimize its downstream impact when the pulse is off, a row of steady jets were placed at the trailing edge of the PUG. These steady jets also mitigate vortex shedding downstream of the device. This concept has been proven in previous research studies [21-23]. The jets are linearly spaced on the TE and LE to eject air only in the spanwise, or vertical direction in an even distribution. Table 2.2 shows a breakdown of the PUG's dimensions and characteristics. In this study, the jets between 0.25H and 0.75H were not used. Even though a section of the jets remained unused, the jets still impact all of the 3-D portion of the turbine passage flow, and a portion of the blade's 2-D flow. This arrangement was acceptable, as the linear cascade had a large aspect ratio (4.17), and the mid-span flow suction surface boundary was not fully separated at the flow Reynolds number used in the study. Because of the device placement, the profile wake produced by the unused section had a minimal effect on the flow.

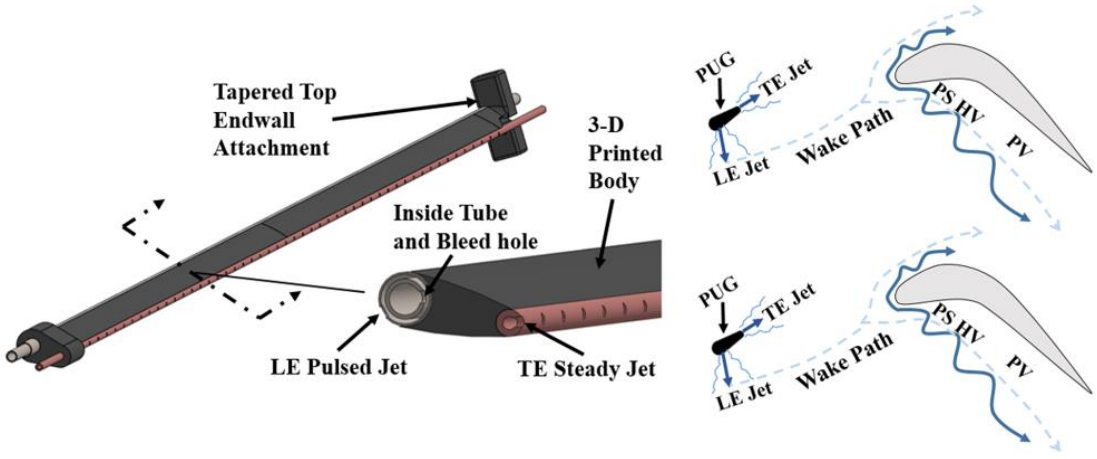

Figure 2.3 a) CAD model of PUG and b) overhead view of PUGs installed in LSWT with approximate streamline of its disturbances propagating downstream into the passage [20]

Table 2.2 PUG dimensions and characteristics

LE Jet Hole Spacing/C_x	0.083	TE Tube OD/C_x	0.021
TE Jet Hole Spacing/C_x	0.083	TE Tube ID/C_x	0.010
Jet Hole Diameter/C_x	0.011	PUG Spacing/C_x	1.221
LE Outside Tube OD/C_x	0.042	PUG TE Upstream Distance/C_x	0.75
LE Outside Tube ID/C_x	0.038	LE Jet Blowing Angle	250°
LE Inside Tube OD/C_x	0.031	PUG Chord/C_x	0.119
LE Inside Tube ID/C_x	0.025	PUG Span/C_x	4.17

2.3 Unsteady Disturbance Characterization

2D2C PIV measurements were used to characterize the disturbances created by the PUG. Fig. 2.1 shows an overhead view of the test section with the five PUGs installed $0.75C_x$ upstream of the blade row. Fig. 2.4 shows the location of the 2D2C PIV plane. The location between the PUG and blade allows for optimal visualization of the disturbance leading into the blade passage and the impact of the PUG's profile on the flow. The plane was parallel to the endwall at $z/H = 0.089$. A Quantel EverGreen 200 laser with sheet-forming optics illuminated the seeding particles. A LaVision Imager sCMOS camera with an 85 mm lens and 532 nm bandpass filter positioned on top of the LSWT test section captured the seeding particles moving through the plane. A bandpass filter was used to attenuate ambient illumination to improve the accuracy of the measurement. Software from DaVis and a LaVision programmable timing unit (PTU) synchronized firing the laser and capturing images. The measurements were phase-locked with the signal driving the solenoid valves and averaged using at least 2,000 images. The software also performed a spatial calibration and perform post-processing of the data. The PIV images were post-

processed using a first pass 64x64 interrogation window and a final pass 32x32 interrogation window with 50% overlap. A study determined the optimal time between successive images was 90 µs. This delay allows for an acceptable amount of pixel shift for the flow speed and optical setup to capture good quality PIV data.

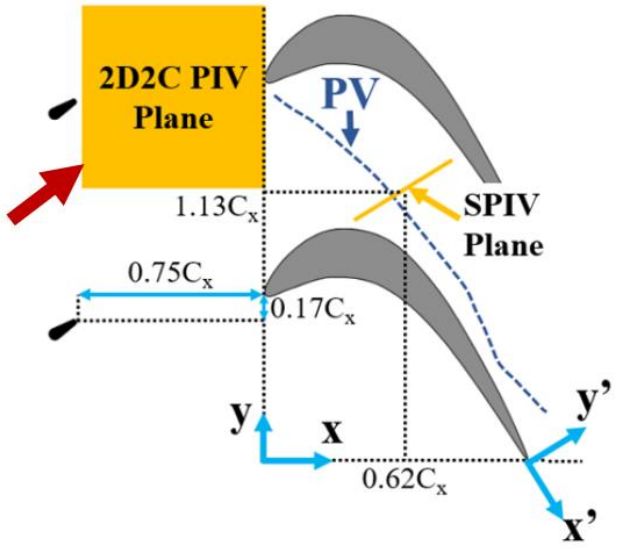

Figure 2.4 Overhead view of 2D2C PIV plane location

The pulsing frequency of the PUG dictates the number of disturbances produced over a given time period. The reduced frequency (F^+), Equation 2.1, nondimensionalizes the frequency by using SSL, the suction side length, and $\overline{U_p}$, the average velocity through the passage, to approximate the average convective time through the blade passage. A convective time of one represents the mean amount of time it takes for flow to enter and exit the blade passage at MS. A reduced frequency larger than one means a disturbance will enter the passage before the previous disturbance completely leaves the passage. Equation 2.2 shows the calculation of nondimensionalized time, which is the inverse of the reduced frequency.

$$F^+ = \frac{f \cdot SSL}{\overline{U_P}} \tag{2.1}$$

$$T^+ = \frac{t \cdot \overline{U_P}}{SSL} \tag{2.2}$$

All velocities were nondimensionalized using the inlet free-stream velocity, shown by Equation 2.3, which helps normalize the velocity measurements. Wakes are commonly characterized by their velocity deficit on the flow, shown by Equation 2.4. Velocity deficits represent regions where the flow velocity is lowered. The high velocity gradient present near the LE causes difficulty in analyzing how the disturbance impacts the velocity in this region. To isolate the impact of the disturbance on the velocity, a new flow parameter was created: U_δ shown by Equation 2.5. U_δ normalizes the velocity to isolate the difference in velocity caused by the disturbance. A positive U_δ value corresponds to a velocity deficit, and a negative U_δ corresponds to a positive velocity change.

$$U^* = U/U_\infty \tag{2.3}$$

$$V_{def} = 1 - U^* \tag{2.4}$$

$$U_\delta = \frac{U^*_{baseline} - U^*}{U^*_{baseline}} \tag{2.5}$$

At each frequency, the number of disturbances impacting flow near the LE and in the passage differs as a function of time. Since each frequency should produce a similar disturbance, the duration of the disturbance event is also of importance and was characterized for each condition considered.

2.4 Endwall Flow Study

High-speed PIV was used to study the temporal behavior of the vortex in the passage. Figure 2.5 shows the location of the PIV plane. In-passage high-speed velocimetry measurements used a Photonics Industries DM30 Dual Head 527 nm laser (Nd:YLF) with sheet-forming optics was used to illuminate the seeding particles. The laser was placed below the test section and fired upwards into the passage of the linear cascade passing through two ½ inch acrylic walls. Two Phantom VEO 640L cameras with 180 mm lenses and Schleimpflug adapters were placed on the sides of the wind tunnel to image the illuminated seeding particles. The cameras were calibrated and the laser-sheet was aligned with the secondary coordinate system (x', y'). The stereo viewing angles to the measurement plane were 28° and 233°. The secondary coordinate system is relative to the exit flow angle, shown by Figure 2.5. Figure 2.6 shows the camera setup for this measurement. Two calibration methods were used for this setup. The pinhole calibration method for spatial calibration was used to identify spatial relationships between the cameras and the calibration plate, the RMS of fit was 0.32 and 0.28 with a scale factor of 14 pixel/mm. The polynomial calibration was used for the spatial calibration in the experiment because it offered higher accuracy for this setup.

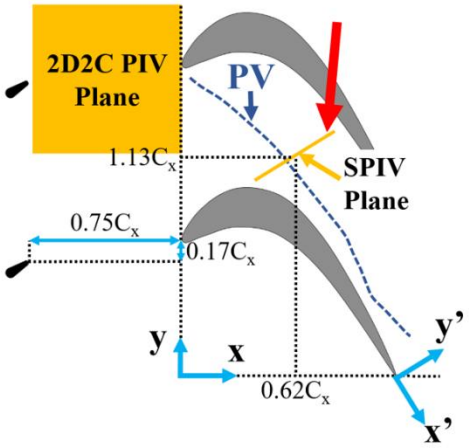

Figure 2.5 Overhead view of the SPIV Plane

a. b. c.

Figure 2.6 Location and setup for SPIV measurements for a) camera 1 looking upstream behind opaque cover, b) camera 2 looking downstream, and c) the calibration plate mounted in the target area

The PIV measurements were used to calculate the instantaneous and time-averaged Q-criterion in the two-dimensional measurement plane. Q-criterion is one method of locating vortices by identifying areas where the magnitude of rotation is greater than the magnitude of rate-of-strain. Equation 2.6 presents the equation for Q-criterion in two-dimensions. Large values of Q-criterion signify regions of strong rotation and vortical flow. The measurement plane was positioned through the blade passage normal to the endwall to capture positional and strength changes of the vortex over time.

$$Q = \frac{1}{2}\left[\left(\frac{\partial u}{\partial x}\right)^2 + \left(\frac{\partial v}{\partial y}\right)^2\right] - \frac{\partial u}{\partial y}\frac{\partial v}{\partial x} \tag{2.6}$$

For image acquisition, the first rising edge of the signal driving the PUGs, generated using LabVIEW software and a National Instruments (NI) BNC-2120 triggered the PIV acquisition system. The sampling frequency was chosen to be a multiple of the PUG pulsing frequency to ensure an even number of phases were captured per second of data acquisition, which allows phase averaging. Table 2.3 shows the PUG pulsing frequency

with the SPIV camera sampling frequency and number of acquired images (each set was limited by camera memory).

Table 2.3 PUG pulsing frequency with SPIV sampling rate and number of acquired images

F^{+}_{PUG}	f_{PUG}	f_{samp} (Hz)	Acquired Images
0	0	1500	8000
0.41	11	2508	15048
0.85	23	2507	15042
1.25	35	2485	14910

The variable-interval time average (VITA) method by Blackwelder and Kaplan [15] was used in this study to detect vortex loss of coherence events using the high-speed velocity data. Loss of coherence can be described as instances of time during which the vortex coherence quickly dissipates. The events have been previously observed and described using high-speed SPIV [20,26]. The VITA method was originally Tardu [16], Kim [17], and Gross [18] utilized the VITA method to detect bursting events in the turbulent boundary layer. Lu [19] applied the VITA method to help identify bursting events in hairpin vortices. Equations 2.7-9 were used for the VITA analysis.

$$\hat{Q}(t,\tau) = \frac{1}{\tau}\int_{t-\tau/2}^{t+\tau/2} Q(\eta)\, \boldsymbol{d}\eta \tag{2.7}$$

τ is the window size. This formulation creates a low-pass filter with $1/\tau$ acting as the cutoff frequency. The variance for the variable-interval time averaged Q can be calculated using Equation 2.8.

$$\widehat{var}(t,\tau) = \hat{Q}^2(t_1,\tau) - \left[\hat{Q}(t,\tau)\right]^2 \tag{2.8}$$

Using Equations 2.7 and 2.8, the VITA detection function is shown below as Equation 2.9.

$$\mathrm{VITA}(t) = \begin{cases} 1 & \text{if } \widehat{var} > k \cdot \mathrm{RMS}(Q) \\ 0 & \text{otherwise} \end{cases} \tag{2.9}$$

The parameter k was a user-selected factor for the root-mean-square of N of the threshold criterion. Additional filtering of detections was applied to improve the results. One stipulation was that loss of coherence events only occur when dN/dt is negative. Additionally, the vortex strength had to be less than $\varepsilon \cdot \sigma$ from the mean tracked Q-criterion. ε is a user-defined factor multiplied by the standard deviation, σ, to establish a threshold for the vortex's strength. These additional conditions were intended to filter out false-positive loss of coherence events. Values of user-defined variables used in this study changed with each case. They were adjusted until the detection points corresponded with loss of vortex coherence events. An example of this process is shown by Figure 2.7 where a space-time plot of the isosurfaces of Q=100 is used to visualize the PV, and red bars indicate VITA detections.

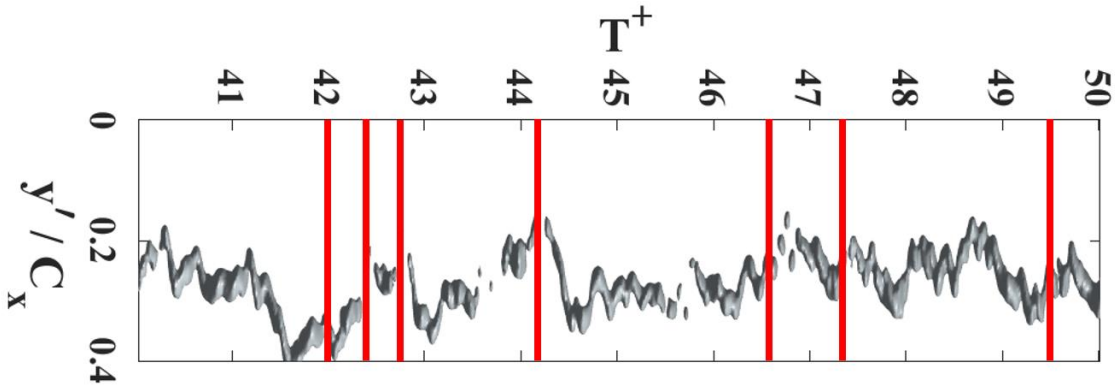

Figure 2.7 Space-time plot of the isosurfaces of Q=100 from $T^+ = 40 - 50$ that includes VITA detection points (shown by red vertical lines)

In the example presented in Figure 2.7, the VITA method produced 7 detections. The algorithm works to find times when the Q-criterion value suddenly decreases

substantially, which should signify a loss of coherence event. After the initial detection, any behavior within a threshold of at least 0.2 convective times is associated with that detection and will not trigger another detection. If the Q-criterion increases during that threshold period, and then suddenly decreases outside of that period, the algorithm will trigger another detection. This characteristic is responsible for the three successive detections between $T^+ = 42$ through 43. The next three detections, from $T^+ = 44$ through 48 all capture loss of coherence events. The final detection, occurring at $T^+ = 49.5$, is considered a false detection. The space-time isosurface shows the PV very briefly decrease in strength and lose coherence, but this is likely an artifact of the quality of the Q-criterion signal. False-positive detections are a part of using the VITA method, and they are present even after tuning k and ε. The number of false positive detections were substantially reduced by modifying those user-defined constant iteratively and checking plots like Figure 2.7 to ensure accurate results. False negatives are also an aspect of the VITA method that can influence its results. Two false negatives were detected in based off Figure 2.7: one at $T^+ = 43.5$ and the other at $T^+ = 45.5$. The VITA method failed to detect either of these brief loss of coherence events. The conditions put in place to reduce/eliminate false-positive results are likely influencing the VITA method here resulting in false-negatives.

Modifying k and ε was key towards producing reliable results. k must be between 0 and 1, but ε is not restricted to any finite scale. For this analysis, increasing k decreases the amount of VITA detections because it specifically needs a low variance of the Q-criterion to identify a detection. Decreasing k allows for more detections because the variance can be larger. Similarly, ε decreases the number of VITA detections as it increases. Increasing ε requires a lower Q-criterion value for a VITA detection.

Space-time plots were generated using isosurfaces of $Q = 100$ to help visualize the PV. These plots were created by utilizing multiple filtering techniques to provide a clearer image of the PV. First, the possible locations of the isosurfaces is restricted based on the location of the maximum Q-criterion detected to eliminate any noise or outliers across the plane. Secondly, a strength criterion that the Q-criterion must be at least 100 to appear on the plot helps eliminate smaller vortices in this region. These parameters were used to track the PV and output its approximate profile to produce plots similar to Figure 2.7.

2.5 Surface-Mounted Hot-films

Surface-mounted hot-films allows for non-intrusive measurements of the flow, they are can be attached to any smooth surface, and they can be synchronized with other measurements. These sensors are useful in identifying unsteady flow signatures near the LE and tracking propagation through the blade passage. With the PUG, these sensors can be used to confirm disturbances at the LE and assess how the disturbance changes the fluid behavior in the passage. Previous research [25] used the IFA 300 and read the surface-mounted hot-film as a voltage signal, which caused limitations on the number of hot-films that could be read synchronously. Technical issues with the IFA 300 limited the number of hot-films measurements occurring simultaneously and reliably receiving data. Therefore, a new method of acquiring surface-mounted hot-film data was pursued by using the NI PXIe-4330/4331 bridge module.

The NI PXIe-4330/4331 bridge module provides 8 simultaneously sampled input channels interfaced with a Wheatstone bridge-based sensors and integrated signal conditioning. The NI module utilized had a 120 Ω quarter-bridge completion resistors. For optimal performance, the hot-film sensors were designed for temperature effects to dominate the measurements to capture velocity behavior using the same principles as a standard hotfilm/wire. A constant voltage was applied across the sensor with the current to maintain a constant temperature for the sensor. When the fluid velocity near the sensor increases, heat transfers from the sensor to the fluid, which requires a higher current to maintain the constant temperature. For this study, the three sensors were placed upstream of the LE, denoted by EW2, and six were installed downstream of the SPIV plane, denoted by EW4. Figures 2.8 and 2.9 show the placement of these sensors. EW2 sensors were installed so that they matched the angle of the PS blade to form a smooth transition. EW4 sensors were placed 10 millimeters downstream of the SPIV plane because the laser pulses caused a noticeable signal in the hot-film measurements. To also combat this problem, black tape was placed on the plexiglass sheet under the hot-films without protruding into the SPIV plane to block the laser energy. Figure 2.9a shows the hot-film placement at EW2 and Figure 2.9b shows the hot-film placement at EW4 and the calibration plate that was placed in the high-speed SPIV plane. The sensor portion of the hot-film is marked by the yellow arrow, and the rest

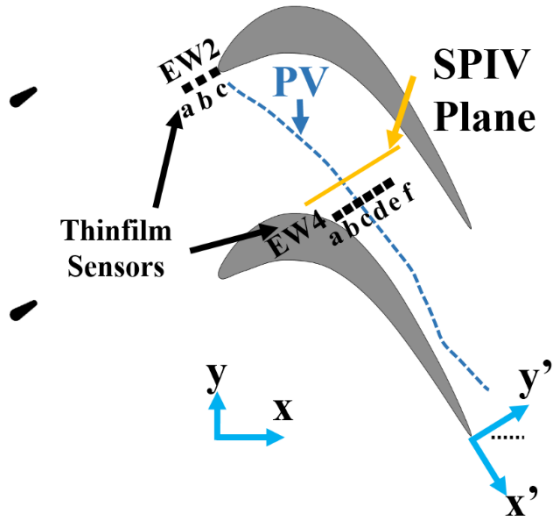

Figure 2.8 Overhead view of the Hot-film sensor placement

of the hot-film contains the wire leads connected to the sensor. Two thin wires connect the sensor to a BNC cable, and these are fastened to the splitter plate by using Kapton tape. Table 2.4 shows the sensor location in the secondary coordinate system.

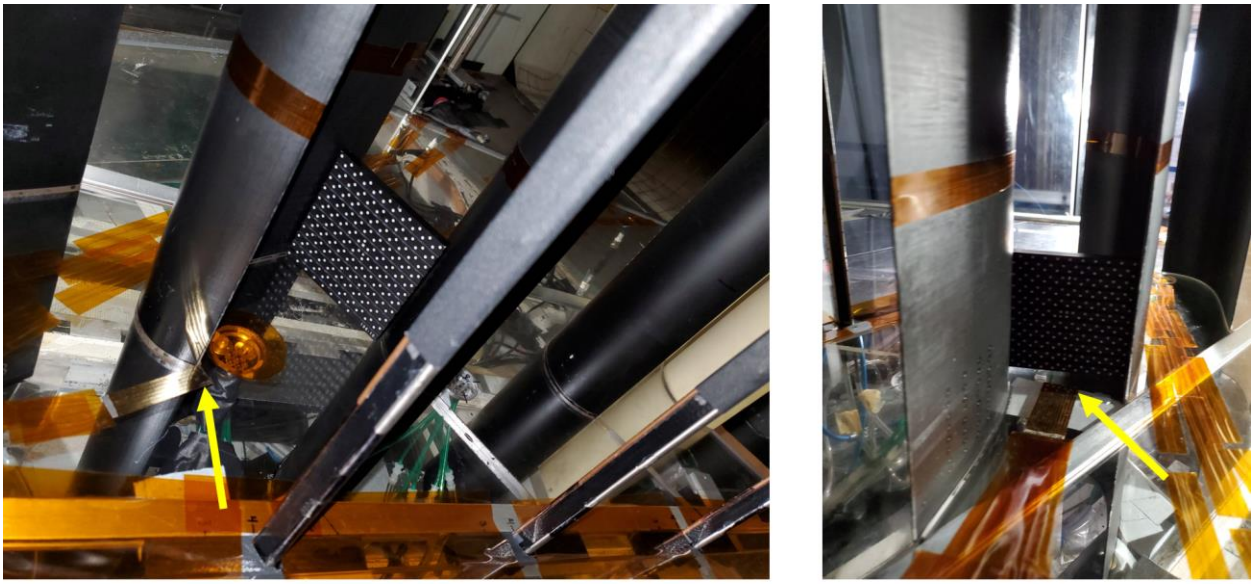

a) b)

Figure 2.9 Hot-film location in linear cascade at a) EW2 and b) EW4 positions

Table 2.4 Sensor location in secondary coordinate system

Sensor Name	x'/C_x (mm)	y'/C_x (mm)
EW2a	325.5	21.1
EW2b	323.8	16.8
EW2c	322.1	12.5
EW4a	161.4	33.5
EW4b	161.4	38.5
EW4c	161.4	43.6
EW4d	161.4	48.7
EW4e	161.4	53.8
EW4f	161.4	58.9

The LabVIEW program can sample eight hot-film sensors and one voltage signal, which was used to synchronize the hot-film measurements with PIV, or, in this case, SPIV by sampling one of the Camera's Trigger lines. Only the Camera Trigger line could be used for this analysis because the Camera Clock and Laser signals capture signals before and after image acquisition. With the Camera Trigger line, it transmits one pulse that starts the beginning of the acquisition sequence. Because this pulse has an incredibly small period, this voltage signal had to be sampled at 1MHz to ensure the signal was captured. As the voltage signal for the SPIV is being sampled, the hot-film channels are also recording data at a rate of 20 kHz. Both types of signals were sampled for ten seconds. Figure 2.10 shows the Camera Trigger line with the peak corresponding to when the SPIV setup started taking data. Some technical issues occurred with a tee installed with the Camera Trigger line directing one lead to the camera and the other lead to a BNC-2090A. No problems occurred with the hot-film measurements, but sampling the Camera Trigger line did have an impact on the timing behavior of the camera. The camera was not able to sample the images at the specified rate for initial testing, but this issue resolved itself.

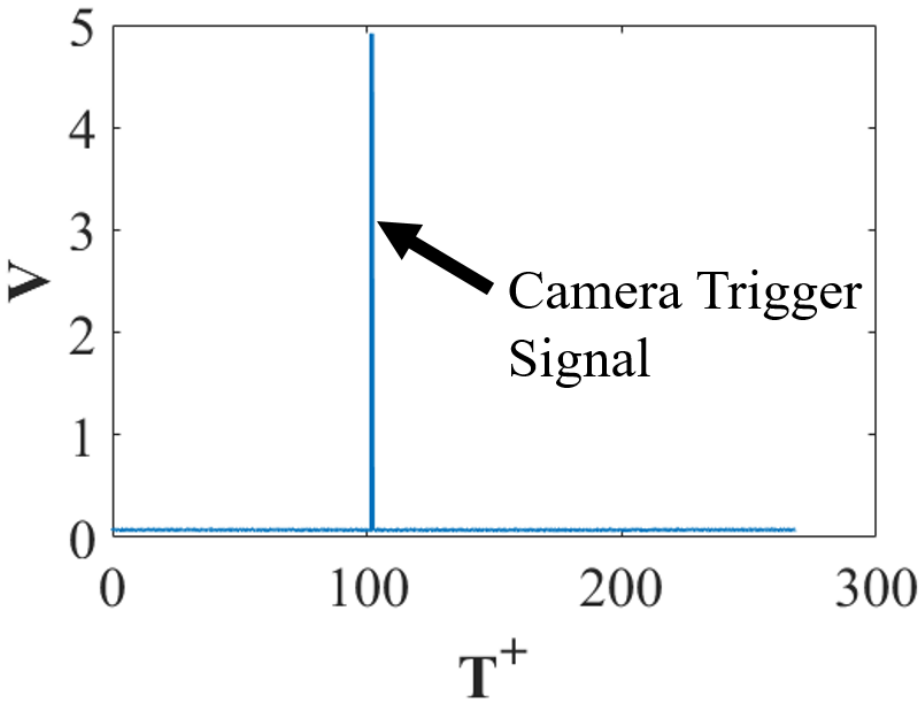

Figure 2.10 Camera Trigger line read at 1 MHz with one image set of SPIV acquired

All outputs are nondimensionalized by the excitation voltage V, which remains close to 5V. This method eliminates the number of leading zeros LabVIEW outputs, which improves the accuracy of the recorded measurement. The moving mean acts as a high-pass filter at $F^+ = 0.1$, which is why these measurements are more beneficial than using the time-averaged mean.

For sampling hot-film and SPIV measurements simultaneously, the SPIV setup largely remains the same as described in Section 4.4, but the setup was slightly adjusted. The camera viewing angles changed to be 26° and 231°. The RMS of fit for the pinhole calibration was 0.447798 and 0.283297 pixel, with a scale factor of 13.8969 pixel/mm. Here the exponential calibration was employed, again.

In order to synchronize surface-mounted hot-film and PIV data collection, the portion of time where PIV data was being acquired needed to be analyzed while the hot-

film data was acquired. The Camera Trigger connected to the PTU outputs a 5V TTL signal to instruct the camera to begin recording images. This line was teed off to also read the signal into LabVIEW via the NI BNC-2090A. As the hot-films are sampled, this line is also being recorded in LabVIEW at a substantially higher sampling rate (1 MHz) to ensure this signal is captured. Figure 2.10 shows the Voltage sampled from the Camera Trigger line when a dataset of PIV is captured. The sudden jump in voltage details when PIV data began being captured. The sampling rate associated with the PIV setup details the duration of simultaneous measurements.

3 Unsteady Disturbance Characterization

3.1 PUG Placement Comparison

To confirm that the installation of the PUGs closely matched the positions used in previous studies, PIV data was gathered and compared with the previous study [20]. The results were used to verify that the PUG placement and characteristics both reasonably matched. Also, this comparison helped show consistency in the PIV measurement and setup. For this examination, the $F_{PUG}^{+} = 0.41$ case [20] was used to generate multiple data sets matching the same data acquisition equipment settings. Of the phases, only the phase at $t/T_{PUG} = 0.78$ is shown because the disturbance stretches across the entire PIV plane. Figure 3.1 presents the measured velocity contours. The current setup is shown in Figure 3.1a and data from the previous study is shown in Figure 3.1b. There are noticeable differences, primarily in the shape and magnitude of the disturbance less than one region,

the blue area. In the current study, the disturbance propagates up toward the positive y/C_x region to a larger degree, has a higher average velocity magnitude, but the disturbance has the same general shape and magnitude for velocity. These slight differences can be attributed to the sensitivity of the measurement plane location, specifically in the spanwise direction, and any slight changes in the wind tunnel. Spanwise vorticity and turbulence intensity were also compared to look for any major differences. Other phases of the disturbance showed the similar results: the same approximate shape and magnitude, but there were some noticeable differences. Spanwise vorticity was also compared and showed the same general trend of similar shape and magnitude, but with some minor differences.

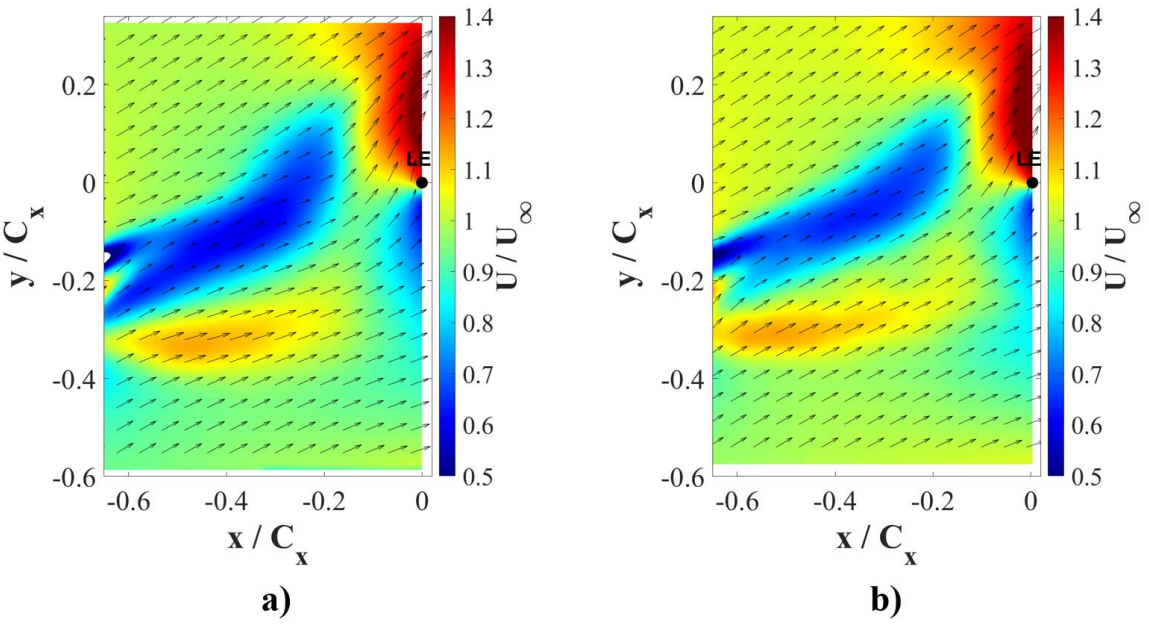

Figure 3.1 Comparison of the velocity distribution measurements for a) current setup and b) previously used setup [20]

Figure 3.2 shows turbulence intensity across the plane for both setups. Turbulence intensity was calculated using Equation 3.1 and showed larger differences between the two setups, than velocity and spanwise vorticity.

$$Tu = \frac{\sqrt{\frac{1}{2}\left(u_{rms}^2 + v_{rms}^2\right)}}{U_\infty} \cdot 100\% \tag{3.1}$$

In the current setup, the disturbance causes the turbulence intensity to impact further in the negative y/C_x direction, especially close to the LE. Additionally, the strength of the turbulence intensity in this direction is higher across most of the plane. Also, the turbulence intensity around the LE is lower in the current setup, which is caused by the disturbance not propagating as far during the same phase. This delay might be caused by the minor differences in the PIV plane location, small changes in the tunnel, or any minor changes in the PUG location. Overall, this is a fairly minor difference considering all the parameters that could have changed between the current setup, and the previous setup used in Ref. 20.

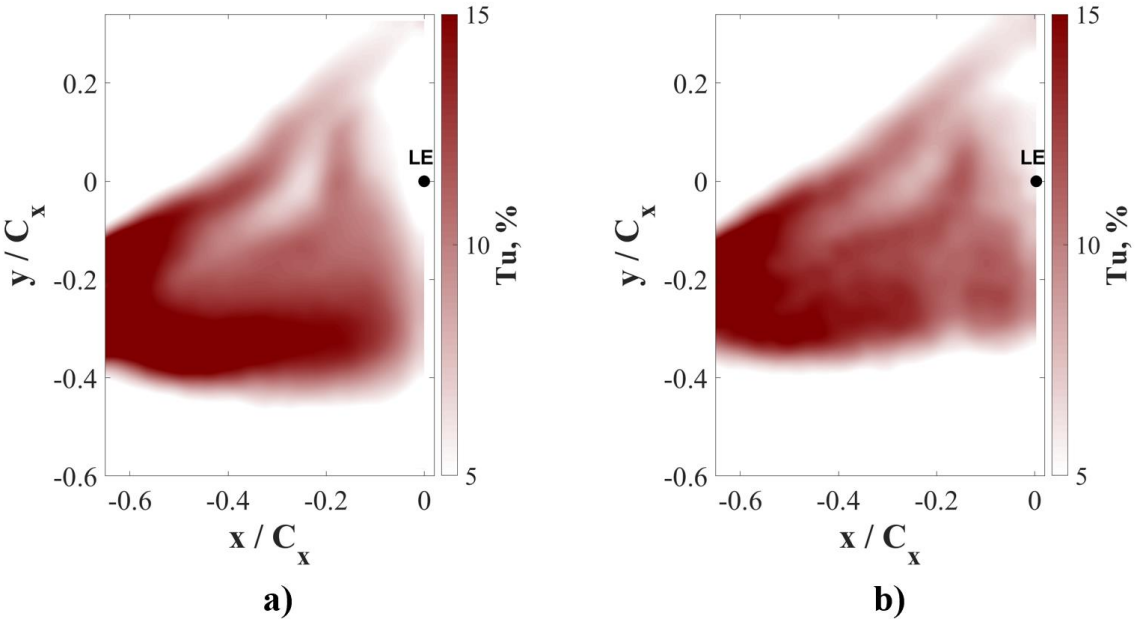

Figure 3.2 Comparison of turbulence intensity for a) current setup and b) previously used setup [20]

Three factors that were analyzed in the previous research study to characterize the disturbance was the velocity profile, turbulence intensity, and incidence angle at $x/C_x =$

-0.3. This process was repeated in the present study to further compare the two experimental setups, and the results are shown in Figure 3.3. Overall, the plots largely show similar results with some minor differences. The velocity looks very similar, the turbulence intensity of the current setup has a slightly different shape and higher peak but overall similar trend, and the incidence angle of the current setup has the same shape but lower magnitude. The differences are most likely caused by minor variation in either the wind tunnel setup, PUG installation, or the experimental setup, but any minor change in either of these categories can explain these differences. Both setups still produced very similar results that verifies the PUGs were installed correctly, the PIV experimental setup is similar to the one used by in previous work [20], and the wind tunnel has not substantially changed since these experiments were performed a similar experiment.

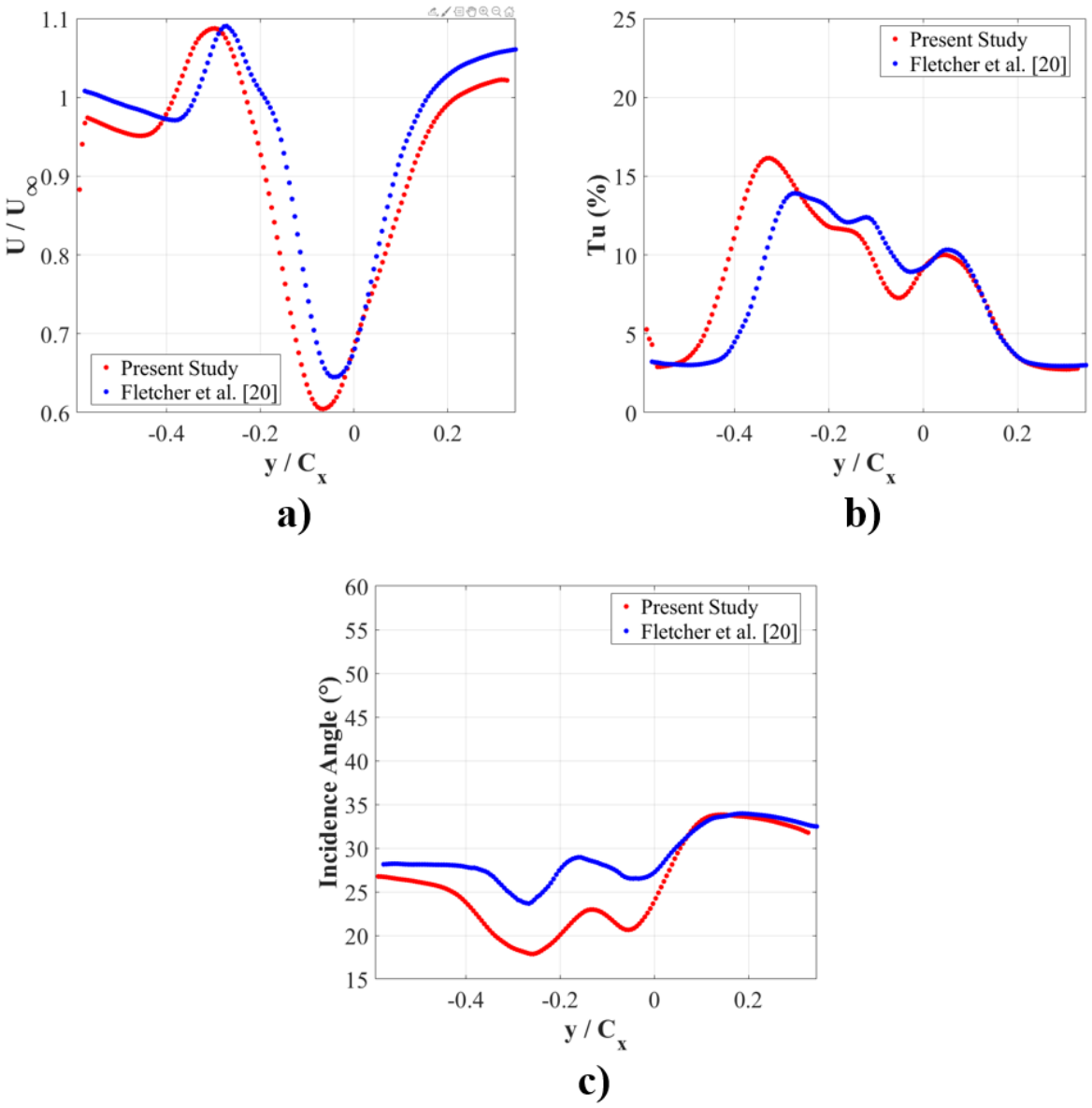

Figure 3.3 Comparison of the new $F^{+}_{PUG} = 0.41$ measurements with those in Ref. 20, at $x/C_x = -0.3$ at phase $t/T_{PUG} = 0.78$ for a) velocity, b) turbulence intensity, and c) incidence angle

3.2 Single Phase Ensemble Averaged Results

To determine which hardware settings to use for each disturbance size, the parameters were iteratively chosen and analyzed, and flow evaluated until similar disturbances were produced at each frequency considered. This involved modifying the supply pressure and the solenoid valve duty cycle until the disturbances were sufficiently

similar in size and other characteristics. The TE jets were supplied with a steady 17 psia supply pressure. Figure 3.4 shows the velocity gradient by subtracting the average inlet freestream velocity from the local velocity magnitude that reveals two velocity gradients appearing on either side of the PIV plane. The larger velocity gradient appearing around x/C_x is caused by the downstream L2F blade with the LE marked on the figure. The blade causes a region of increased velocity on the SS of the blade and a region of decreased velocity on the PS side of the blade. Additionally, the PUG is creating another velocity gradient even with the TE jets set to 17 psia because of its profile wake. This is a significantly smaller velocity gradient than the one caused by the blade. The $x/C_x = -0.3$ position was chosen as the location to evaluate disturbance characteristics, as it in close proximity to the LE, while avoiding most of the high gradient regions. Initial tests to confirm similar sized disturbances used only 100 images to quickly process and analyze in DaVIS and MATLAB. Once the initial results confirmed that the PUG devices setting produced disturbances that were similarly sized and with similar fluid dynamic characteristics, larger sets of 2,000 images were acquired at multiple phases to better visualize and compare the disturbances. All images shown in this section were produced from the 2,000 image sets. The velocity, turbulence intensity, incidence angle (incidence angle), and V' were compared at $x/C_x = -0.3$ to find close matching results for each pulsing frequency

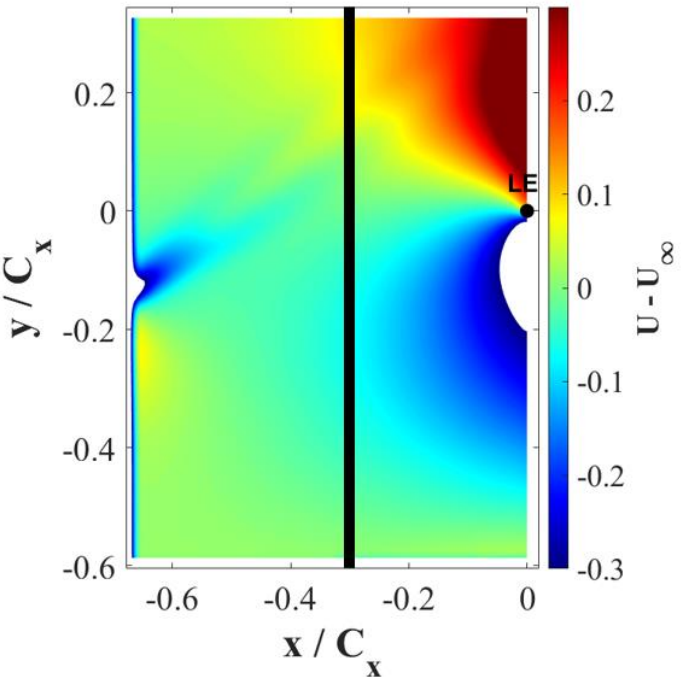

Figure 3.4 Velocity distribution for the $F^{+}_{PUG} = 0$ with $p_{TE,jets} = 17$ psia (baseline case) showing the velocity deviation from freestream

For these comparisons, the images were captured at the same time delay relative to the solenoid valve driving signal. As a result, each pulsing frequency image set is at a different phase of the pulsing period, but the disturbances were located in roughly the same location in the passage. Figure 3.5 shows the ensemble average of U_δ at 26 milliseconds after the solenoid valve is opened. Upstream of the core of the disturbance are regions of positive and negative U_δ values extending from the PUG. The core of the disturbances

match in size and shape confirming that the disturbance was located in the same positions for all three frequencies shown.

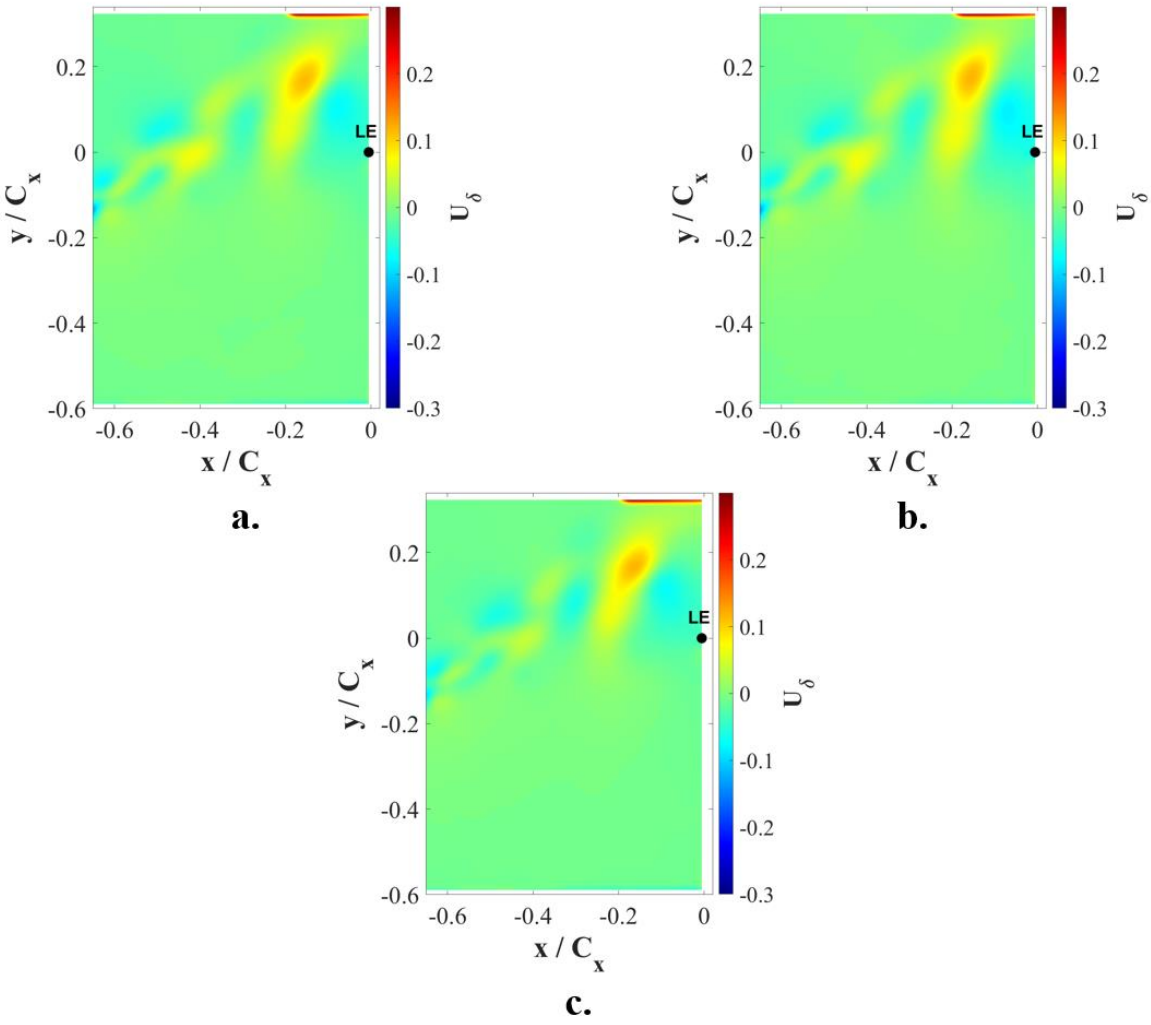

Figure 3.5 U_δ contours for the small disturbance case 26 milliseconds after the TTL signal is received for F^+_{PUG} = a) 0.41, b) 0.85, and c) 1.25

Figures 3.6 presents the ensemble average of velocity, turbulence intensity, incidence angle, and U_δ at $x/C_x = -0.3$ for the small cases taken at the same reference time as was used in Figure 3.5. All incidence angles are relative to the design angle of 35°. The turbulence intensity and incidence angle plots show good agreement between each pulsing frequency. For the velocity magnitude shown in Figure 3.6a, the $F^+_{PUG} = 1.25$ case differs sin a small region of the plane where the velocity is slightly higher than the $F^+_{PUG} =$

0.41 and 0.85 cases. This difference occurs in the region with a slight velocity gradient. To help eliminate the influence of the velocity gradient, U_δ was introduced to understand how the disturbance influenced the velocity magnitude even in regions with a large velocity gradient. Here the $F^+_{PUG} = 1.25$ case differs from the $F^+_{PUG} = 0.41$ and 0.85 cases as its plot has a lower minimum and maximum U_δ value, but a similar general shape. Comparing Figure 3.6a-d captures the importance of accounting for the velocity gradient when analyzing how the disturbance influences the velocity. This same analysis is repeated over 23 milliseconds and 29 milliseconds after the solenoid valve is opened, and these plots show a similar trend. All three other parameters (velocity, turbulence intensity, and spanwise vorticity) also matched over the three reference times. Therefore, the three pulsing frequencies and accompanying hardware settings produced similar disturbances.

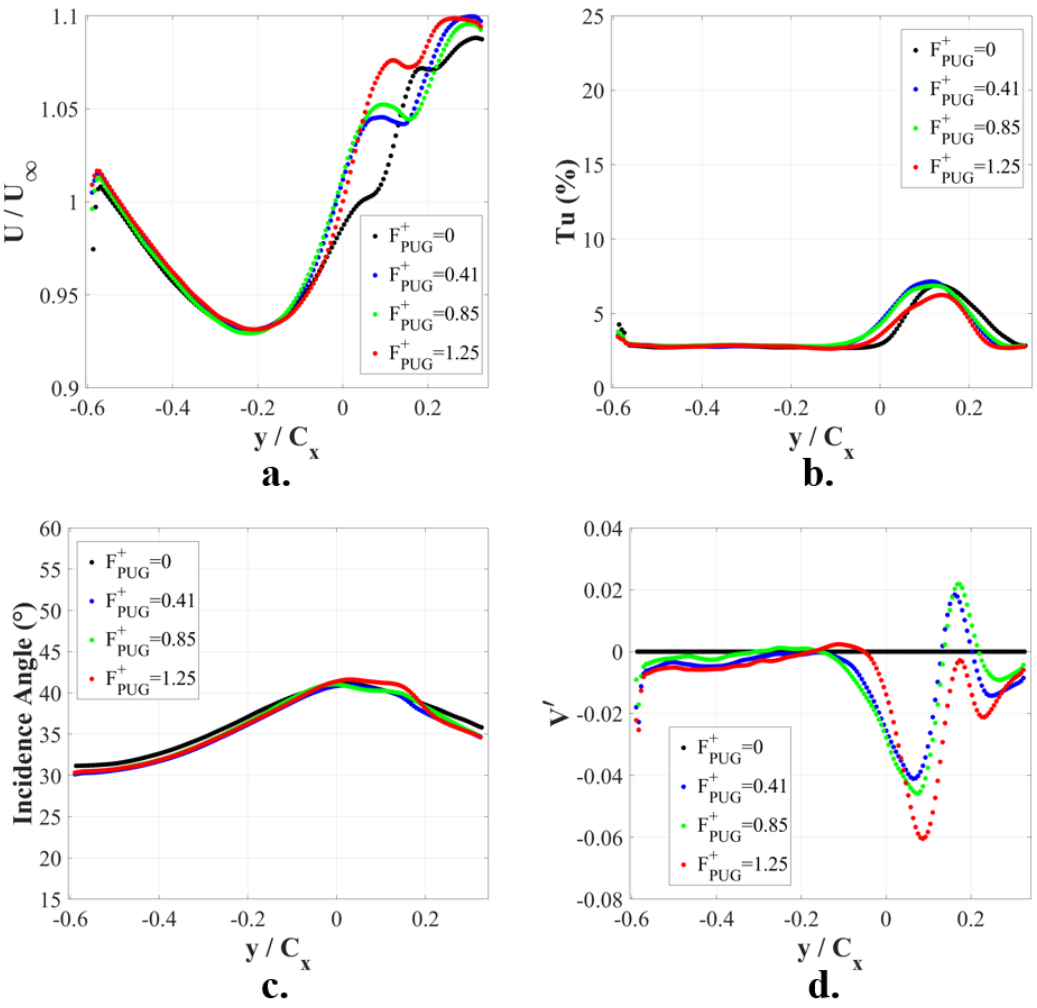

Figure 3.6 Comparison of the small disturbance cases at $x/C_x = -0.3$ at a reference time of 26 milliseconds for a) velocity, b) turbulence intensity, c) incidence angle, and d) U_δ

To further compare the disturbance produced for each case, the integral of each parameter, velocity, turbulence intensity, incidence angle, Φ, and U_δ were computed. Also, the minimum velocity and U_δ minimum and maximum were included. Using the integral values helps to eliminate some of the minor differences in magnitude and shape for each parameter while also providing a single number to compare each case with. Analyzing the minimum and maximum values of the velocity parameters helps to compare each disturbance and their influence on velocity more accurately, especially since the U_δ parameter eliminates the influence of velocity gradient. The results, Table 3.1, show very

good agreement for the $F^+_{PUG} = 0.41$ and 0.85 case. The $F^+_{PUG} = 1.25$ case again showed slight deviation in the integral of turbulence intensity and the minimum and maximum of U_δ. In the other parameters, this case agreed well with the lower frequency cases.

Table 3.1 Computed quantities for small disturbance at $x/C_x = -0.3$ for a reference time of 26 milliseconds

F^+_{PUG}	$\int (U^*)dy$	$\int (Tu)dy$	$\int (\Phi)dy$	$\int (V')dy$	$\min(U^*)$	$\max(U^*)$	$\min(U_\delta)$	$\max(U_\delta)$
0.41	-0.911	-3.38	-32.8	0.0073	0.931	1.10	-0.411	0.0184
0.85	-0.910	-3.39	-33.0	0.0065	0.930	1.10	-0.0458	0.0218
1.25	-0.914	-3.12	-33.1	0.0103	0.932	1.10	-0.0605	0.0024

For the large disturbance case, the same analysis was performed. To start, the plane of data was compared for each pulsing frequency showing velocity, turbulence intensity, spanwise vorticity, and U_δ. Figure 3.7 shows the U_δ plots compared for each pulsing frequency taken at the same reference time as the small cases: 26 milliseconds. Again, the $F^+_{PUG} = 0.41$ and 0.85 cases appear identical, but $F^+_{PUG} = 1.25$ shows some slight difference. The negative U_δ region close to the LE is significantly smaller and lower in magnitude and the positive U_δ region is larger in size compared to the lower pulsing frequency cases. The same trend appeared in the other plots where all the cases look very similar, but the $F^+_{PUG} = 1.25$ exhibits some minor differences.

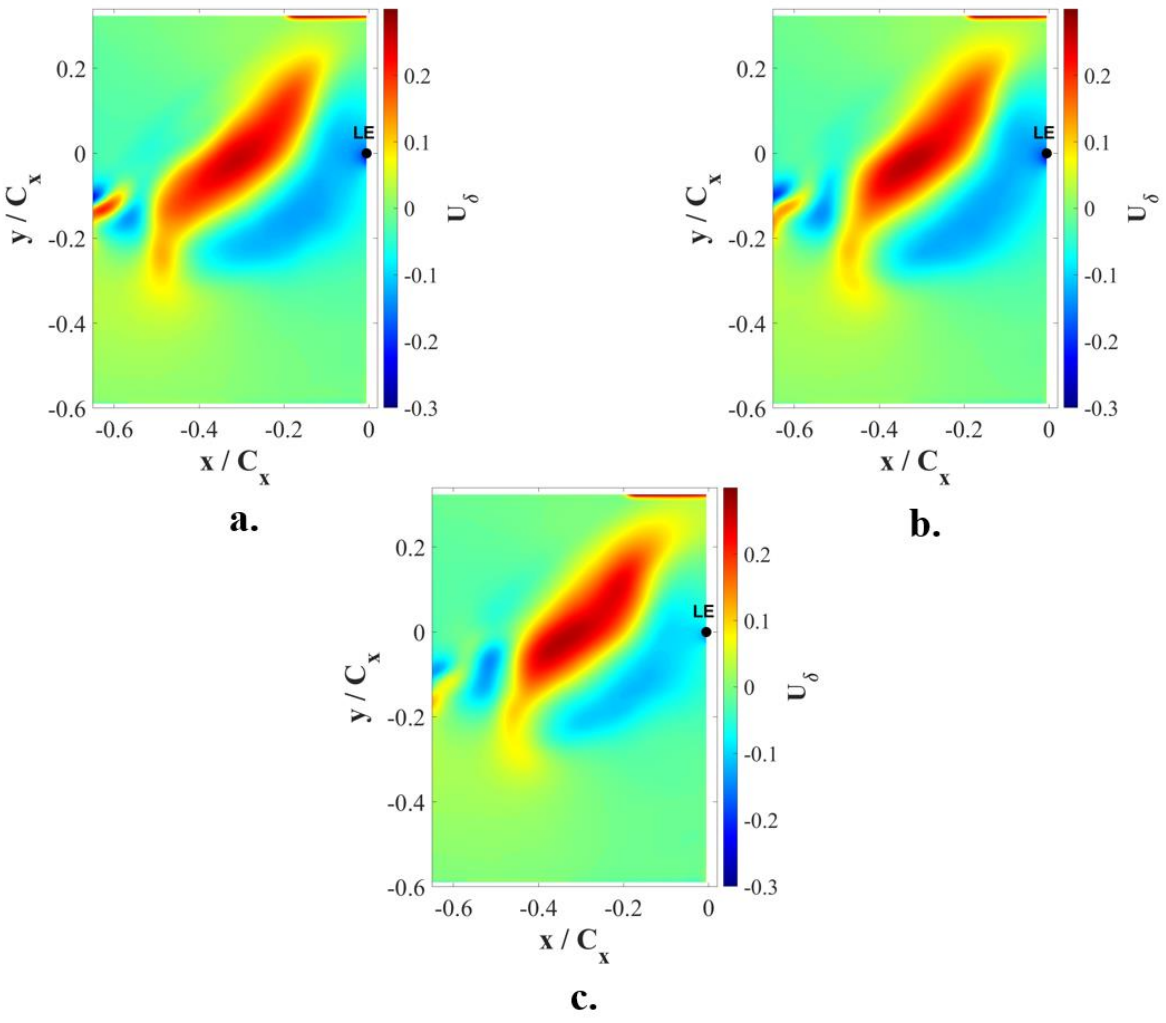

Figure 3.7 2D2C PIV U_δ contours for the large disturbance case 26 milliseconds after the TTL signal is received for F^+_{PUG} = a) 0.41, b) 0.85, and c) 1.25

All three pulsing cases produced almost identical velocity, turbulence intensity, incidence angle, and U_δ distributions at a reference time of 26 milliseconds. The $F^+_{PUG} = 0.85$ is the only case that shows minor deviation from the other two cases primarily near $y/C_x = -0.2$, but these differences are incredibly minor. Figure 3.8b shows slightly higher turbulence intensity and Figure 3.8c shows slightly lower incidence angle around this location. The velocity values shown in Figure 3.8a and 3.8d all show synchronized and consistent results in magnitude and shape.

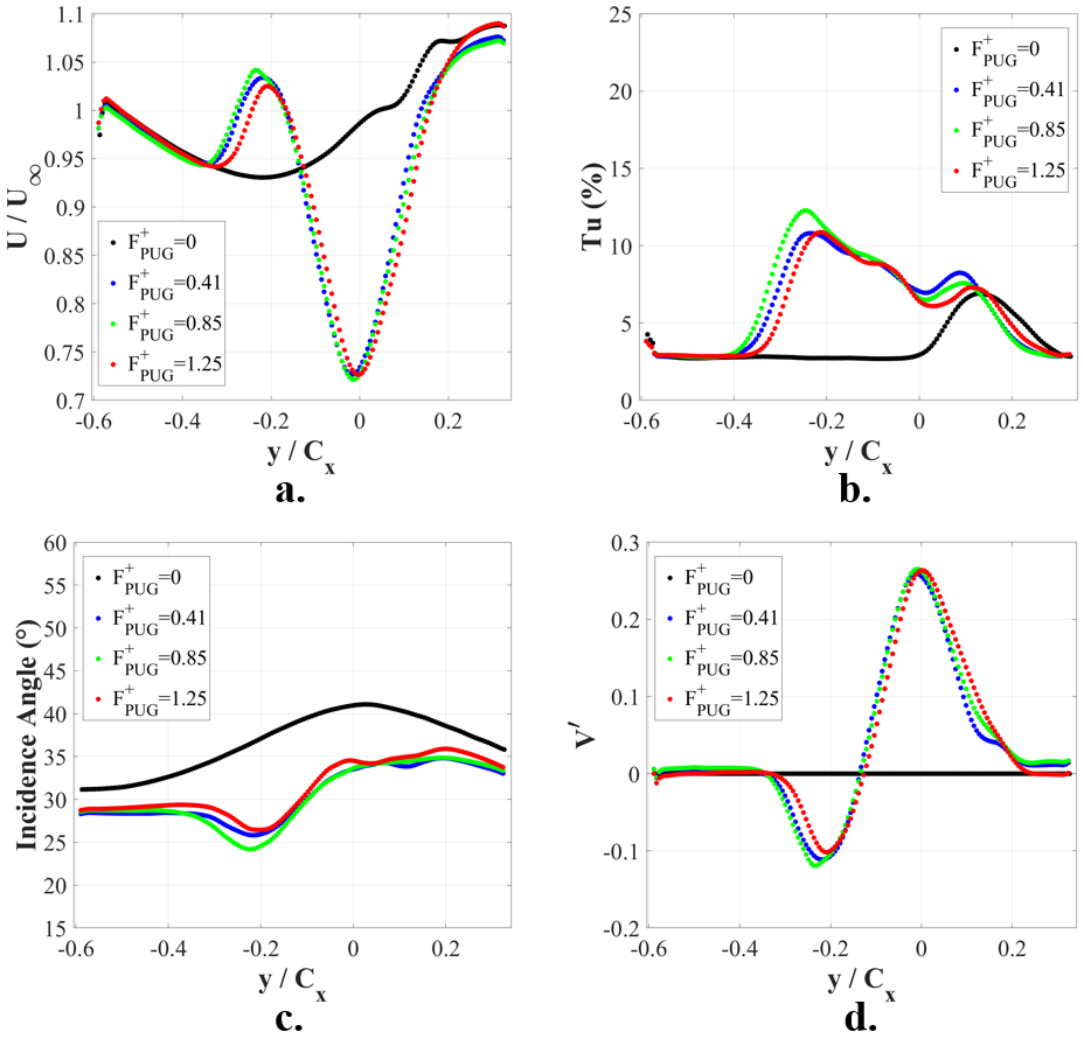

Figure 3.8 Comparison of the large disturbance cases at $x/C_x = -0.3$ at a reference time of 26 milliseconds for a) velocity, b) turbulence intensity, c) incidence angle, and d) U_δ

The integral of the velocity, turbulence intensity, incidence angle, and U_δ were computed using the values shown in Table 3.2 for the large disturbance case at $x/C_x = -0.3$ for a reference time of 26 milliseconds. Additionally, the minimum and maximum values for the velocity quantities were evaluated to help with the comparison. All the cases showed very similar results with only minor deviations. Some minor deviations are expected, especially considering how different the pulsing frequencies are.

Table 3.2 Computed quantities for large disturbance at $x/C_x = -0.3$ for a reference time of 26 milliseconds

F^+_{PUG}	$\int(U^*)dy$	$\int(Tu)dy$	$\int(\Phi)dy$	$\int(V')dy$	$\min(U^*)$	$\max(U^*)$	$\min(U_\delta)$	$\max(U_\delta)$
0.41	-0.868	-5.54	-27.9	-0.0344	0.727	1.08	-0.111	0.259
0.85	-0.866	-5.76	-27.8	-0.0362	0.722	1.07	-0.0120	0.265
1.25	-0.866	-5.31	-28.6	-0.0365	0.727	1.09	-0.102	0.264

These results confirm that the disturbances created are very similar for each of these parameters. To better relate the disturbance duration to the flow dynamics, the solenoid valve on-time was non-dimensionalized for each disturbance case $T^+_{ON,PUG}$. This relates the pulsing frequency and its associated duty cycle to the passage convective time. Additionally, the time between the pulses was computed and compared for each case to estimate how many convective times the LE junction flow had to recover from the disturbances ΔT^+_{pulses}. Table 3.3 summarizes the solenoid driving signal characteristics. For the small disturbance cases, the $F^+_{PUG} = 1.25$ had a slightly higher solenoid on-time, and the large disturbance cases all had very similar on-times. The $F^+_{PUG} = 1.25$ small and large and the $F^+_{PUG} = 0.85$ large cases all had the time between disturbances less than one convective time. On average, the solenoid was ON for about 0.15 and 0.4 convective times in the small and large cases, respectively.

Table 3.3 On-time for the solenoid valves used to create each disturbance

F^+_{PUG}	Size	$T^+_{ON,PUG}$	ΔT^+_{pulses}
0.41	Small	0.146	2.29
0.85		0.141	1.04
1.25		0.160	0.640
0.41	Large	0.390	2.05
0.85		0.400	0.776
1.25		0.400	0.400

Table 3.4 shows the hardware settings for the cases, and includes the cases used previously by Fletcher et al. [20]. Experiments by Fletcher et al. were conducted at three disturbance frequency, using great care to create disturbances of similar magnitude. All of the previous disturbances cases had larger magnitude and duration than the largest disturbance cases used in the present study. The first case shown in Table 3.4 represents the baseline case, with pulsed jets off. For the small disturbances, the maximum velocity deficit at this location was around 0.15, and, for the large disturbance, the maximum velocity deficit was around 0.3. Overall, each sized disturbance closely matched regardless of the pulsing frequency.

Table 3.4 PUG hardware settings

F^+_{PUG}	f (Hz)	Size of Disturbance	DC	$p_{LE,plenum}$ (psia)	$p_{TE,jets}$ (psia)
0 Ref. [20]	0	-	-	-	17.0
0.19 Ref. [20]	5	-	15	33.0	17.0
0.41	11	Small	6	18.0	17.0
0.41	11	Large	17	32.0	17.0
0.41 Ref. [20]	11	-	25	45.0	17.0
0.56 Ref. [20]	15	-	35	55.0	17.0
0.85	23	Small	12	24.0	17.0

0.85	23	Large	34	48.0	17.0
1.25	35	Small	20	23.0	17.0
1.25	35	Large	50	61.0	17.0

3.3 Multiphase Ensemble Averaged Results

Multiphase data was used to track U_δ, turbulence intensity, and vorticity past $y/C_x = -0.1$ across a full actuation period (T_{PUG}). For these plots, the center of the disturbance is defined as the location corresponding to the maximum value for U_δ, and the LE is projected forward based off of the chosen y/C_x value and the inlet flow angle of 35°. These plots are generated by repeating the results for the actuation period over 7 convective times to help visualize the disturbance's length and compare each case. Tracking the disturbance past a line close to the LE offers clearer insight into its impact on the flow, proximity to the LE, and the convective time of one disturbance. Figure 3.9 shows the space-time plots of U_δ, turbulence intensity, and vorticity plots for the $F^+_{PUG} = 0.41$ small disturbance case, and Figure 3.10 shows the same plots for the $F^+_{PUG} = 0.41$ large disturbance case. The small case in Figure 3.9 shows that the core of the disturbance missed the LE by about $y/C_x = 0.25$, but it still perturbed the velocity and turbulence intensity around the LE. Figure 3.10 presents a more ideal scenario where the disturbance was better aligned with the LE. The region with negative U_δ and positive vorticity largely passed to the PS, and the region with positive U_δ and negative vorticity largely passed to the SS.

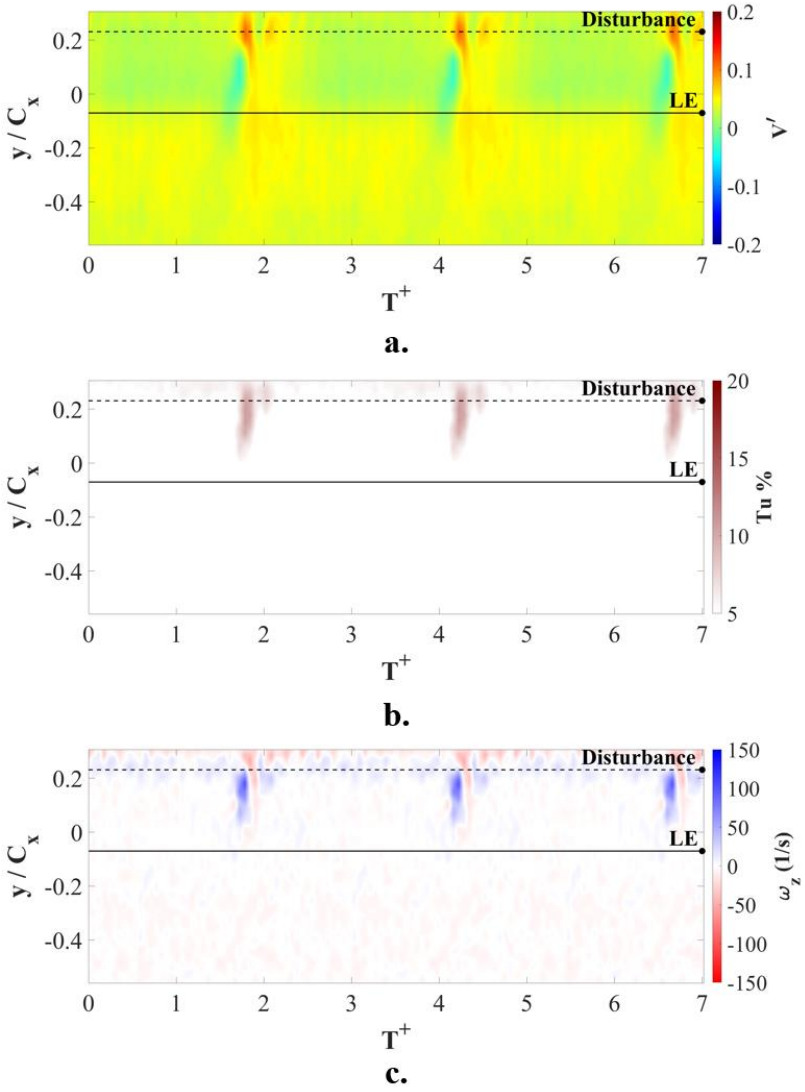

Figure 3.9 Space-time plots for $F^+ = 0.41$ small disturbance at $x/C_x = -0.1$ across dimensionless time for a) U_δ, b) turbulence intensity, and c) spanwise vorticity

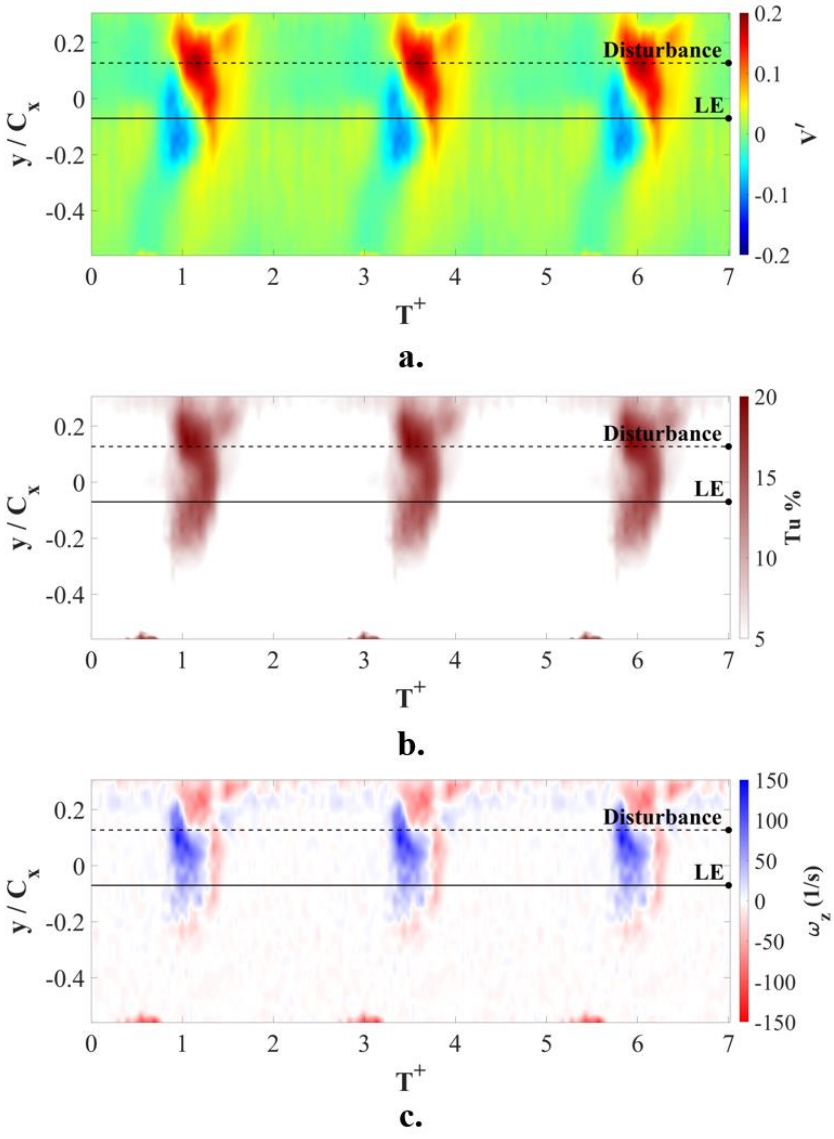

Figure 3.10 Space-time plots for $F^+ = 0.41$ large disturbance at $x/C_x = -0.1$ across dimensionless time for a) U', b) turbulence intensity, and c) spanwise vorticity

The turbulence intensity space-time plots helped to reveal the period between disturbances. Figure 3.11 shows this quantity plotted for the small disturbance cases. As the pulsing frequency increases, the time between disturbances decreases, but, even for the highest pulsing frequency, the LE has a period of 0.6 convective times where no disturbances are present. This allows the LE junction time to recover from the disturbances and return to its steady inflow behavior.

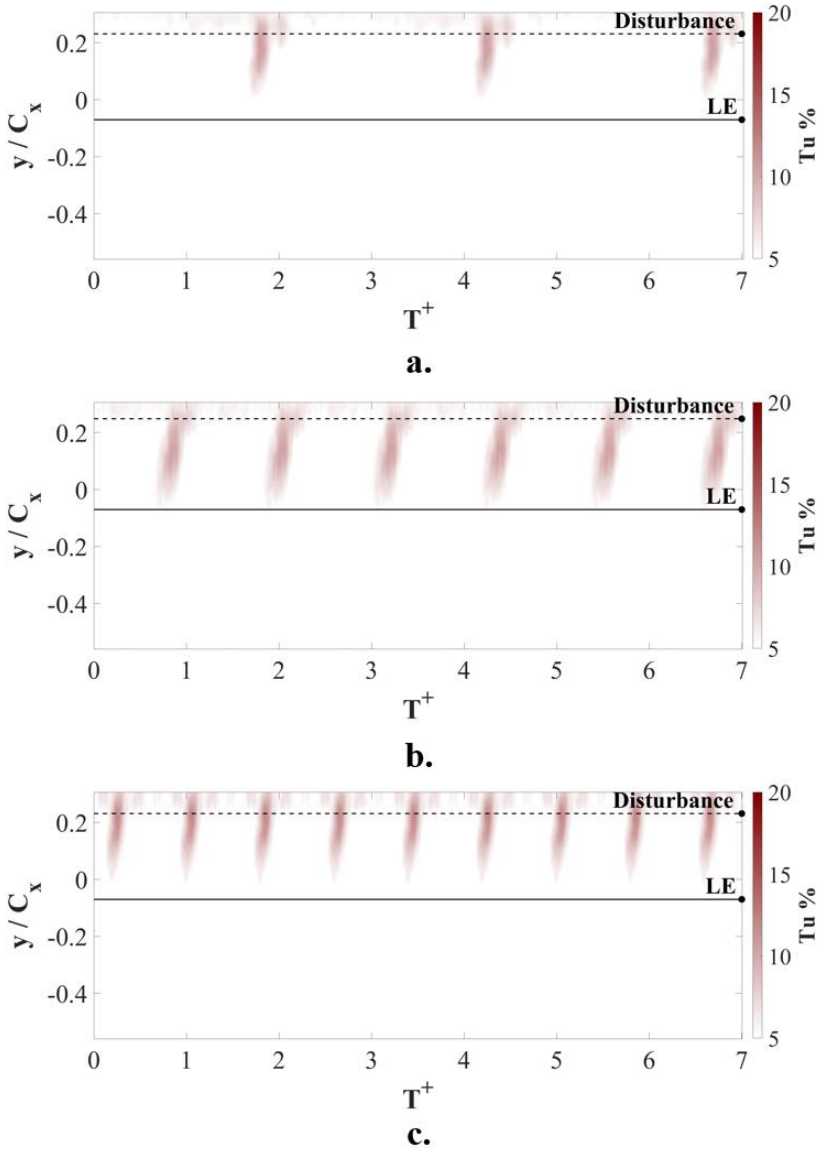

Figure 3.11 Space-time plot of the turbulence intensity values at $x/C_x = -0.1$ for F^+_{PUG} = a) 0.41, b) 0.85, and c) 1.25 small disturbance cases

For the large disturbance cases, the turbulence intensity values tell a very different story. As the pulsing frequency increases, the form of the disturbance starts to lose its shape. Figure 3.12 shows a plot of the turbulence intensity for each the large disturbance cases. In Figure 3.12a, the $F^+_{PUG} = 0.41$ case allows ample time between disturbances so that the LE has about two convective times to recover from the disturbances, and that is

why the disturbances do not appear to blend together like the other cases. These figures show a gradual progression of the core of the disturbance turbulence intensity decreasing and increasing the time averaged FTSI. Both $F_{PUG}^{+} = 0.41$ and 0.85 cases increase the turbulence intensity to $y/C_x = -0.3$, but the $F_{PUG}^{+} = 1.25$ case only increases the turbulence intensity to $y/C_x = -0.25$. This difference is caused by the short time delay between air ejections causing the disturbances to interact with one another. For the disturbance frequencies of $F_{PUG}^{+} = 0.85$ and 1.25, the LE does not have any time to recover from the disturbance.

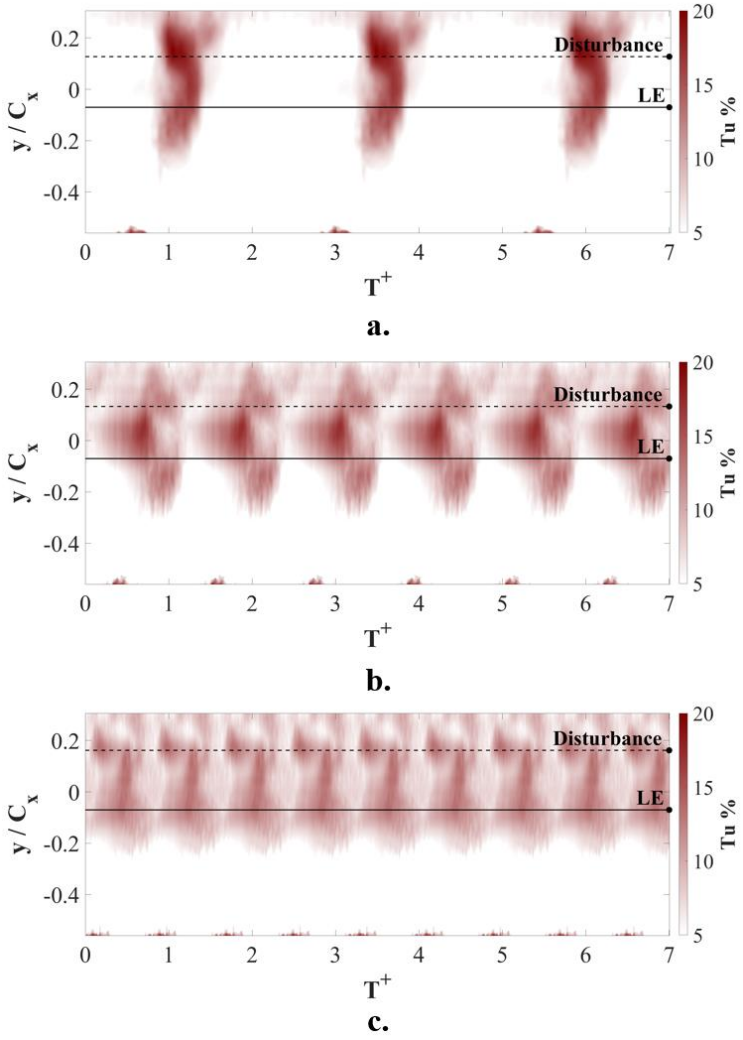

Figure 3.12 Space-time of the turbulence intensity values at $x/C_x = -0.1$ for F^+_{PUG} = a) 0.41, b) 0.85, and c) 1.25 large disturbance cases

Figure 3.13 shows the predicted impact of the disturbance on the LE in respect to velocity, elevated turbulence, and streamwise vorticity for the small disturbance cases, and Figure 3.14 shows the same values for the large disturbance cases. These plots present the LE line from Figures 3.9-3.12 for each pulsing frequency for an easy comparison of each disturbance's size and strength.

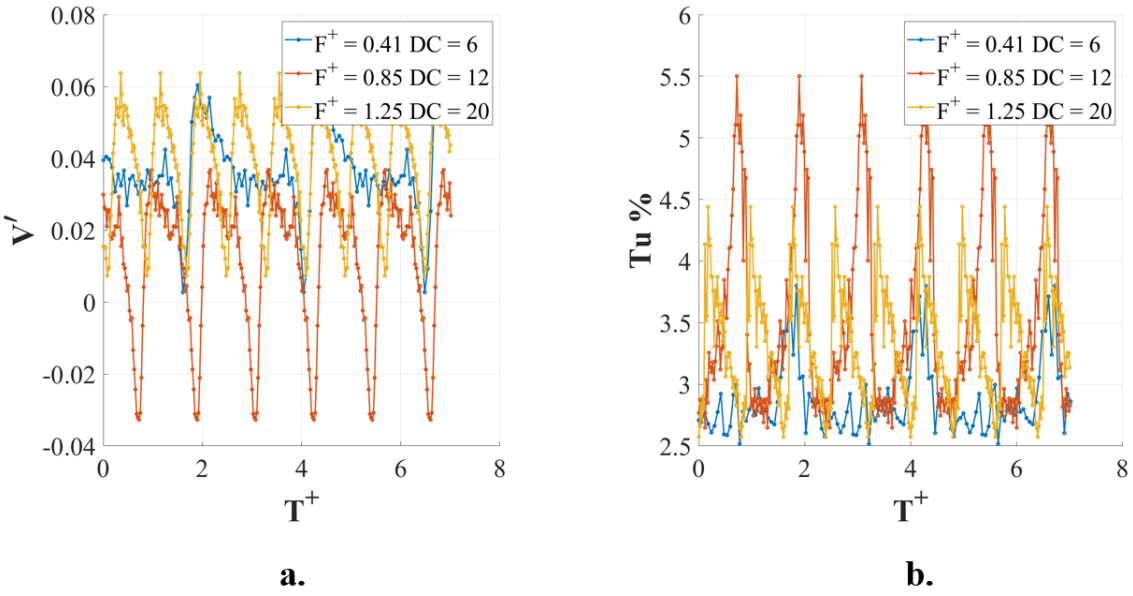

Figure 3.13 Predicted small disturbance cases impact on LE across dimensionless time at $y'/C_x = -0.1$ for a) U_δ and b) turbulence intensity

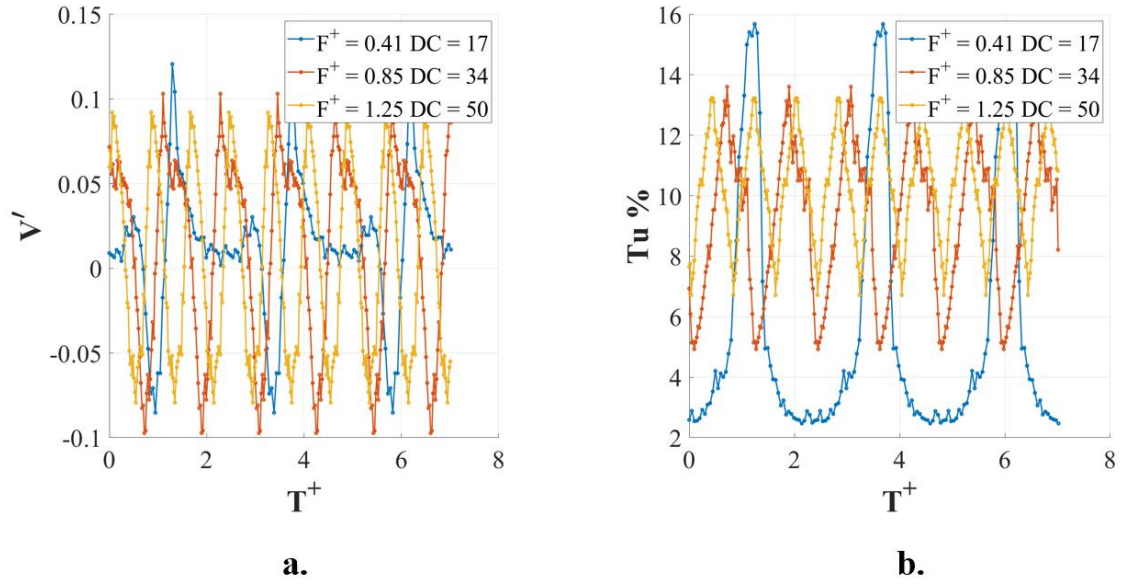

Figure 3.14 Predicted large disturbance cases impact on LE across dimensionless time at $y'/C_x = -0.1$ for a) U_δ and b) turbulence intensity

Figure 3.13a shows the $F^+_{PUG} = 0.85$ small disturbance had a noticeably lower U_δ range compared to the other small cases, and Figure 3.13b shows the same case with higher turbulence intensity values than the other small cases. These two factors made the $F^+_{PUG} = 0.85$ small case appear as an outlier; however, the relative magnitude difference was minor

compared to the large cases. Additionally, it was unclear the impact higher pulsing frequencies would have on the characteristics of the disturbance. Therefore, this disturbance was still utilized because its attributes were similar to the other cases.

The cyclic fluctuation of velocity deficit and turbulence intensity are plotted as a function of passage convection time in Figs. 3.13 and 3.14. The duration of the fluctuation relative to flow convective time changes significantly as disturbance frequency is increased. Disturbance time relative to passage convective time is an important consideration, as the endwall flow dynamics in the passage are expected to respond at a rate slower than the passage convective time. At the lowest frequency, $F_{PUG}^{+} = 0.41$, the disturbance duration is longer than one convective time per period. The incoming flow returns to a steady condition for nearly one convective time in between disturbances. As the disturbance frequency is increased, the time period between disturbance decreased relative to passage convective time, and the endwall vortices in the passage are not expected to respond to individual fluctuations. For $F_{PUG}^{+} = 1.25$, the flow continuously fluctuates, at a rate greater than the passage convective time. Figs. 3.13-3.14 show a clear difference in magnitude for all the quantities, which reaffirm that 6 unique disturbances were created.

4 Endwall Flow Study

4.1 Results

4.1.1 SPIV Results Analyzing PV

In this section, high-speed SPIV measurements in the passage are used to study the change in the vortex temporal behavior with various leading-edge disturbances generated by the PUG device. Two critical aspects of the vortex that were compared are the location of the PV and the strength of the PV for each case. These attributes of the PV provide key insight into if/how the disturbance impacted this key feature of secondary flow. Table 4.1 shows the time-averaged location of the PV. Figure 4.1 shows the 2D histogram of the location of the PV. Each location of the PV was determined by identifying the location with the highest Q-criterion. In these figures, small y'/C_x values correspond to the SS and high values correspond to the PS. Here only the baseline, $F_{PUG}^{+} = 1.25$ small and large, and $F_{PUG}^{+} = 0.85$ large cases are shown because only these cases resulted in any shift in the time averaged location of the PV. The darker red region indicates that the PV was frequently in that location. Figure 4.1a shows that the PV fluctuates from roughly $0.18 \leq y'/C_x \leq 0.38$ and $0.04 \leq z'/C_x \leq 0.12$. For the majority of the time, the PV is located between $0.23 \leq y'/C_x \leq 0.32$ and $0.06 \leq z'/C_x \leq 0.09$, which shows that the majority of shifts in position occur in the pitchwise (y'/C_x) direction, and only minor shifts occur in the spanwise (z'/C_x) direction. The same trends were observed for the pulsating cases.

The pulsing cases shown in Figure 4.1 ($F^+_{PUG} = 1.25$ small and large and $F^+_{PUG} = 0.85$ large cases) caused a small shift in position toward the SS and the endwall compared to the baseline case. Shifts in the location of the PV in these directions are typically indicators of a loss of strength. $F^+_{PUG} = 0.85$ large case had the largest impact, but even that shift is minor. The $F^+_{PUG} = 1.25$ cases had an even less substantial shift, with the large case having a more noticeable impact compared to the small case. Overall, no substantial shift in the PV location distribution was triggered for these disturbances.

Table 4.1 Time-averaged position of the PV in the secondary coordinate system

F^+_{PUG}	**Size of Disturbance**	$(y'/C_x)_{AVG}$	$(z'/C_x)_{AVG}$
0	-	0.0286	0.078
0.41	Small	0.288	0.079
0.85		0.287	0.079
1.25		0.280	0.076
0.41	Large	0.282	0.079
0.85		0.278	0.073
1.25		0.283	0.073

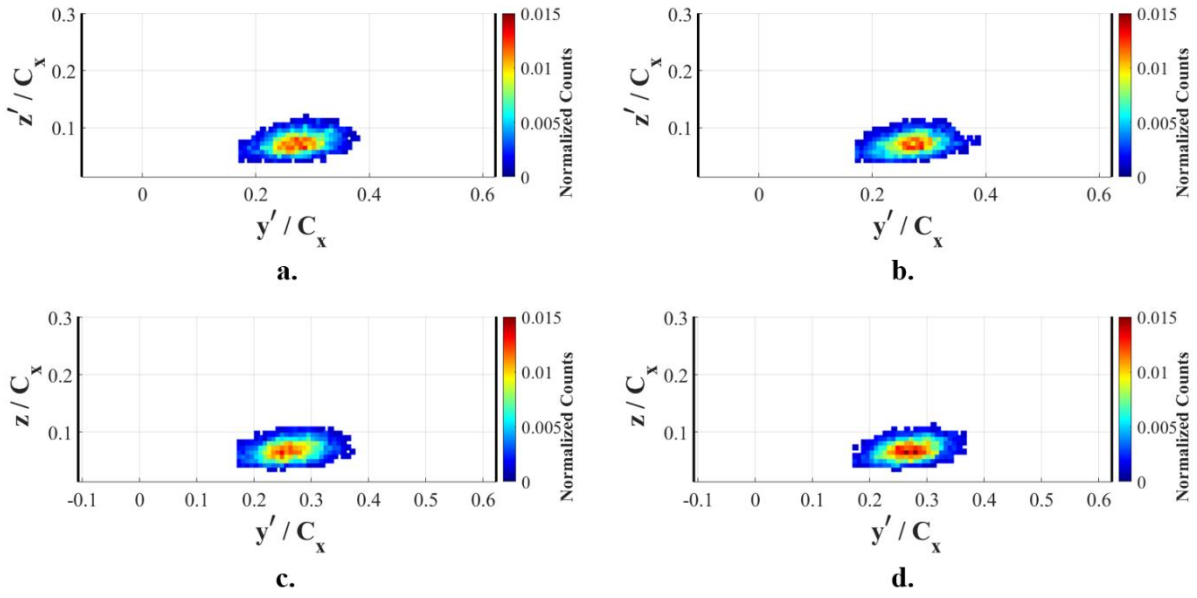

Figure 4.1 2D histogram of PV positions using Q_{max} for F^+_{PUG} = a) 0, b) 1.25 small, c) 0.85 large, and d) 1.25 large cases

The change in the time averaged strength of the vortex is visualized in Figure 4.2 using the $Q = 100$ isoline for $F^+_{PUG} = 0$, $F^+_{PUG} = 0.41$, $F^+_{PUG} = 0.85$, and $F^+_{PUG} = 1.25$ large disturbance cases only. The vortex strength noticeably decreased for the large disturbance cases, while there were only minor decreases in the small disturbance cases. This is why only the large disturbance cases are shown in the plot. Over the range of large disturbance cases, the $F^+_{PUG} = 0.85$ produced a substantial decrease in strength, while the vortex moved closer to the endwall and the SS. The $F^+_{PUG} = 1.25$ case also resulted in a position change and a decrease in its strength, but to a lesser degree compared to $F^+_{PUG} = 0.85$. The $F^+_{PUG} = 0.41$ large case did not show any noticeable shift in the PV location; however, the strength decreased. It appears that disturbances with higher elevated velocity deficit, turbulence intensity, and vorticity values will have a more substantial impact on the strength of the PV.

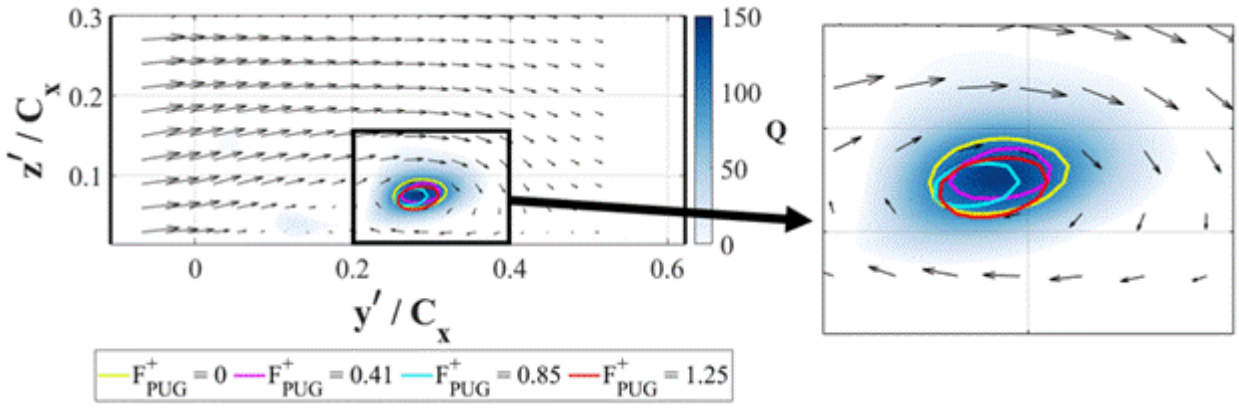

Figure 4.2 Time-averaged Q-criterion contours for $F^+_{PUG} = 0$ with isolines of $Q = 100$ for $F^+_{PUG} = 0$ baseline case and $F^+_{PUG} = 0.41, 0.85$, and 1.25 large cases

Figure 4.3 shows the 2D histogram of the average Q-criterion for each instance that that Q_{max} was located in that location for the baseline and large disturbance cases. In these plots, only the large disturbance cases are pictured because they showed the most impact on the PV strength. Each plot shows a clear relationship between position and strength of the PV. All plots show that the average maximum Q-criterion value is highest close to the PS and decreases going towards the SS. A similar trend was reported in Ref. 20, which also provides some possible reasons for this characteristic. Figure 4.3 shows the average Q_{max} decreases as the actuation frequency increases, with an exception between $F^+_{PUG} = 0.85$ and 1.25. Figure 4.3c and 4.3d have a similar shape, but the average Q_{max} near the SS of $F^+_{PUG} = 0.85$ is slightly larger than $F^+_{PUG} = 1.25$. Near the PS, the trend flips and $F^+_{PUG} = 0.85$ has a lower average Q_{max} compared to $F^+_{PUG} = 1.25$.

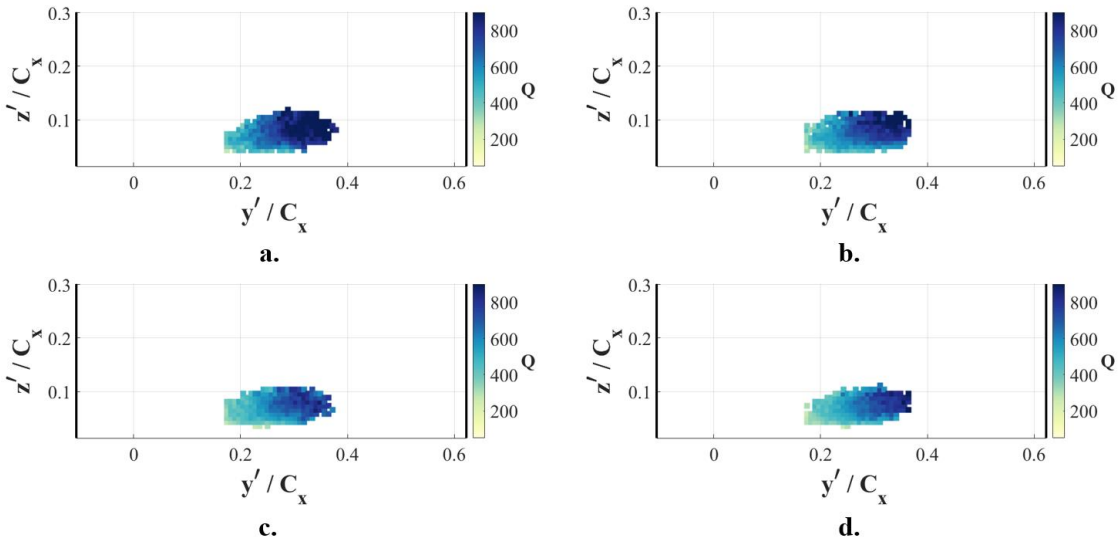

Figure 4.3 Passage vortex position based on Q_{max} colored by average Q_{max} of all occurrences at that position for F^+_{PUG} = a) 0, b) 0.41, c) 0.85, and d) 1.25 (large disturbance cases only)

Also of interest was to determine if the disturbance frequency had any impact on periodically varying the PV strength. The Q_{max} value and y'/C_x location associated with that Q value were tracked and phase-averaged. The average Q_{max} value was used to nondimensionalize the phase averaged Q_{max} value. Figure 4.4 shows the results of this analysis for the small and large cases for $F^+_{PUG} = 0.41$ and 0.85.

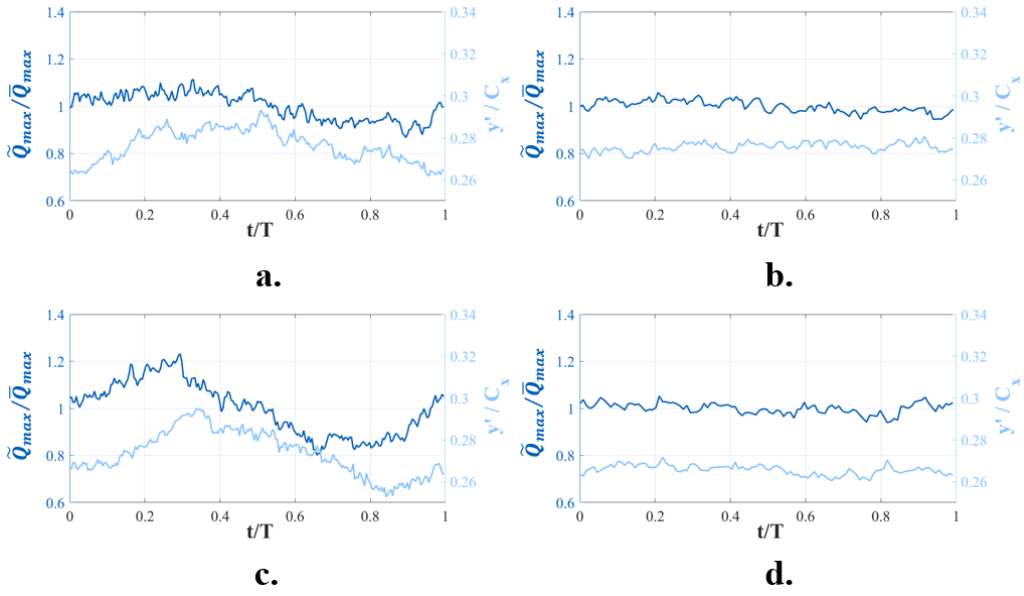

Figure 4.4 Phase-locked ensemble averaged PV Q_{max} (normalized by the time-averaged Q_{max}) and PV y' position at every captured phase for F^+_{PUG} = a) 0.41 small b) 0.85 small, c) 0.41 large, and d) 0.85 large

The $F^+_{PUG} = 1.25$ small and large cases are not shown because they looked very similar to the $F^+_{PUG} = 0.85$ cases. The $F^+_{PUG} = 0.41$ cases show some phase-dependence, more for the large case than the small. Figure 4.4c shows the PV strength and position changing based on the disturbance phase by a factor of 20% versus Figure 4.4a showing a shift of about 10%. Figure 4.4c draws a similar conclusion as previous research, where the PV strength appears to decrease the PV moves closer to the SS. It does appear that the small disturbances have a much smaller impact on the phase-dependence of the PV most likely caused by the disturbance having a minor impact on the PV. Figures 4.4b and 4.4d show a very linear trend in the data, which signifies that the PV is not phase-dependent for either the $F^+_{PUG} = 0.85$ or the 1.25 small and large cases. Comparing the PV location from 4.2b to 4.2d shows the $F^+_{PUG} = 0.85$ large case shifted the PV closer to the SS, but it is still a minor shift. A similar trend appears in the $F^+_{PUG} = 1.25$ case. Previous research included testing at $F^+_{PUG} = 0.41$ and 0.56 for disturbances with a larger velocity deficit and

disturbance period [20]. F^+_{PUG} was determined to have a minor phase dependence, and $F^+_{PUG} = 0.41$ had a heavy phase dependence. Therefore, the loss of phase-dependence occurs between $F^+_{PUG} = 0.56 - 0.85$, but the importance of disturbance size/strength is also a factor. The typical V_{def} reported for their disturbances were around 0.4, but the large case has a V_{def} around 0.15 for the large cases, and 0.10 for the small cases. In their study, the $F^+_{PUG} = 0.41$ case showed a heavy phase-dependence, slightly more significant than the relationship shown in Figure 4.4c. As a result, both the pulsing frequency and the characteristics of the disturbance (velocity deficit, turbulence intensity, period, and vorticity) impact if the strength and position of the PV is dependent on the present disturbance phase.

Space-time plots were developed using isosurfaces of Q-criterion to visualize the in-passage vortex. A sampling of vortex changes with time are shown in Figure 4.5 for the baseline case, with pulsed disturbance off. The vortex position fluctuations and intermittently loses coherence consistent with previous experiments. Figure 4.5a shows a short loss of coherence event as the vortex undulates in the pitchwise direction from the PS to the SS and back to the PS over a time period of 1.3. During this undulation, the vortex does not substantially move in the spanwise direction until close to the end of the undulation where it slowly moves away from the endwall. Figure 4.5b shows a series of short period undulations of the vortex in the pitchwise direction. During these short undulations, the PV also undulates in the spanwise direction, although less pronounced. The undulation in the spanwise direction occurs over roughly the same time as the undulations in the pitchwise direction. Figure 4.5c shows a clear loss of coherence event that started as the PV shifted from the PS towards the SS. For a period of about 1, the PV

struggles to regain coherence, until it completely losses coherence. Analyzing these plots show a connection between the vortex undulating from the PS to the SS and loss of coherence events. Veley et al. [25] noticed a similar trend using surface mounted thin film sensors with steady inflow. The PV also traveled throughout the passage from y'/C_x of 0.17 to 0.37 and z'/C_x of 0.04 to 0.14.

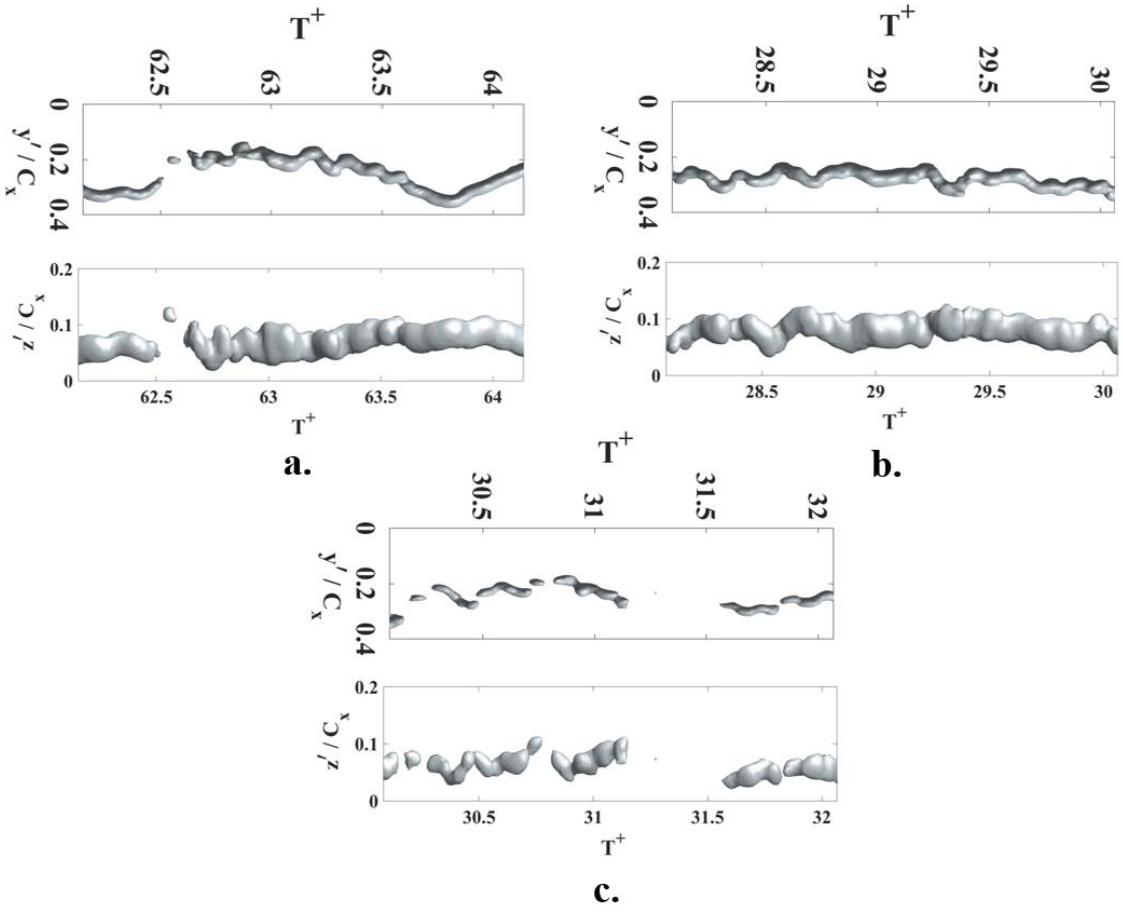

Figure 4.5 Space time plots of isosurfaces of Q = 100 showing examples of a) a long period undulation; b) a series of short period undulations in the pitchwise direction; c) a clear loss of coherence event.

To better visualize the PV, similar plots from Figure 4.5 are presented over more convective times, shown in Figure 4.6. Only the y'/C_x direction across time was plotted here because the z'/C_x direction showed only minor shifts in position with no clear connection to loss of coherence events. Figures 4.6a and 4.6b help showcase the undulation

behavior of the PV, and its connection to loss of coherence events. Figure 4.6a shows 3 undulations, with 2 loss of coherence events occurring shortly after the PV shifts from the PS towards the SS. The first two undulations occur over 1.5 convective times consecutively, and the third undulation takes 4 convective times to complete. For each undulation, the PV does not behave in a similar manner, or give any clear consistent behavior besides the period. Figure 4.6b shows the PV undulate 4 times, with again inconsistent behavior. For this example, it appears that there are 3 undulations with a short period (<1), and one long undulation with a period of 4 convective times. Again, besides the period of the undulation, there appears to be no consistent behavior. Additionally, these plots show potentially 3 loss of coherence events. Two occur in Figure 4.6a with the first occurring at $T^+ = 53.5$ and the second starting at $T^+ = 56$. The loss of coherence event beginning at $T^+ = 53.5$ occurs after the PV shifts from the PS to the SS, and it shows the PV intermittently regain and lose coherence over a period of 1. The second loss of coherence event occurs as the PV shifts from the PS to the SS, again, but this event is much clearer. It also has a period around 1. In Figure 4.6b, loss of coherence event happens starting at $T^+ = 62.5$. The PV loses coherence after shifting from the PS towards the SS, but it regains coherence quickly. After regaining coherence, it starts to shift and change size drastically. This maybe a product of the method employed to visualize the PV, or it could be a loss of coherence event causing the method to produce odd looking results. If this case is assumed to be a loss of coherence event and its end occurs once the PV maintains its strength and direction, the approximate period is 1. By analyzing these 20 convective times, it showcases the erratic behavior of the PV, and the loss of coherence events are not driven by the pulsed disturbances.

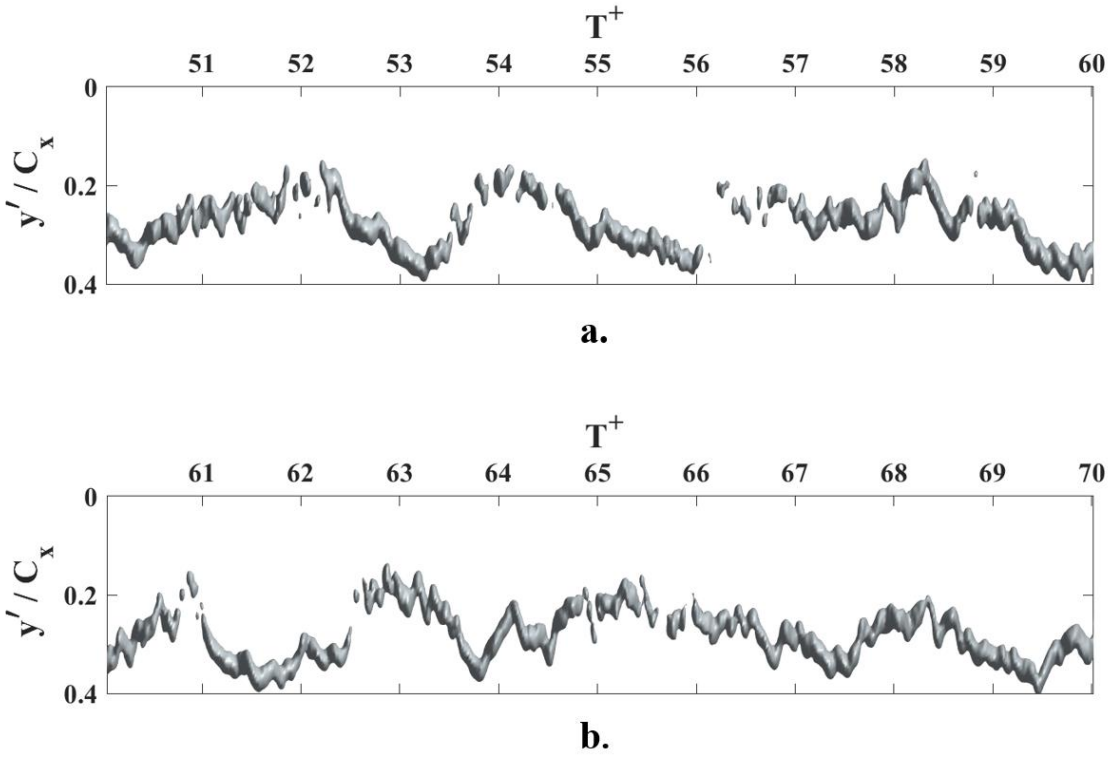

Figure 4.6 Space-time plot of isosurfaces of $Q = 100$ for the baseline case shown at a) $T^+ = 50 - 60$ and b) $T^+ = 60 - 70$

Verifying whether or not the fluid phenomena coupled to the pulsing frequency of the PUG was necessary to confirm that the disturbances were impacting the fluid dynamics near the PV. Power spectral density (PSD) plots were generated using V_y, the pitchwise velocity component, at the time averaged location of the PV and Welch's method. The time series data from V_y was broken into four segments with Hamming windows and 50% overlap. This ensures good spectral resolution and averaging. The same process was applied to the 8 surrounding points of the time averaged location of the PV, and the spectral results were all averaged. Figure 4.7 shows these PSD plots for the baseline case (a) and the large disturbance cases. Only the large disturbance cases are shown because the small disturbance cases for $F^+_{PUG} = 0.41$ and 0.85 are similar to the baseline case, or, for $F^+_{PUG} = 1.25$, matched the large disturbance case. The baseline case shows 4 strong peaks at

frequency multiples of 0.4. This signifies harmonic behavior occurring for V_y, near the time averaged location of the PV, actuating at a frequency of 0.41. Additionally, there is a band of peaks from $0.1 - 0.6$ with a few distinct peaks at frequencies of 0.10 and 0.41. The same process yielded similar results when applied to V_z.

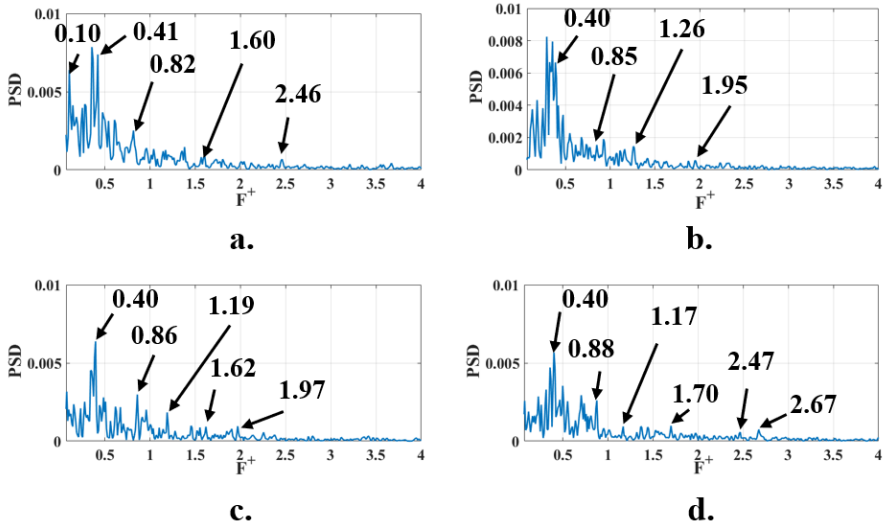

Figure 4.7 PSD of V_y, at time averaged location of PV for a) $F^+_{PUG} = 0$ baseline case, b) $F^+_{PUG} = 0.41$ c) $F^+_{PUG} = 0.85$, and d) $F^+_{PUG} = 1.25$ large disturbance cases

All of the plots in Figure 4.7 have a peak at $F^+ = 0.41$, which is a common frequency found when other researchers analyzed the flow in a similar setup [9, 20, 25, 26]. All significant amount of harmonic behavior was detected here. The baseline case shows multiple peaks at $F^+ = 0.41$ and its multiples 0.82, 1.60, and 2.46. Additionally, all the PUG pulsing cases had peaks at their actuation frequency, along with its multiples. This indicates that the leading-edge disturbances are influencing V_y in the spatial region containing the PV. The exact influence and its extent can be determined by similarly analyzing the fluctuation in Q-criterion with time.

The instantaneous maximum Q-criterion is assumed to be associated with the strength of the vortex. If this value increases, then the vortex gained strength. If this value

decreases, then the vortex becomes weaker and will potentially experience a loss of coherence event. The maximum value across the time domain was tracked and used to generate the PSD plot in Figure 4.8. These were constructed using the same analysis as Figure 4.5, except the V_y, was replaced by the maximum Q-criterion time signal. The $F^+_{PUG} = 1.25$ cases looked identical, which is why only the large case is shown in Figure 4.8. Plotting multiple PSD plots was utilized to show different features. PSD plots in Figure 4.7 that were created using V_y, at the time averaged location of the PV showed noticeable peaks at the pulsing frequency, and it reflected the common F^+ of 0.4 that other researchers had reported [9, 20, 25, 26]. PSD plots shown in Figure 4.8 were utilized to determine frequencies associated with the PV strength changes, such as when the PV loses coherence.

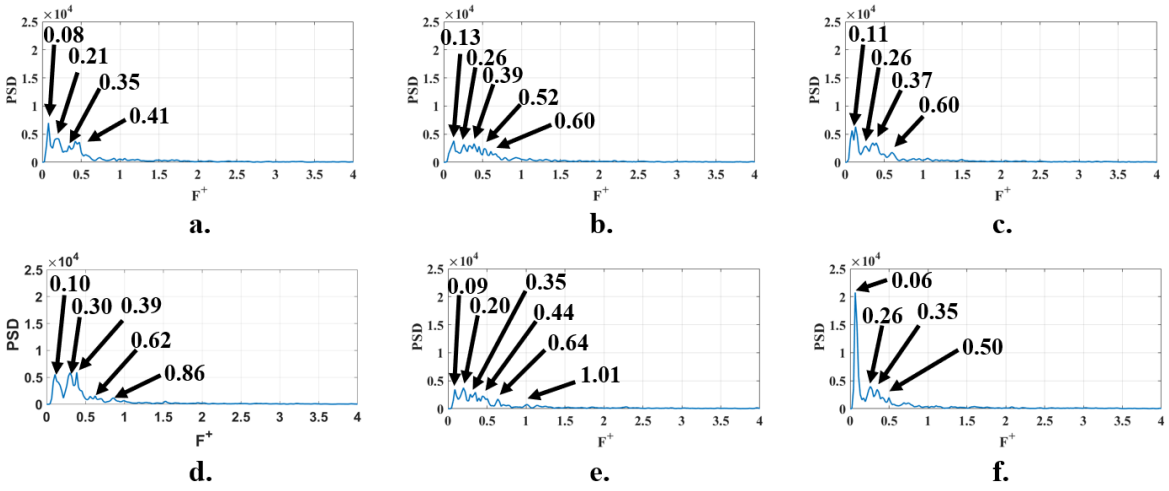

Figure 4.8 PSD using Welch's method of the maximum Q-criterion value at each instance in time for a) baseline case, b) $F^+_{PUG} = 0.41$ small disturbance case, c) $F^+_{PUG} = 0.85$ small disturbance case, d) $F^+_{PUG} = 0.41$ large disturbance case, e) $F^+_{PUG} = 0.85$ large disturbance case, and f) $F^+_{PUG} = 1.25$ large disturbance case

For the baseline case, four primary peaks appeared here with no substantial peaks beyond $F^+ > 0.5$. Similar behavior was found for both small and large cases at $F^+_{PUG} = 1.25$. The $F^+ = 0.4 - 0.5$ peaks appear to correspond to the time for one undulation where the PV moves from the PS to the SS and back to the PS. This undulation occurs over a

period of 2-2.5 convective times and can be visualized by analyzing the peaks in Figure 4.8. Peaks at these frequencies also appear in Ref. 8, 14, 20, and 24. Typically, this event repeats two or three times in a row, which corresponds to the peaks at $F^+ = 0.2 - 0.3$. These ranges of peaks are present for all of the cases, which means that this behavior was present for all the cases. The small and large $F^+_{PUG} = 0.41$ and 0.85 cases showed more unique characteristics. These cases had more peaks scattered over a wider range of frequencies. The peak around $F^+ = 0.6$ was present for all these cases, which represents the average time between the two successive undulations from the PS to the SS and back, and the duration of one complete undulation from the PS to the SS and back towards the PS. This frequency being present for these cases is largely attributed to the increase in frequency of two successive undulations occurring in very close proximity over a short period. Figure 4.9 show examples of these shorter undulations in these cases for both pulsing cases.

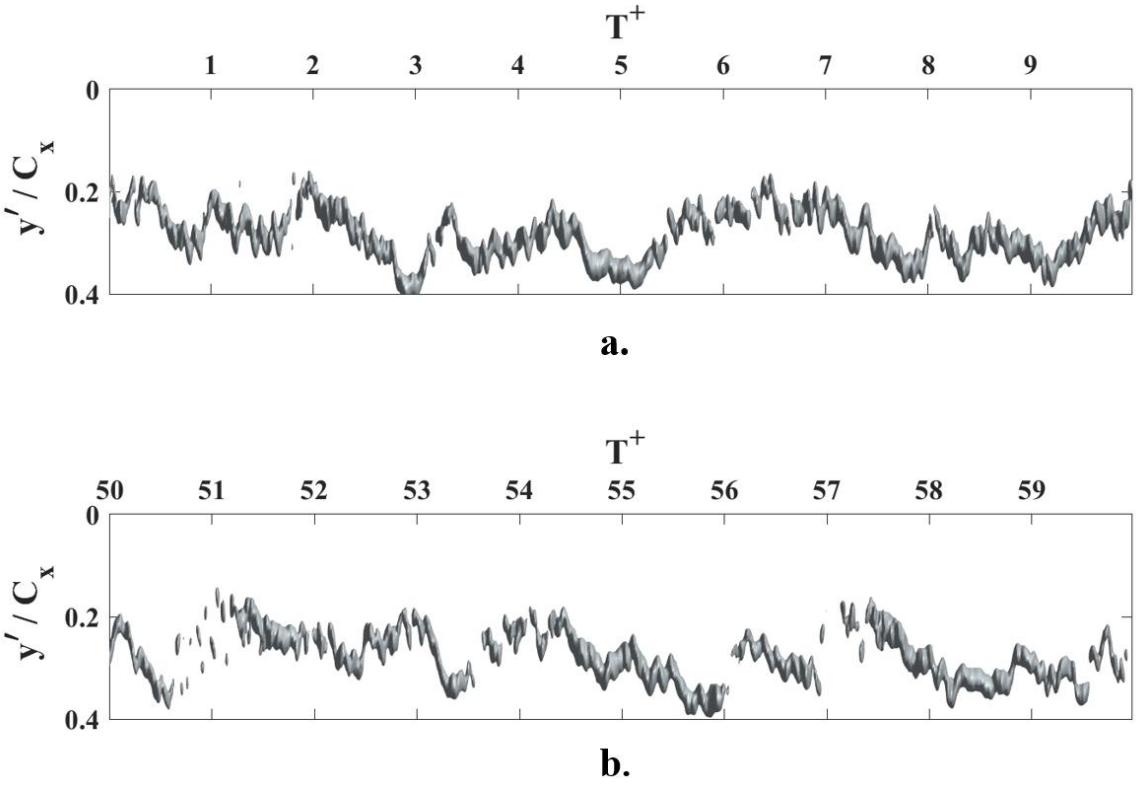

Figure 4.9 Space-time plot of isosurfaces of $Q = 100$ for the large disturbance cases at F^+_{PUG} = a) 0.41 and b) 0.85

The baseline case shows some examples of this behavior, but it also shows periods of extended loss of coherence events or long durations of coherent structure with short, brief undulations. This causes the very slight peak in the PSD, without it being substantial enough to be labeled. The peaks in the large disturbance cases at $F^+ = 0.86$ and 1.01 for $F^+_{PUG} = 0.85$ and 1.25, respectively, correspond to the average duration of loss of coherence events. Figure 4.10 shows examples of these shorter loss of coherence events occurring for these pulsing frequencies. Figure 4.10a shows the $F^+_{PUG} = 0.41$ large case with two short loss of coherence events, each with a period of around 1-1.2 convective times. Figure 4.10b shows the $F^+_{PUG} = 0.85$ large case with three short loss of coherence events. The first event takes place at the start of the space-time, and it has a period of about

1-1.2. The second and third events take place near $T^+ = 95$, and they both have a period of about 1.

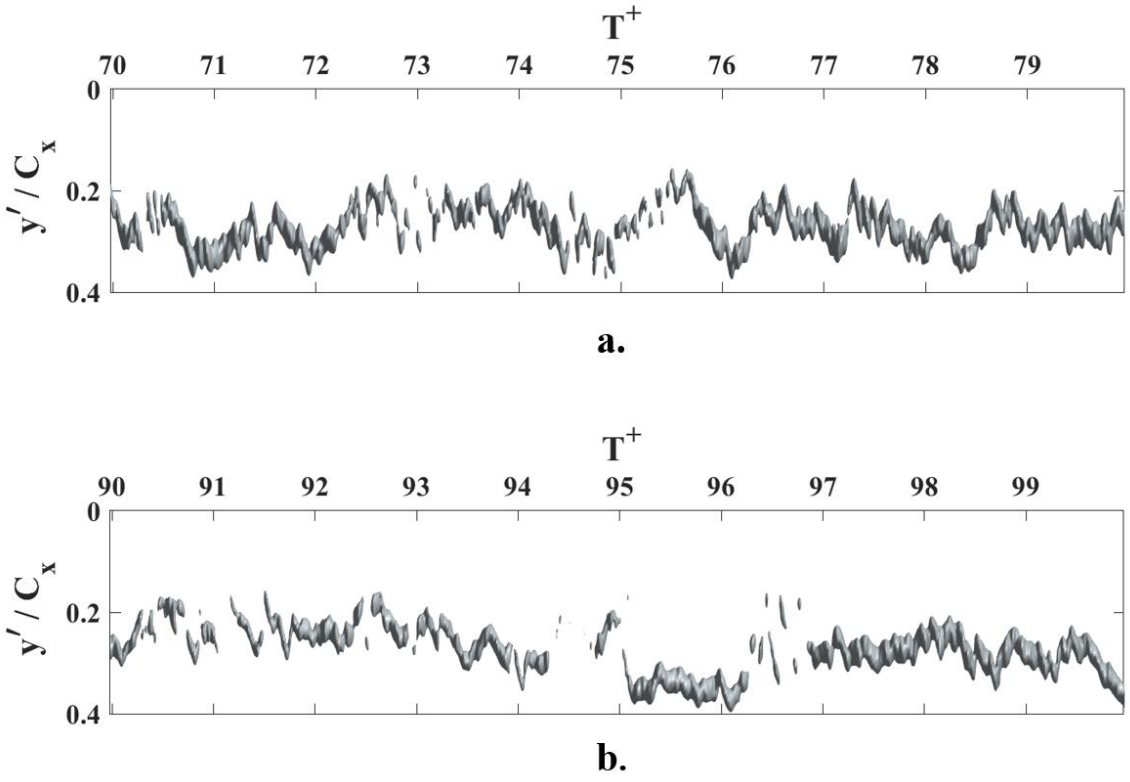

Figure 4.10 Space-time plot of isosurfaces of $Q = 100$ for the large disturbance cases at F^+_{PUG} = a) 0.41 and b) 0.85

The VITA method was utilized to determine its effectiveness at identifying events in the flow, and to help identify how upstream periodic unsteadiness impacted the frequency and duration of loss of coherence events. The convective time between these events were calculated and plotted as histograms. Figure 4.11 shows the histogram plots of the time between VITA detections for the baseline case and $F^+_{PUG} = 0.41, 0.85$, and 1.25 large disturbance cases. All four histograms show a bimodal distribution with one peak occurring around $\Delta T^+ = 0.5$ ($F^+ = 2$). The second peak appears to be different depending on pulsing frequency of the PUG. For the baseline case, the second peak occurs near

$\Delta T^+ = 2.25$ ($F^+ = 0.44$), and, as the pulsing frequency increases, the second moves closer to $\Delta T^+ = 3$. The small disturbance plots closely resemble the large disturbance plots, so they were not included.

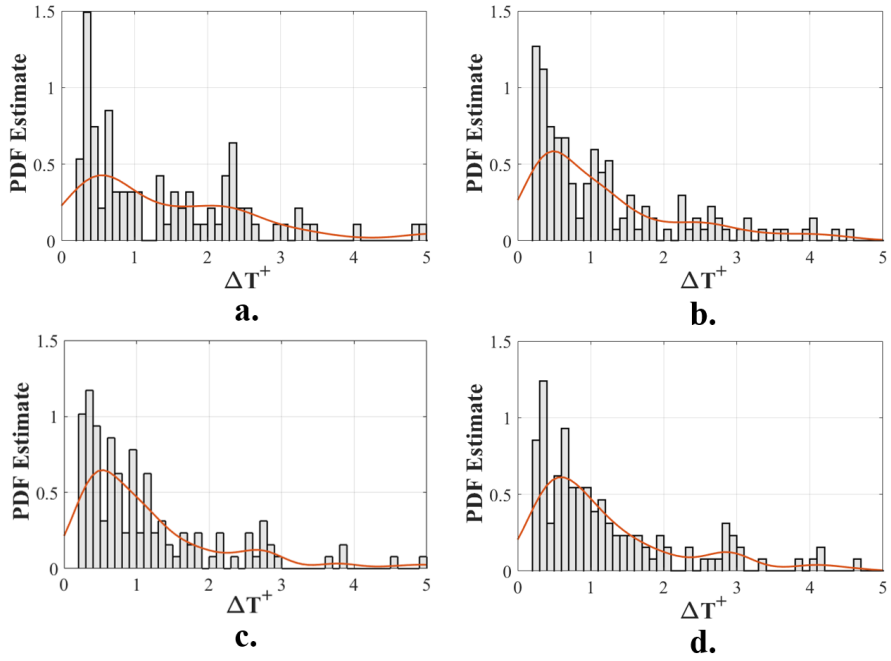

Figure 4.11 Histogram of the time between VITA detections (ΔT^+) with a line of best fit for a) baseline case, b) $F^+_{PUG} = 0.41$ c) $F^+_{PUG} = 0.85$, and d) $F^+_{PUG} = 1.25$ large disturbance cases

Table 4.1 summarizes the statistical results based on loss of coherence events detected by the VITA method. The median and mean time period between events is listed, along with the frequency for each quantity. To accompany the VITA method results, the space-time plots for $Q = 100$ were analyzed for the period range of incoherence, and short and long undulations. These results are shown in Table 4.2. The VITA method results were primarily focused on characterizing the loss of coherence events, and the space-time plot analysis determined ranges of periods and frequencies associated with three primary characteristics of the PV: the duration of incoherence, the period for short undulations, and

the period for long undulations. For these results, short undulations are considered to be $T^+ \leq 1.0$ with long undulations classified as having a period $T > 1.0$.

Table 4.2 VITA method results

Case	Size of Disturbance	median(ΔT^+)	F^+_{Median}	mean(ΔT^+)	F^+_{Mean}
Baseline	-	1.02	0.980	1.57	0.637
$F^+_{PUG} = 0.41$	Small	1.00	1.00	1.54	0.649
$F^+_{PUG} = 0.85$		1.01	0.990	1.40	0.714
$F^+_{PUG} = 1.25$		0.987	1.01	1.51	0.662
$F^+_{PUG} = 0.41$	Large	0.919	1.09	1.26	0.794
$F^+_{PUG} = 0.85$		0.854	1.17	1.21	0.826
$F^+_{PUG} = 1.25$		0.880	1.14	1.29	0.775

Table 4.3 Summary of vortex unsteady events using space-time Q-criterion=100 plots

		T^+			F^+	
F^+_{PUG}	Size	Duration of Incoherence	Undulation – short period	Undulation – long period	Undulation – short period	Undulation – long period
$F^+ = 0$	-	0.2-1.0 typical, as long as 2.0	0.2-0.7	1.4-3.5	1.4-5.0	0.3-0.7
$F^+ = 0.41$	Small	0.2-0.8 typical, as long as 1.8	0.2-1.0	1.4-3.6	1.0-5.0	0.3-0.7
$F^+ = 0.85$		0.2-1.0 typical, as long as 1.8	0.2-0.8	1.2-3.2	1.2-5.0	0.3-0.8
$F^+ = 1.25$		0.2-1.0 typical, as long as 1.8	0.2-1.0	1.5-3.0	1.0-5.0	0.3-0.7
$F^+ = 0.41$	Large	0.2-1.4 typical, as long as 2.0	0.2-1.0	1.4-3.0	1.0-5.0	0.3-0.7
$F^+ = 0.85$		0.2-2.0 typical, as long as 3.6	0.2-1.0	1.2-2.6	1.0-5.0	0.4-0.8
$F^+ = 1.25$		0.2-1.6 typical, as long as 3.0	0.2-1.0	1.4-3.0	1.0-5.0	0.3-0.7

For each pulsing case, the median and average time between VITA detections decreased compared to the baseline result. The small cases had a substantially smaller change in these values, which makes sense because the small cases had a minor impact on the size and strength of the PV. The $F^+_{PUG} = 0.41$ and 0.85 small cases histograms (not

shown) closely resembled the trend in behavior from the baseline case, but the $F_{PUG}^{+} = 1.25$ showed an increase in the frequency of loss of coherence events with no consistent trend. The large cases showed a decrease in the median and average time between VITA detections, signifying that these cases had a higher frequency of loss of coherence events. There appears to be a nonlinear trend for the large disturbance cases where increasing the pulsing frequency did not always increase the median/mean time between detections, which is evident by comparing the large cases. By examining the vortex tracking plots, like the ones shown in Figures 4.9 and 4.10, these revealed that the large cases caused the loss of coherence events to happen more frequently, which decreases the average time the PV was coherent. At $F_{PUG}^{+} = 0.41$, the disturbances caused slightly higher frequency of a loss of coherence event occurring and a slightly lower average durationfor the loss of coherence events. At $F_{PUG}^{+} = 0.85$, the disturbances caused a slightly higher frequency of a loss of coherence event occurring, but it substantially reduced the average period of the loss of coherence events. This disturbance case typically lengthened the duration of loss of coherence events occurring after the PV shifts from the PS towards the SS. At $F_{PUG}^{+} = 1.25$, the disturbances substantially increased the frequency of a loss of coherence event occurring with no consistent trend, and it slightly decreased the average period of loss of coherence events. Both $F_{PUG}^{+} = 1.25$ disturbances caused an increase in the frequency of loss of coherence events, but it did not show any consistent pattern for when these loss of coherence events occurred.

Overall, the $F_{PUG}^{+} = 0.85$ case had the longest period of total loss of coherence events, which explains why the median and mean time between VITA detections was the lowest, but it did not show any lock-on or consistent behavior. The PV showed temporary

periods of consistent behavior, whether that be long durations of a loss of coherence or long duration of minimal shifts in location.

5 Surface-Mounted Hot-film

5.1 Hot-film Results

Surface-mounted hot-film data was gathered to help connect flow phenomena at the LE to the secondary flow in the passage. Figure 5.1 shows the film signals for the $F_{PUG}^{+} = 0$ baseline case across ten convective times. These plots can be useful in showing the spread and variability of fluctuations for each sensor across a short time period. The large fluctuations in the signal are signatures of fluid dynamic features. For example, the signals from the LE sensors EW2a and EW2b show a small range for the voltage output but high variability in this short time i.e. these readings show heavy amounts of small, short changes in voltage. These sensors show the highly chaotic behavior of the flow at the LE. The sensors in the passage (EW4a-f) each have their unique characteristics based off their proximity to the PV. Sensors EW4a, EW4e, and EW4f all show a small range for voltage output and low variability since their voltage output remains relatively steady with slow changes occurring over an extended time. These sensors are positioned close to the SS and the PS, which explains why these sensors are detecting fewer fluid dynamic structures: the PV remains close to the center region of the passage. Sensors EW4b, EW4c, and EW4d all show large spread with a small variability meaning that the dynamics captured by these signals are long relatively stable structures. These sensors capture the behavior of the PV,

and the signals shown below presents peaks at similar times suggesting that multiple sensors are detecting the same vortex.

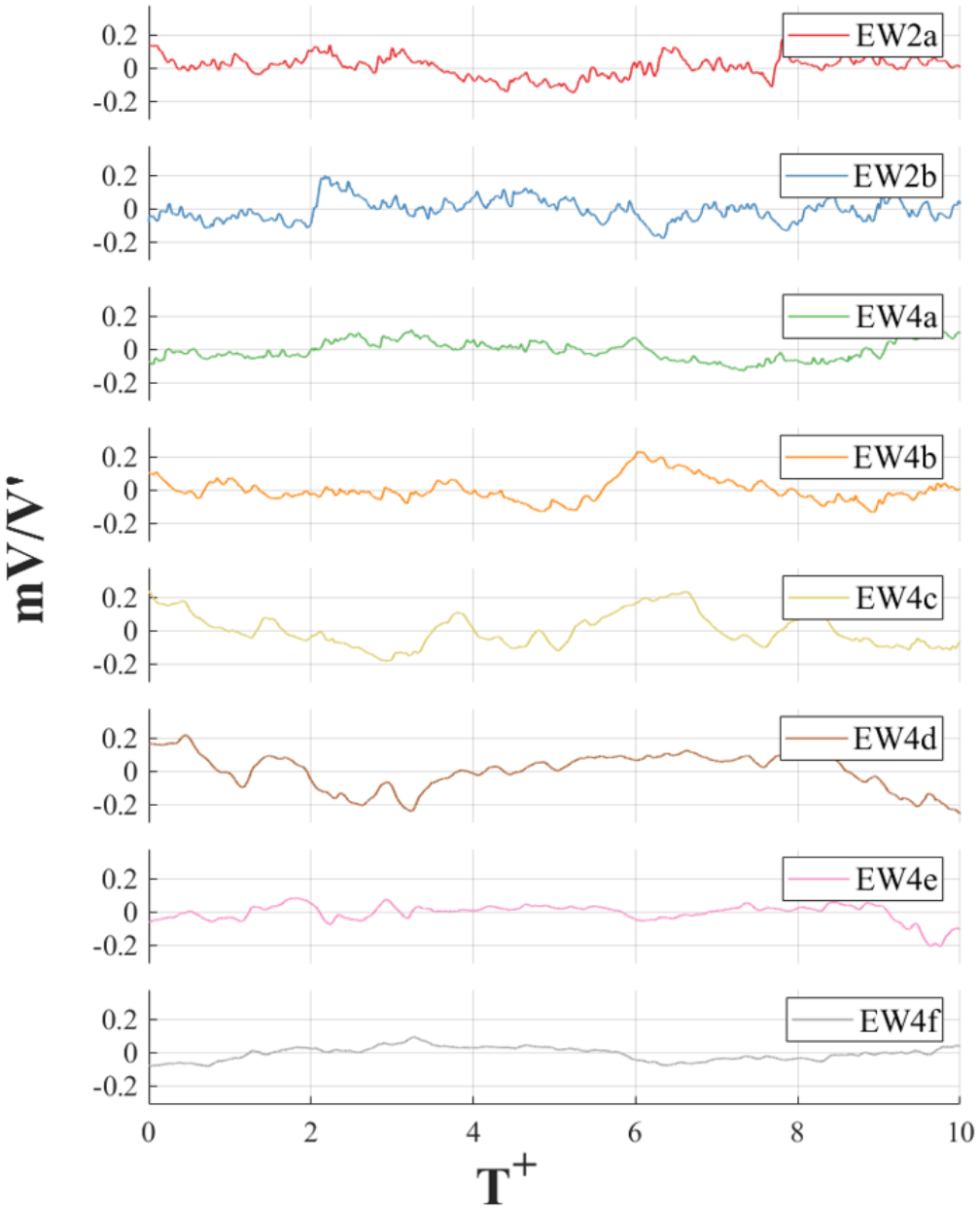

Figure 5.1 mV/V' output for $F^{+}_{PUG} = 0$ baseline case across 10 convective times

Because the $F^{+}_{PUG} = 0.85$ and 1.25 large disturbance cases showed the most impact on the PV behavior, these two cases were further studied with surface mounted hot-films. PSD plots were generated using the same approach as Figure 4.8 by taking the raw voltage

output from the hot-film sensors, breaking it into 4 groups, creating a Hamming window with the 4 groups, and then using Welch's method. This method was employed for both the EW2 and EW4 sensors. Figure 5.2 shows the PSD plots at EW2 for the baseline case. Note: sensor EW2a is furthest from the LE and EW2c is closest to the LE. Figure 5.2 shows that as the flow progresses closer to the LE, its periodic behavior diverges into fewer frequencies. At EW2a, there are 4 noticeable peaks, at EW2b there are three noticeable peaks, and at EW2c there are only 2 noticeable peaks. Also, since the junction flow is bimodal and switches between the backflow and zero-flow mode, the bimodal PSD distribution for sensor EW2c captures this behavior. The same peaks are present from sensor EW2b to EW2c, which likely means that these two sensors are capturing the same behavior in the flow.

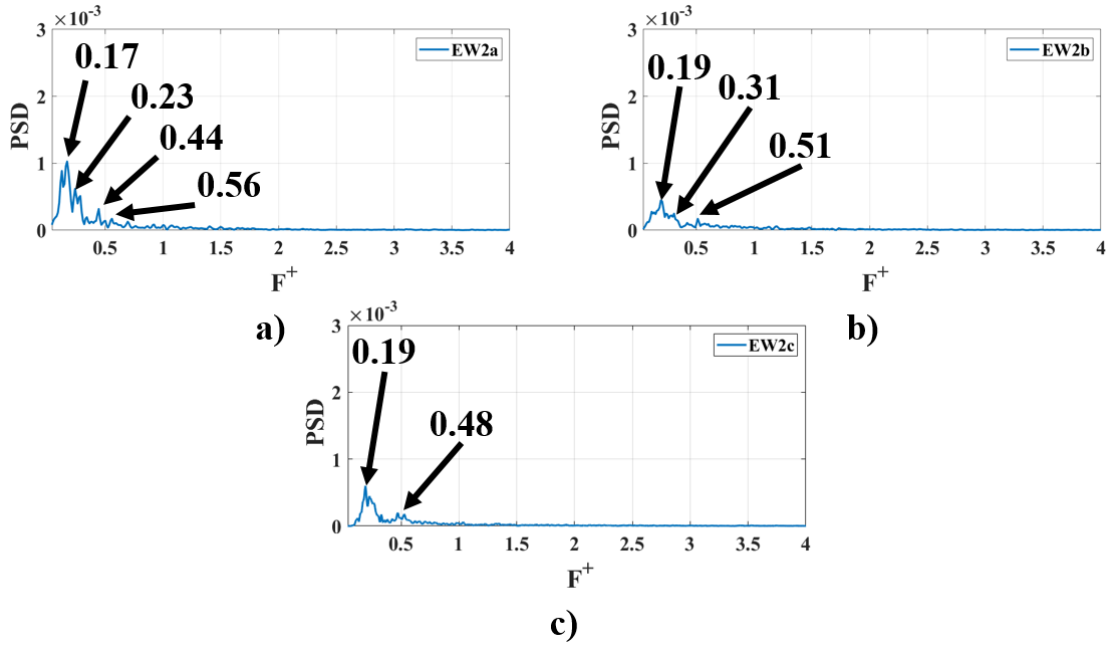

Figure 5.2 PSD from hot-film measurements for $F^+_{PUG} = 0$ baseline case at a) EW2a, b) EW2b, and c) EW2c locations

Figure 5.3 shows the PSD at the EW2 locations for the $F^+_{PUG} = 0.85$ large case. This case appears to have a strong impact on the flow near the EW2a sensor, but it only

has a minor impact on the sensors closer to the LE. All three PSD plots look very similar to the baseline case shown in Figure 5.3. The biggest differences are that EW2a shows a peak at $F^+ = 0.84$, which is likely caused by the pulsing frequency of the disturbance. Also, it appears that the size of the peak around $F^+ = 0.2$ at EW2c has reduce for this case. Other than these two small differences, these PSD plots show that the disturbance has a very minor impact on the junction flow. Also, the peaks common in sensor EW2b ($F^+ =$ 0.22 and 0.52), are still present in EW2c.

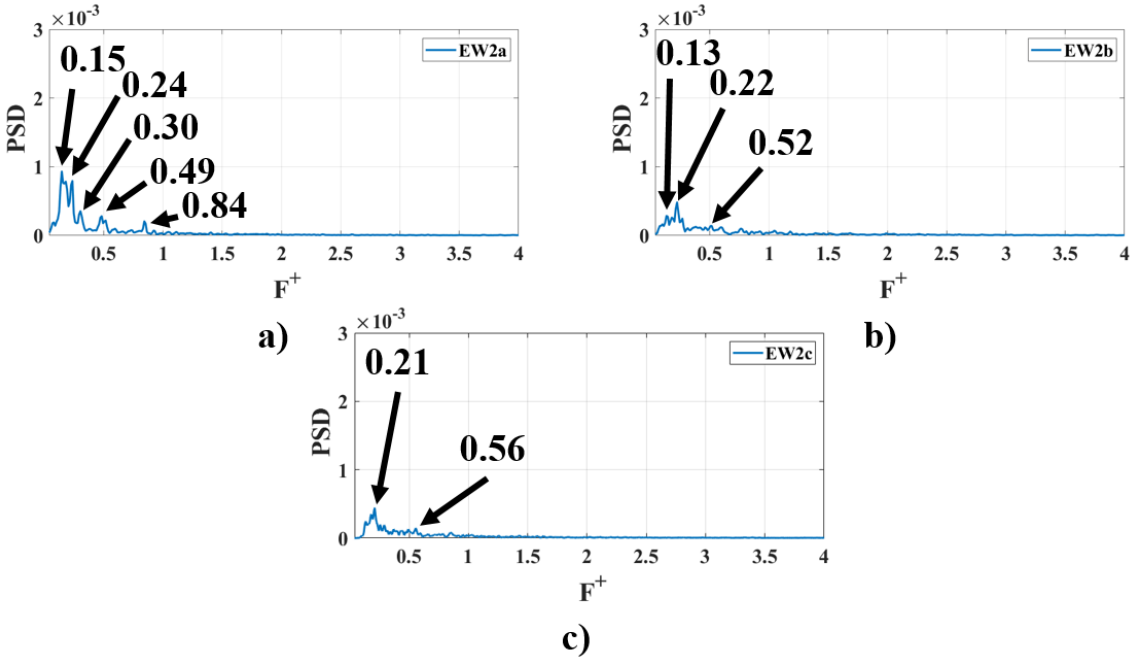

Figure 5.3 PSD from hot-film measurements for $F^+_{PUG} = 0.85$ large case at a) EW2a, b) EW2b, and c) EW2c locations

Figure 5.4 shows the PSD at the EW2 location for the $F^+_{PUG} = 1.25$ large case. These plots show a substantial change in behavior compared to the baseline case. Sensor EW2a shows the biggest change as most of the original peaks are gone and only two peaks remain. This is likely caused by the disturbance increasing the freestream turbulence intensity due to its high pulsing frequency and DC. At sensor EW2b (Figure 5.4b), this PSD plot looks similar to the baseline case, but two of the peaks, $F^+ = 0.19$ and 0.25, are

much closer together than they were in the baseline case. Also, these same peaks are present and dominating at sensor EW2c for this case, which deviates from the other cases. The other cases saw peaks around $F^+ = 0.2$ and 0.5 consistent for both the EW2b and EW2c sensors, but this case shows a peak at 0.25 consistently for EW2b and EW2c. Sensor EW2c still shows a bimodal distribution, but one of the frequencies are halved compared to the baseline and $F^+_{PUG} = 0.85$ large disturbance cases. Therefore, the $F^+_{PUG} = 1.25$ has a significant impact on the junction flow.

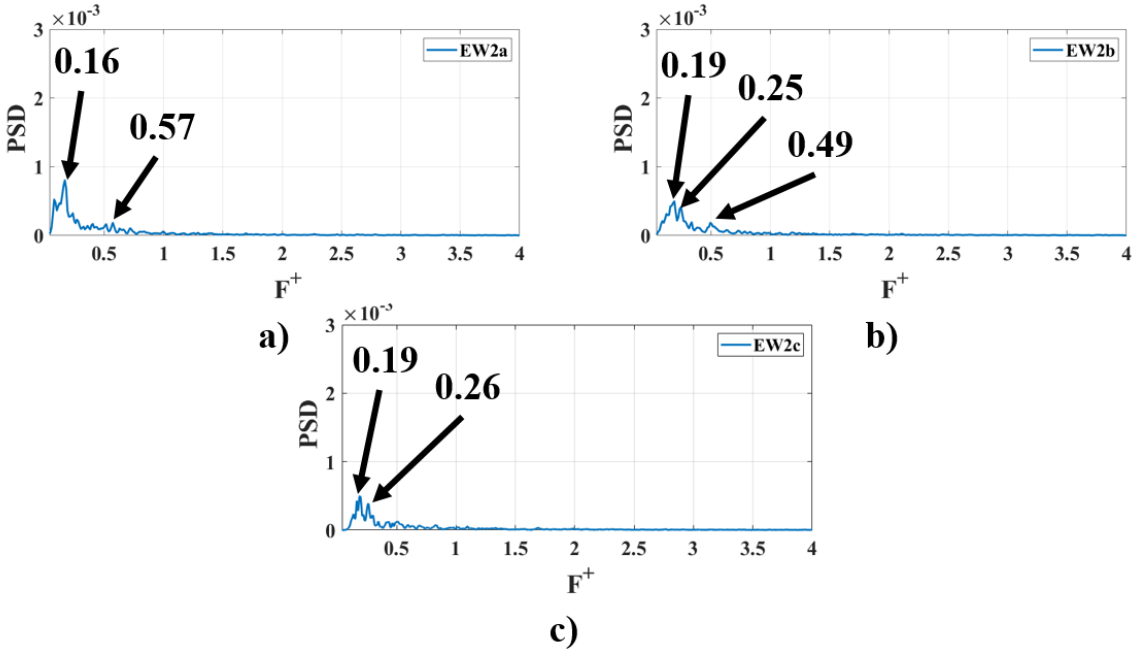

Figure 5.4 PSD from hot-film measurements for $F^+_{PUG} = 1.25$ large case at a) EW2a, b) EW2b, and c) EW2c locations

To help further compare the baseline case to the $F^+_{PUG} = 0.85$ and 1.25, the RMS and standard deviation of the signals were compared. The RMS of a measurement shows how much each single measurement in a data set changed value, and the standard deviation of a measurement looks at how far apart the spread of the measurement was. Figure 5.5a shows the computed RMS of the filtered voltage signal, and Figure 5.5b shows the computed standard deviation of the raw voltage signal for each case and sensor. The

sensors that show the largest deviation between cases are EW2a, EW2c, and EW4d. For sensor EW2a, the standard deviation showed that the baseline case had a substantially larger spread than the pulsing cases. This is by the pulsing cases creating more consistent flow behavior around this location. At sensor EW2c, the baseline case had lower RMS and standard deviation values compared to the pulsing cases, which means that the readings from the sensor changed more often and had a larger spread for the pulsing cases than the baseline case. This justifies that the pulsing cases are exciting the flow close to the LE and their influence on the PV might be linked to these changes. Sensor EW4d captures a large amount of the PV behavior because this in-passage sensor has the highest RMS and standard deviation values out of all nine sensors. The differences in the pulsing cases compared to the baseline case is likely linked to their impact on the PV. Both pulsing cases moved the time averaged position of the PV closer to the SS, where EW4a is closest to the SS. This might explain why the change in sensor value was lower for these cases: the PV passed over this sensor less often.

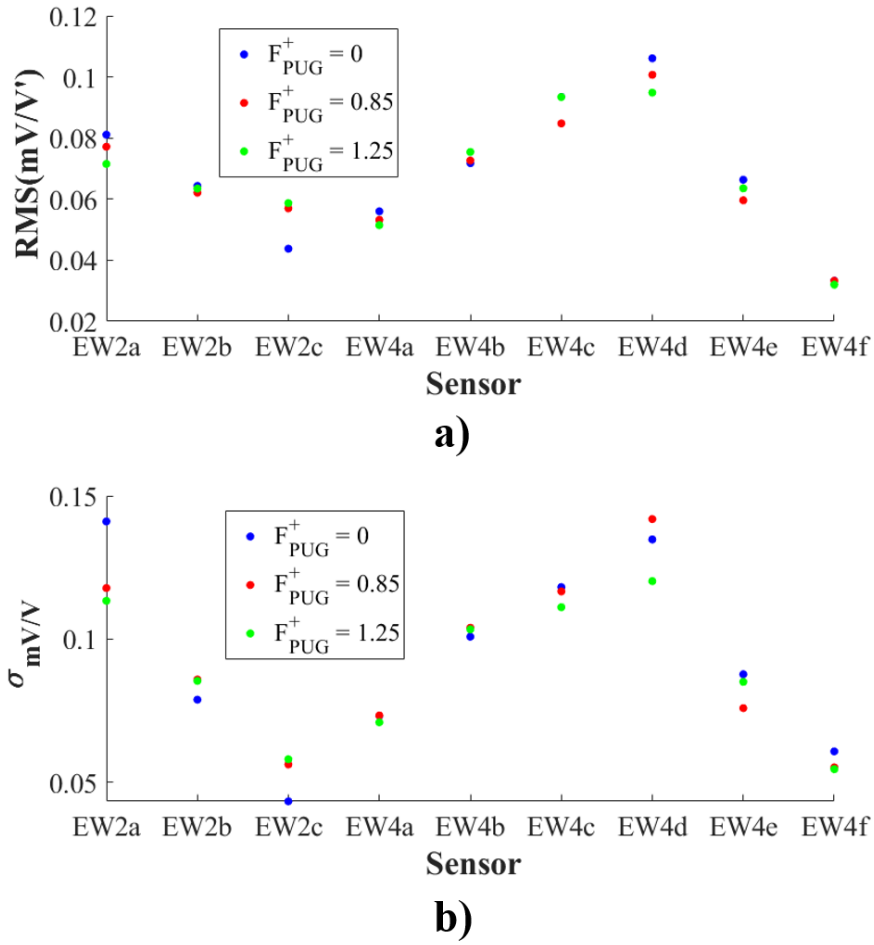

Figure 5.5 Plots comparing the a) RMS of the filtered voltage and b) standard deviation of the raw voltage signal for all surface mounted hot-films

All sensors at EW4 were analyzed by creating PSD plots using the same process as Figures 5.2-5.4. Sensors EW4a and EW4f showed minor peaks at very low frequencies, and, of the EW4 sensor array, Figure 5.5 shows sensors b-e captures the majority of fluid dynamic changes in the passage likely caused by the PV. Note that sensor EW4a is closest to the SS and EW4f is closest to the PS, which is explains why these sensors are not detecting rapid, large shifts in the fluid dynamics behavior close by. The resulting plots for the $F^+_{PUG} = 0$ baseline case is shown in Figure 5.5. Peaks at $F^+ = 0.2, 0.26$, and 0.4 are common across all four sensors, which likely indicates that the same fluid dynamic behavior is consistent across all four sensors. Only sensors EW4c and EW4d show peaks

at $F^+ = 0.54$, and only sensor EW4c shows a peak at $F^+ = 0.82$. From the SPIV analysis, the PV spends a majority of its time around these sensors, and that can be verified by Figure 5.5 above. These two sensors have the largest RMS and standard deviation values, and, since the dominating flow feature in the passage is the PV, these sensors are largely detecting the PV behavior. Figure 4.8a shows the PSD plots for the maximum Q-criterion value, which looks similar to Figure 5.6a and 5.6d. The four clear frequencies from that analysis were 0.08, 0.21, 0.35, and 0.41, but only the frequencies of 0.21 and 0.41 are measured by the hot-film sensors. Frequencies 0.08 and 0.35 may still be capturing PV behavior, but the hot-film sensors cannot detect all of the PV behavior, especially when it moves higher in the spanwise direction toward MS since the sensors are attached to the endwall. From previous analysis, the reduced frequencies close to 0.2 and 0.4 were associated with the PV undulations, which is likely what these sensors are detecting here as well.

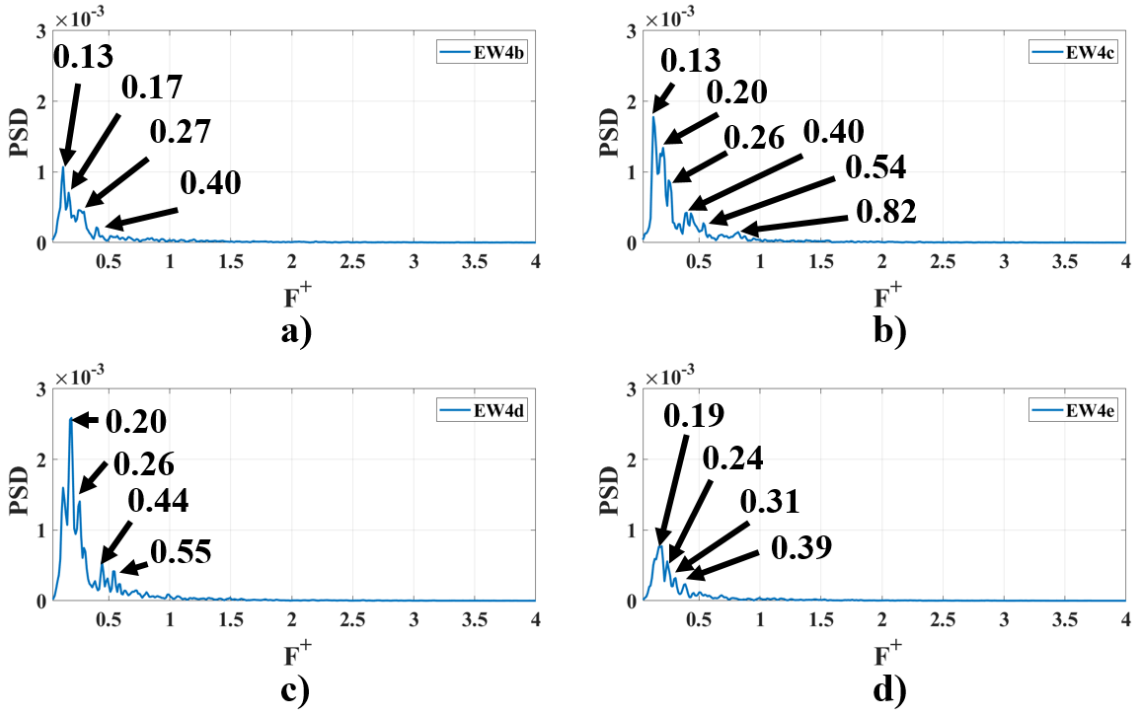

Figure 5.6 PSD from hot-films at EW4 for $F^+_{PUG} = 0$ baseline case at a) EW4b, b) EW4c, c) EW4d, and d) EW4e

Figure 5.7 shows the PSD plots for the $F^+_{PUG} = 0.85$ large case for sensors EW4b-e. Similar to the baseline case, these sensors had common frequencies of $F^+ = 0.2$ and 0.45 detected by all four sensors. Additionally, the frequency of 0.64 is noticeable in Figures 5.7b and 5.7c corresponding to sensors EW4c and EW4d, which are located closest to region of the time averaged position of the PV. All three of these frequencies were detected in Figure 4.8e, and all three are believed to correspond to the undulations of the PV. Sensors EW4b and e detect the two common frequencies, with sensor EW4b also detecting a peak at $F^+ = 0.13$. This was also detected in Figure 5.6a and 5.6b for the baseline case, and it depicts an attribute of the fluid dynamic behavior occurring close to the SS since that frequency is not observable at the other sensors.

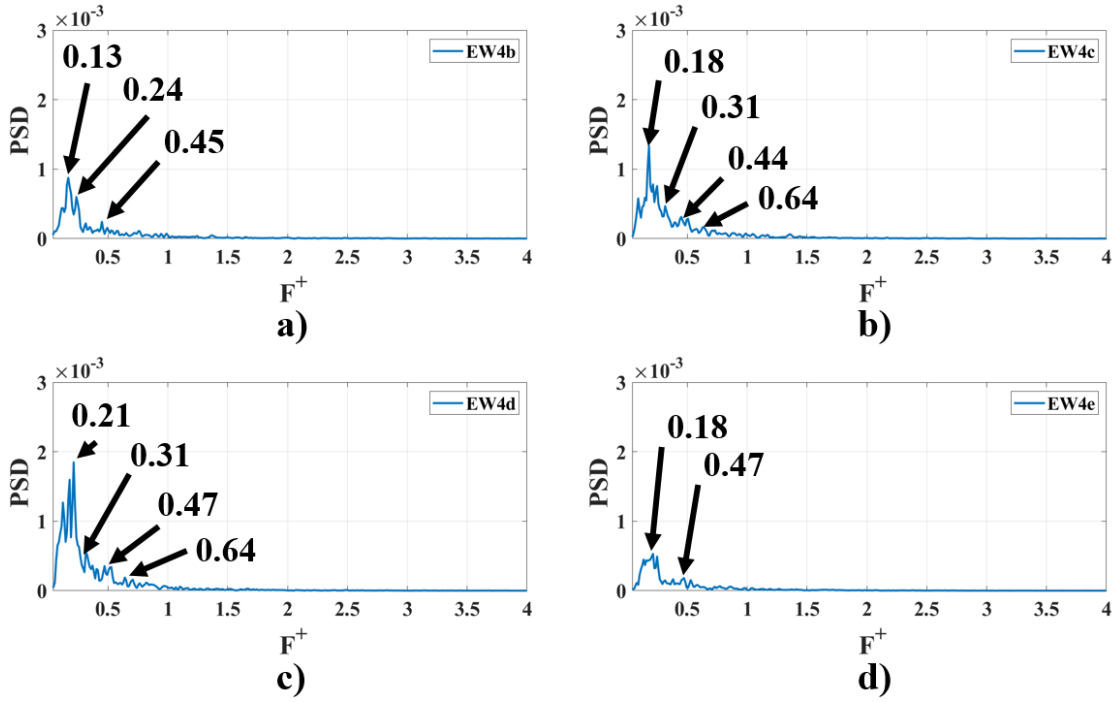

Figure 5.7 PSD from hot-films at EW4 for $F^+_{PUG} = 0.85$ large case at a) EW4b, b) EW4c, c) EW4d, and d) EW4e

Figure 5.8 shows the PSD plots for $F^+_{PUG} = 1.25$ large case for sensors EW4b-e. For this pulsing case, there are three consistent frequencies of 0.15, 0.24, and 0.54 are appear in all four sensor PSD plots, but the reduced frequency of 0.15 did not appear in Figure 4.8f. This behavior deviates from the other two cases, where all of the common frequencies also appeared in the PSD plots for maximum Q-criterion. From Figure 5.8, this frequency is the most apparent frequency for all the sensors, except EW4c as it is the second largest peak, which means this behavior is not associated with the strength of the PV. Since the reduced frequencies of 0.24 and 0.54 are common for both PSD analysis methods, that means the hot-film sensor is detecting reductions in the PV strength.

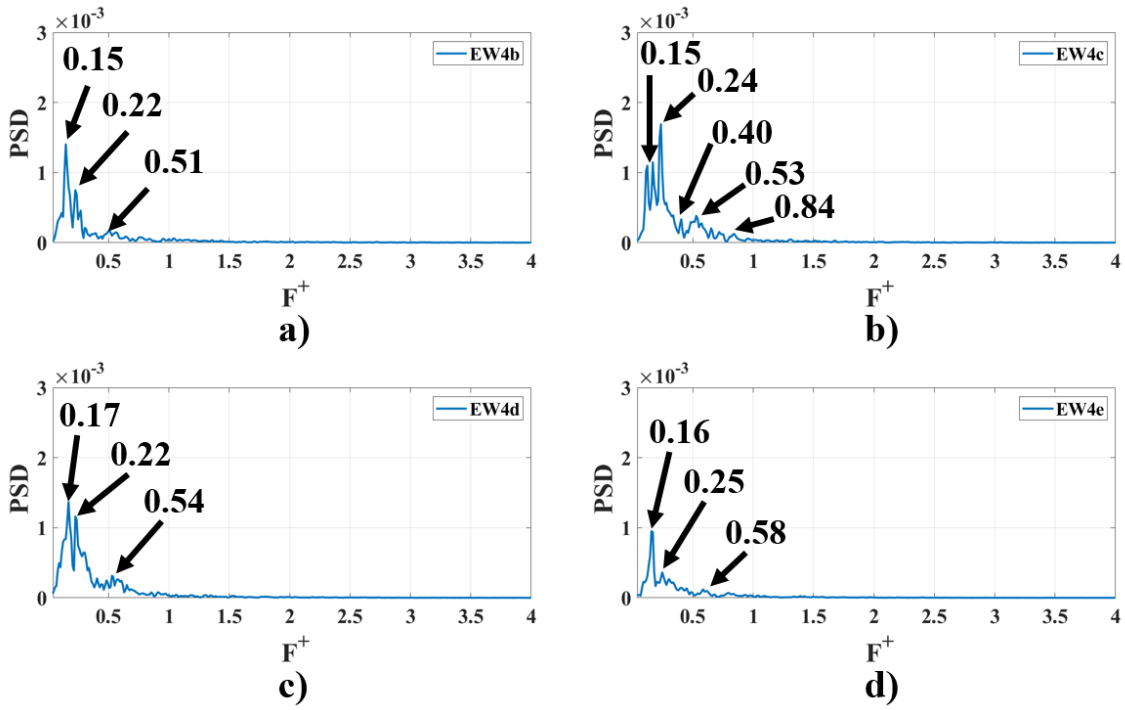

Figure 5.8 PSD from hot-films at EW4 for $F^+_{PUG} = 1.25$ large case at a) EW4b, b) EW4c, c) EW4d, and d) EW4e

The PSD analysis for all three cases using sensors at EW4 reveals that the hot-film sensors are able to detect when the PV loses strength. All of the common frequencies for all four sensors, except for $F^+_{PUG} = 1.25$ with a peak at $F^+ = 0.15$, also had notable peaks in the PSD analysis for the maximum Q-criterion. This commonality means that the hot-films are able to capture when the PV loses strength, and all of the frequencies were determined to be connected to undulations of the PV. These undulations also commonly capture loss of coherence events, as they most frequently occur when the PV moves from the PS to the SS. Therefore, the hot-film sensors are able to capture loss of coherence events with the PV in their current configuration.

An important aspect of measuring the upstream EW2 sensor array with the EW4 sensor array was being able to use cross-correlation techniques to approximate the time it takes the disturbance to propagate from one of the LE sensors (EW2) to the in-passage

sensors (EW4). This analysis can help approximate how long the LE has to recover from the disturbance impacting the junction flow in terms of convective times and approximate the velocity in the endwall region. Additionally, a phase lag can be calculated that can be used to enhance the analysis of concurrent SPIV and hot-film measurements since the sensors are 10 mm downstream of the SPIV plane. Cross-correlation is a method of signal processing used to evaluate the similarity of two series as a function of the displacement of one relative to the other. In essence, this method determines the time between one sensor measuring a value, and the other sensor measuring a similar value. The disturbance should illicit a change in fluid behavior at the EW2 sensors, that causes some type of similar response from the EW4 sensor array. Cross-correlation analysis should be able to identify these similar responses and determine the average time delay between them.

For this analysis, sensors EW2a and b, and EW4c and d were analyzed. The results showed cross-correlating sensor EW2b with either EW4 sensor did not produce clear peaks at convective times close to one. Figure 5.9 shows the cross-correlation results for sensor EW2b to EW4d. Here the largest peak occurs at $T^+ = 0.1$ meaning that there is a delay of 0.1 convective times between EW4d experiencing a similar signal as EW2b. This is inaccurate since it implies that sensor EW2b and EW4d are much closer together than they are. Results for sensor EW2b to EW4c showed similar results, which is why sensor EW2b is not used for this analysis.

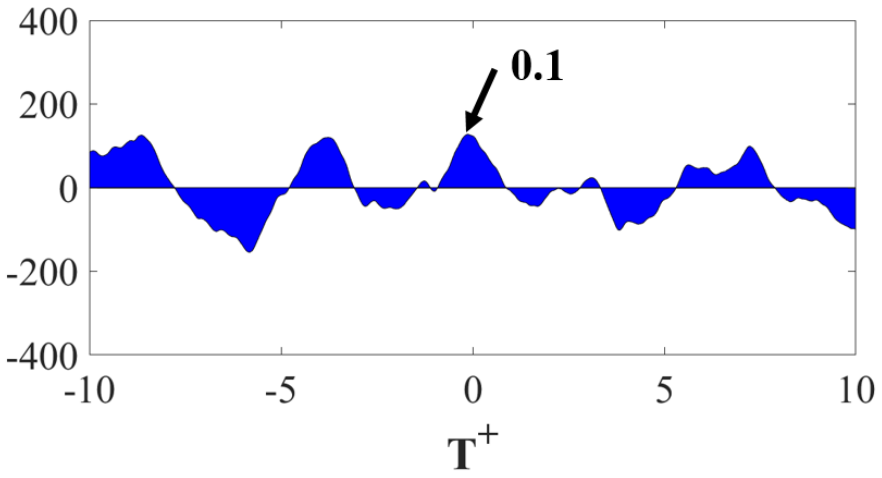

Figure 5.9 Cross-correlation results using sensor EW2b to EW4d for $F^{+}_{PUG} = 0$ baseline case

Cross-correlation results using sensor EW2a and sensors EW4c and d produced very similar results. Both EW4 sensors show peaks in similar location with a minimal difference in the result. Figure 5.3a showed that sensors EW4c-d have the largest RMS and standard deviation values out of all 8 sensors tested. This explains why either of these sensors can be used for the cross-correlation analysis. Figure 5.10 shows the cross-correlation for senor EW2a to EW4d. For values at $T^+ < 0$, sensor EW2a leads sensor EW4d, and, for values at $T^+ > 0$, sensor EW2a lags behind sensor EW4d. The distance from sensor EW2a to EW4d is 0.166 m. The peak at $T^+ = -1.05$ means that the estimated velocity in the endwall region is around $0.8U_\infty$. The cross-correlation producing a negative value here might be caused by the sensors reading opposite sign voltages, but they are consistently separated by a period of 1.05.

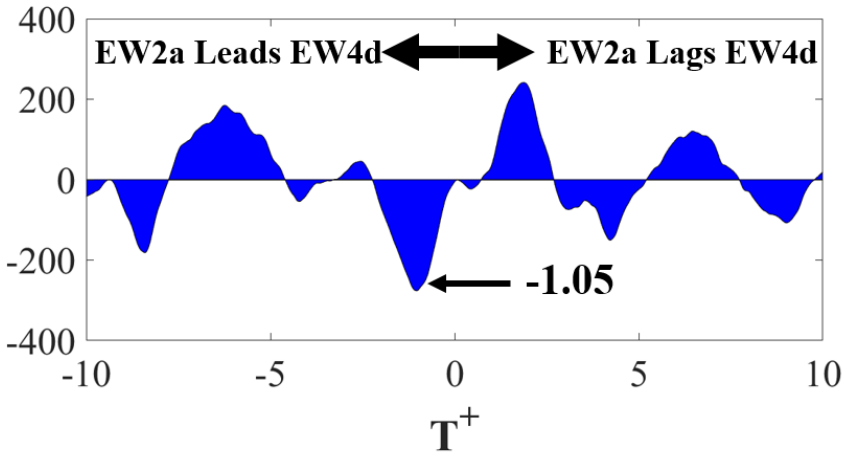

Figure 5.10 Cross-correlation results using sensor EW2a to EW4d for $F^+_{PUG} = 0$ baseline case

Figure 5.11 shows the cross-correlation results for the time lag between sensors EW2a and EW4d at $F^+_{PUG} = 0.85$ large case. The largest and most logical peak occurs at $T^+ = -1.15$, which means that sensor EW2a at the LE leads sensor EW4d in the passage. With this time delay, the velocity in the endwall region can be approximated to be $0.75U_\infty$. A peak at $T^+ = 1.15$ also corresponds to a frequency of 0.85, which is the pulsing frequency in this case. This likely means the sensors are capturing the disturbance at both locations and is reflecting the time from the disturbances. Figure 3.20 shows a line plot of U' and turbulence intensity across time at the LE, which shows a period of 1.15.

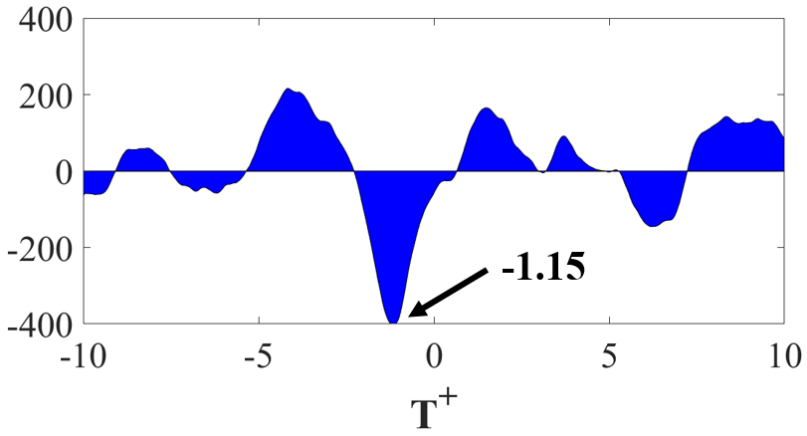

Figure 5.11 Cross correlation results using sensors EW2a and EW4d for the time lag for $F^+_{PUG} = 0.85$ large case

Figure 5.12 shows the cross-correlation results using the same two sensors as above, but for $F^+_{PUG} = 1.25$ large case. The higher pulsing frequency caused the time lag between sensors to increase to $T^+ = -1.33$, which is approximately $0.65U_\infty$. This time corresponds to a frequency of 0.75 The higher phase lag for a higher pulsing case may be caused by the constant change in velocity, turbulence intensity, and spanwise vorticity effectively increasing the FTSI at the LE shown by Figure 3.20. Therefore, the hot-film sensors are struggling to detect the actuation frequency at the LE, shown by Figure 5.10. The difference in time delay is likely caused by the high-pulsing frequency creating a time-averaged change in the fluid dynamic behavior at the LE and in the passage by essentially elevating the FSTI. This period does not match the disturbance period, which is around 0.8.

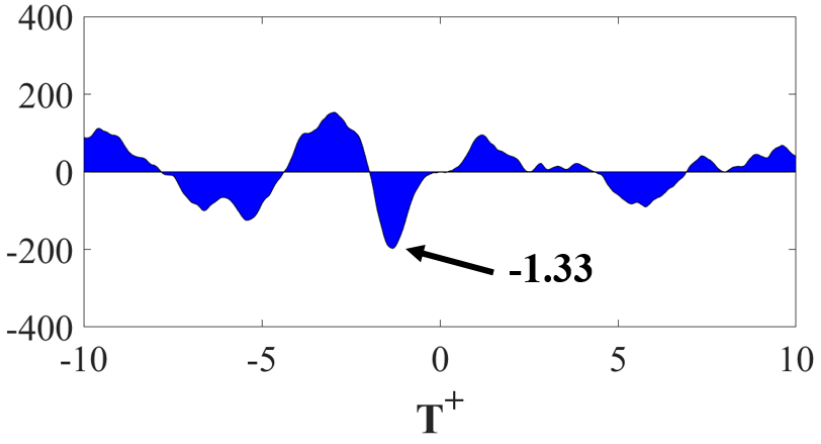

Figure 5.12 Cross correlation results using sensors EW2a and EW4d for the time lag for $F^+_{PUG} = 1.25$ large case

5.2 Simultaneous Hot-film and SPIV Results

Simultaneous surface-mounted hot-film and SPIV results were analyzed to determine the effectiveness of hot-films for investigating loss of coherence events. Q-criterion isosurfaces were also plotted to verify the PV location and its coherence level. Figure 5.13 shows the collection of pitchwise and spanwise space-time plots of $Q = 100$

along with the hot-film results that includes the maximum Q-criterion location plotted as the black line. The spanwise space-time plots are important to show when the PV lifts off the endwall, which can influence the sensor signals. These plots show false loss of coherence events due to the view. That is why the pitchwise space-time plot can be used to verify if the PV loses coherence.

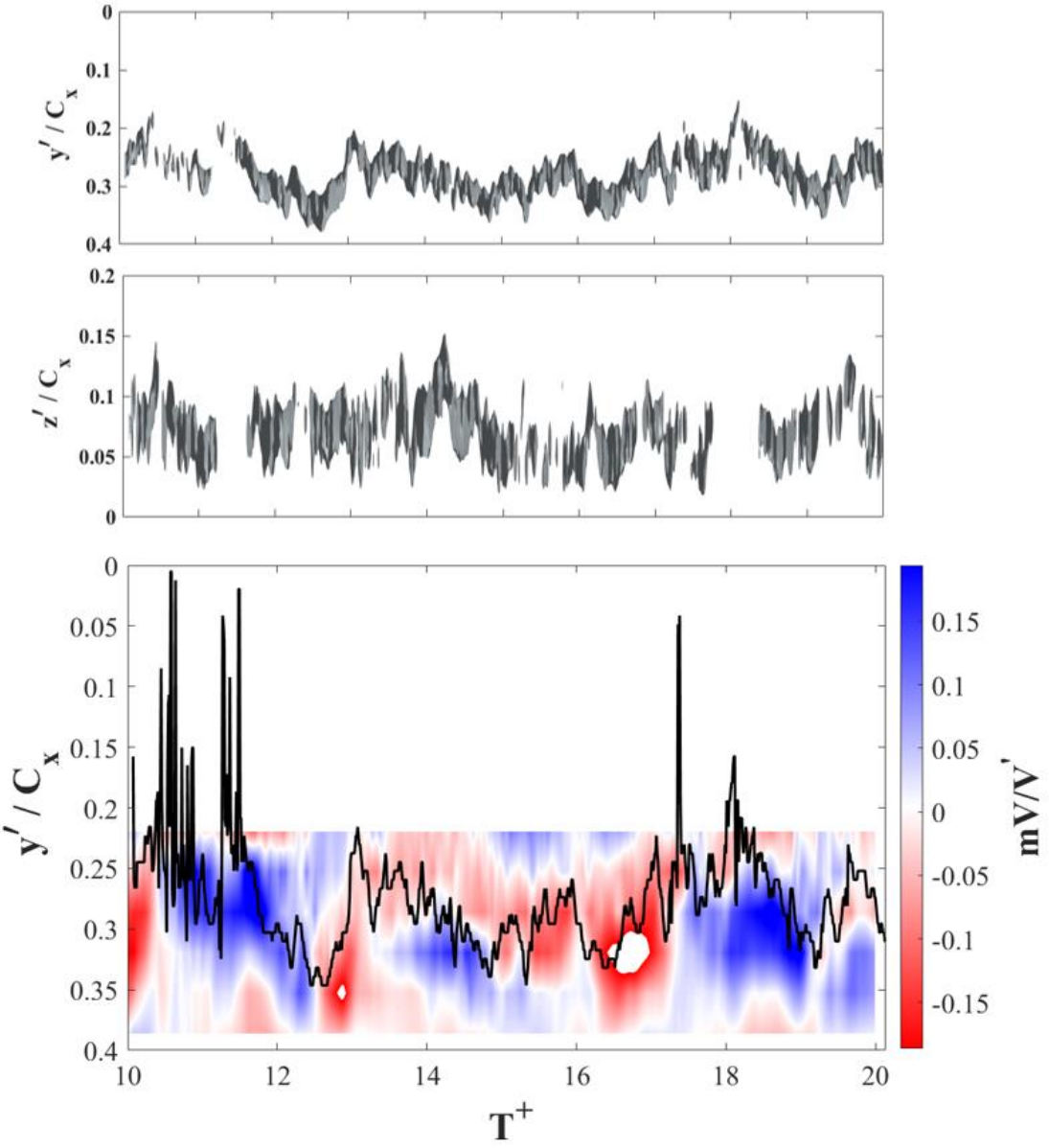

Figure 5.13 $F^{+}_{PUG} = 0$ baseline case results for a) surface-mounted hot-film results with the location of maximum Q-criterion plotted as a black line, b) space-time plot of Q=100 isosurfaces showing the PV location in the spanwise direction, and c) in the pitchwise direction

When the maximum Q-criterion suddenly jumps far towards the SS, this typically coincides with the PV temporarily losing coherence and is largely reflected in the hot-film measurement by large positive regions of filtered voltage measurements across multiple

sensors. Positive voltage readings for the hot-films sensors are connected to an increase velocity/fluid dynamic behavior near the sensor. When the PV loses coherence, the hot-film sensors detect lower levels of heat transfer representing changes in the fluid characteristics near these sensors. Figure 5.13b shows the PV lifting off the endwall at $T^+ = 14$, and Figure 5.13c shows the hot-film sensors detected a slightly higher than average concentration of positive mV/V'. There were concerns about how the hot-film sensors would respond when the PV lifted further off the endwall region, and these results show the sensors respond similarly to a loss of coherence event with a smaller magnitude.

Similar results were generated for the $F_{PUG}^+ = 0.85$ large case, and they are shown in Figure 5.14. These plots capture the same behavior shown by Figure 5.13 in the $F_{PUG}^+ = 0$ baseline case. Two clear loss of coherence events occur during this time frame (at $T^+ = 72$ and 77), with a potential third example at $T^+ = 75$. For the clear loss of coherence events, multiple hot-film sensors measured elevated voltages. The third example of a loss of coherence event may be artificial and created from the post-processing techniques since the PV only briefly loses coherence before briefly regaining it. Lower than average voltage readings were measured across all hot-film sensors during this time frame, which suggest a reduction in fluid velocity in the region near these sensors. When the PV lifted off the endwall at $T^+ = 71$, more hot-film sensors read a negative voltage, and, as the PV lowers towards the endwall, more sensors begin reading positive voltages. This response differs from the behavior captured by Figure 5.13 As the PV lowers towards the endwall, it intermittently loses coherence, which may be responsible for the change in readings.

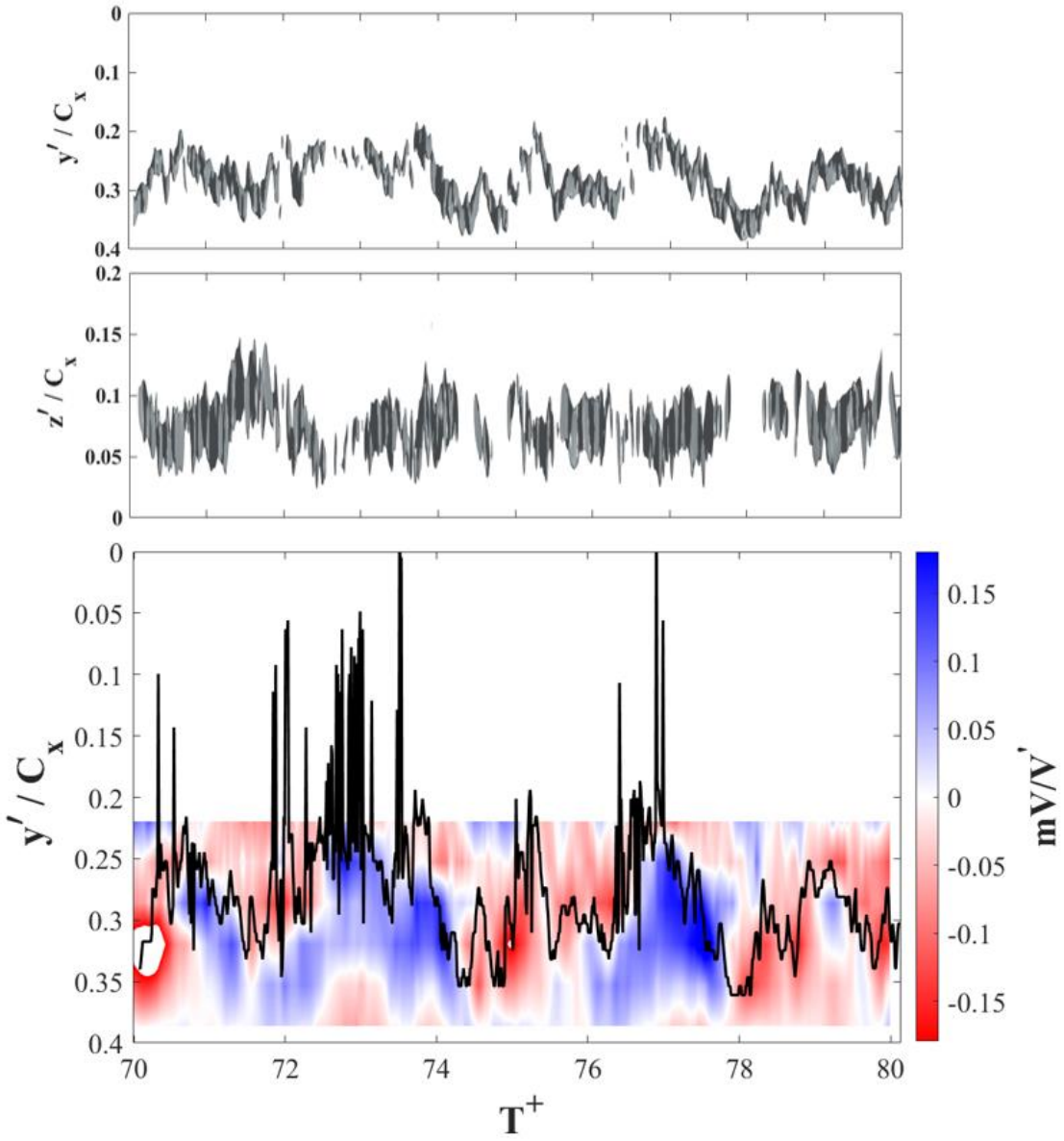

Figure 5.14 $F^{+}_{PUG} = 0.85$ large case results for a) surface-mounted hot-film results with the location of maximum Q-criterion plotted as a black line, b) space-time plot of Q=100 isosurfaces showing the PV location in the spanwise direction, and c) in the pitchwise direction

At the pulsing frequency of 1.25, the resulting plot looks similar to Figures 5.13 and 5.14. During periods when the PV loses coherence, the majority of the hot-film sensors read higher than voltages. Periods of PV coherency show largely negative voltage readings that signifies a reduction in the heat transfer from the sensor to the fluid representing changes in the fluid behavior near the sensors. When the PV lifts off the endwall, the hot-

film sensors show a minor, inconsistent change suggesting little to no correlation between the sensors and this event. The surface-mounted hot-film sensors do appear successful in identifying loss of coherence events, and they suggest the velocity close to the endwall increases during these events.

6 Conclusion

6.1 Upstream Characterization

An upstream plane of 2D2C PIV was used to verify that current PUG installation was similar to previous research analysis. This plane was also used to identify hardware settings for the PUG that produced a small and large disturbance case at frequencies of 0.41, 0.85, and 1.25. Small disturbance cases were characterized by a solenoid on-time of 0.15, and a maximum velocity deficit at $x/C_x = -0.3$ of 0.15. Large disturbance cases were characterized by a solenoid on-time of 0.4, and a maximum velocity deficit at $x/C_x = -0.3$ of 0.3. By investigating a small and large disturbance cases, more information was gathered regarding how characteristics of the disturbance influenced the behavior of the PV. Each pulsing frequency and disturbance size was characterized using single phase ensemble averaged results, and multiphase analysis. Single phase measurements showed high-fidelity results for analyzing certain phases as the disturbance propagates toward the LE of nondimensionalized velocity, vorticity, incidence angle, turbulence intensity, and V'. Multiphase measurements yielded a space-time of those same quantities at $x/C_x = -0.1$. For the large disturbance cases, pulsing frequencies greater than or equal to 0.85

increased the FSTI and did not allow any time for the flow at LE to recover between disturbances. At $F_{PUG}^{+} = 0.41$ large case, the LE flow had close to two convective times to recover from the disturbances. The small disturbance cases offered a much more subtle approach at changing the secondary flow characteristics with a smaller impact on velocity, turbulence intensity, and spanwise vorticity. These disturbances did not reach as close to the LE as the large cases, but they still offered insight into how a disturbance propagating into the passage close to the SS will change the secondary flow behavior.

6.2 Endwall Flow Study

High-speed SPIV data was taken in the passage of the cascade to analyze the endwall vortex unsteady response. The $F_{PUG}^{+} = 0.85$ large disturbance case and both cases for $F_{PUG}^{+} = 1.25$ caused minor shifts in the time averaged position of vortex core. Only the large disturbance cases caused a substantial shift in the time averaged strength of the PV. Spectral analysis of the velocity field for the baseline case showed how erratically the vortex behaves. These results were also used in conjunction with vortex tracking code to visualize the vortex phenomena associated with some of the frequencies present in PSD plots for the maximum Q-criterion. This analysis helped show that the vortex undulates from the PS to the SS back to the PS over convective time periods of about 2-2.5, which may be responsible for the common peak in PSD at $F^{+} = 0.41$. The shift in the vortex from the PS to SS typically caused a loss of coherence event, but other events appeared erratically with no clear trend or indicating factor in the behavior. The undulation appeared to occur in succession two or three times, which can be linked to frequencies of 0.2-0.3. At the $F_{PUG}^{+} = 0.41$ large case, the disturbance caused a slight increase in the frequency of loss of coherence events occurring and decrease in the duration of these events. The $F_{PUG}^{+} =$

0.85 large disturbance case appeared to substantially increase the frequency of loss of coherence events occurring and slightly increase the duration of these events. This case substantially increased the total time period that the PV was incoherent, but it did not exhibit any lock-on behavior. The $F_{PUG}^{+} = 1.25$ large case increased the frequency of loss of coherence events occurring, but the PV was incoherent for shorter total duration of time compared to the $F_{PUG}^{+} = 0.85$ large case. Pulsing at $F_{PUG}^{+} \geq 0.85$ caused the PV to have no phase-dependence on the disturbance period, which may indicate these frequencies created a steady-like effect increasing the free-stream turbulence intensity causing this behavior. In the end, none of the frequencies and disturbance size combinations caused the vortex loss of coherence events to lock-on to the periodic disturbance frequency, but they did impact the behavior and/or strength of the vortex in some capacity.

6.3 Surface-Mounted Hot-films

Surface-mounted hot-films were installed in two locations inside the linear cascade: upstream of the LE and downstream of the SPIV plane. The upstream row of sensors captured data in the junction flow region that included a bimodal distribution of PSD closest to the LE. Downstream of the SPIV plane, these hot-film sensors observed the PV behavior, and their results largely agreed with the SPIV analysis performed using maximum Q-criterion to generate PSD plots. With sensors upstream of the LE and in the passage, cross correlation analysis was performed that determined the velocity in this region is $0.9U_{\infty}$ for the $F_{PUG}^{+} = 0$ case. The cross-correlation results $F_{PUG}^{+} = 0.85$ yielded an endwall velocity around $0.75U_{\infty}$, but these results were heavily influenced by the pulsing frequency. The $F_{PUG}^{+} = 1.25$ case had a velocity of $0.5U_{\infty}$, which is likely caused by the high-pulsing frequency. Simultaneous SPIV and hot-film measurements were taken

that successfully demonstrated the hot-film's ability to capture loss of coherence events in the PV. When the PV, the majority of hot-film sensors would read high voltages that suggest elevated fluid dynamic activity in the region.

6.4 Future Work

The surface-mounted hot-films have many applications in experimental research. They can be attached to the blade to analyze flow along the LE, PS, or SS in an effort to capture the fluid dynamic flow here. Additionally, the data produced from these sensors are not fully understood yet. The results included in Section 5 offer an approach at using the data produced from these sensors to characterize the baseline case and compare its results to including periodic disturbances upstream of the LE. Further analyzing these signals can help understand the relationship between the LE junction and the secondary flow behavior.

Further investigations with the PUG focusing on midspan analysis can yield important information. High-lift front-loaded blade geometries like the L2F are supposed to have superior MS performance but increased endwall losses. Verifying these results while testing in an unsteady flow environment would be beneficial. Performing a similar study analyzing the MS flow could also yield interesting results that may provide further insight on the influence of upstream periodic unsteadiness on LPT performance.

Investigating how the disturbance changes the behavior and characteristics of the incoming BL could yield useful knowledge. Other studies have linked characteristics of the incoming BL to the strength of the PV. Understanding how the disturbance influences the BL can verify/contradict existing results. Hotfilms, boundary layer probes, and

traverses can be used to investigate how disturbances change the size of the boundary layer near the LE.

Appendix A

2D2C Image Count Convergence Study

When taking the 2D2C single-phase and multiphase data, the number of images used in the ensemble average needed to provide good quality data had. For the single-phase image acquisition, camera RAM did not meaningfully limit the number of images taken that could be acquired for each phase, however, for large multiphase datasets, data storage capacity was a factor. For the multiphase image acquisition, disc space was a significant concern, and it greatly limited the number of images that could be ensemble averaged for each phase. Capturing fewer phases would allow for a larger number of images used in the ensemble average, but it would limit the amount of information gained. The amount of time between each phase would increase, which would cause any space-time plots or videos to appear disjointed and could potentially miss important dynamics.

In this study, 2,500 images were captured for $F_{PUG}^{+} = 0.41$, DC=25, $p_{tank} = 45$ psia, and at $t/T_{PUG} = 0.78$. This case was previously used in research conducted in the lab [20]. This case, it produces a larger disturbance with a larger impact on velocity, turbulence intensity, spanwise vorticity, and incidence angle than the cases used for this paper. Using DaVis 8.4, the post-processing feature was used to average 20, 100, 300, 600, 1,000, 1,500, 2,000, and 2,500 images for the same set of images. This allowed for a clear and direct comparison of the quality the three quantities examined: velocity magnitude, turbulence intensity, and incidence angle (incidence angle). All three of these values were used to compare and analyze each of the disturbances. Spanwise vorticity was not included in this analysis because minor differences in the magnitude caused large percent difference results that limit the effectiveness of analyzing this data. Figure A.1 shows a contour plot of the

entire measurement plane with the required number of images to have the percent error less than 1% for velocity magnitude and incidence angle, and 5% for turbulence intensity. For the percent error calculation, the exact result was assumed to be the values computed with 2,500 images ensemble averaged. Velocity magnitude and incidence angle had a reasonable spread for a percent error of 1, but the turbulence intensity was heavily dependent upon the number of images used. This dependence caused the difference between 2,000 and 2,500 images to be greater than 1%.

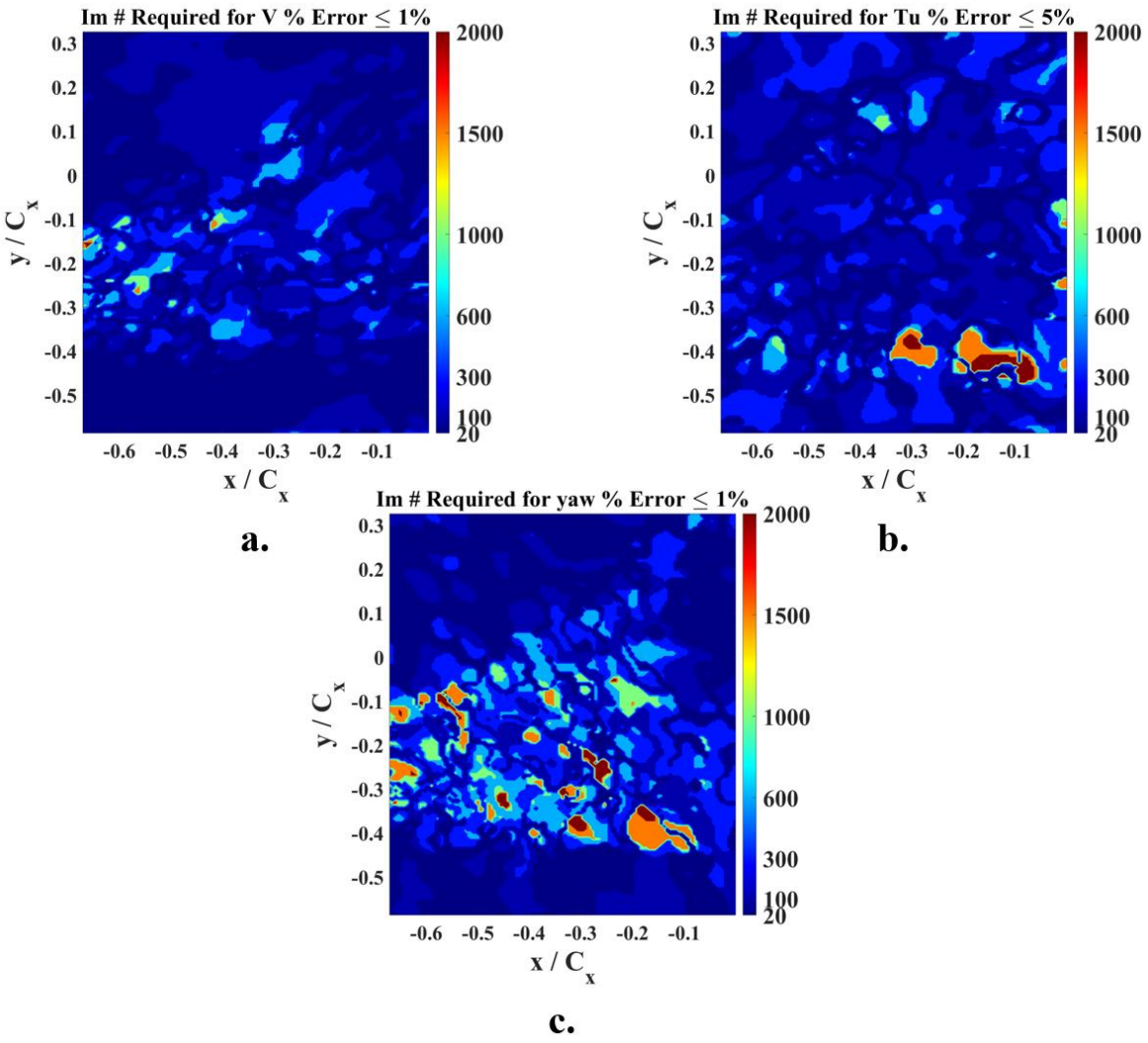

Figure A.1 Number of images required for a) percent error of velocity magnitude to be lower 1 than 1%, b) percent error of turbulence intensity to be lower than 5%, and c) percent error of incidence angle (incidence angle) to be lower than 1%

Figure A.1 is useful for identifying areas with high variation in the computed velocity magnitude, turbulence intensity, or incidence angle. These areas are heavily reliant on the number of images averaged to determine its computed value, which is either a product of high variation for that quantity (found to be true for turbulence intensity), or is caused by the flow behavior in that region. The latter is true for the velocity magnitude value. In the region just downstream of the PUG and in its profile wake required more images to achieve the percent error threshold than regions far away from those locations.

The profile wake, disturbance, and TE jets caused the seeding particles in this region to move fewer pixels than in any other region. For the turbulence intensity, Figure A.1b shows the turbulence intensity can achieve percent errors of less than 5% for most image count, except for the region $y/C_x = -0.4$ and $-0.3 \leq x/C_x \leq -0.1$. This region captures the end of the disturbance, but it largely avoids the influence on velocity, turbulence intensity, spanwise vorticity. Additionally, the pixel shift in this region is the desired amount of eight pixels between successive images. Figure A.1c shows a sporadic result for the number of images required for the percent error of incidence angle to be less than 1%. It appears that the region in the profile wake of the PUG or that encompasses the region where the disturbance passes through caused substantial variation in the number of images required to maintain that percent error threshold. The PUG and the disturbance do cause the pixel shift in this region to vary, with most of the region have a lower pixel shift, but the region below $y/C_x \leq -0.3$ saw some increase in pixel shift. Incidence angle was the only parameter with substantial regions requiring more than 600 images to meet the percent error threshold of 1%. Velocity magnitude and turbulence intensity showed that most of the plane would produce consistent results with 100 images.

Figure A.2 shows the percent error computed for 100 images ensemble averaged of velocity magnitude, turbulence intensity, and incidence angle. Figure A.2a and A.2c show that the velocity magnitude and incidence angle are both fairly accurate across the majority of the PIV plane, except in the region just downstream of the PUG. The turbulence intensity shows large percent errors sporadically in the plane.

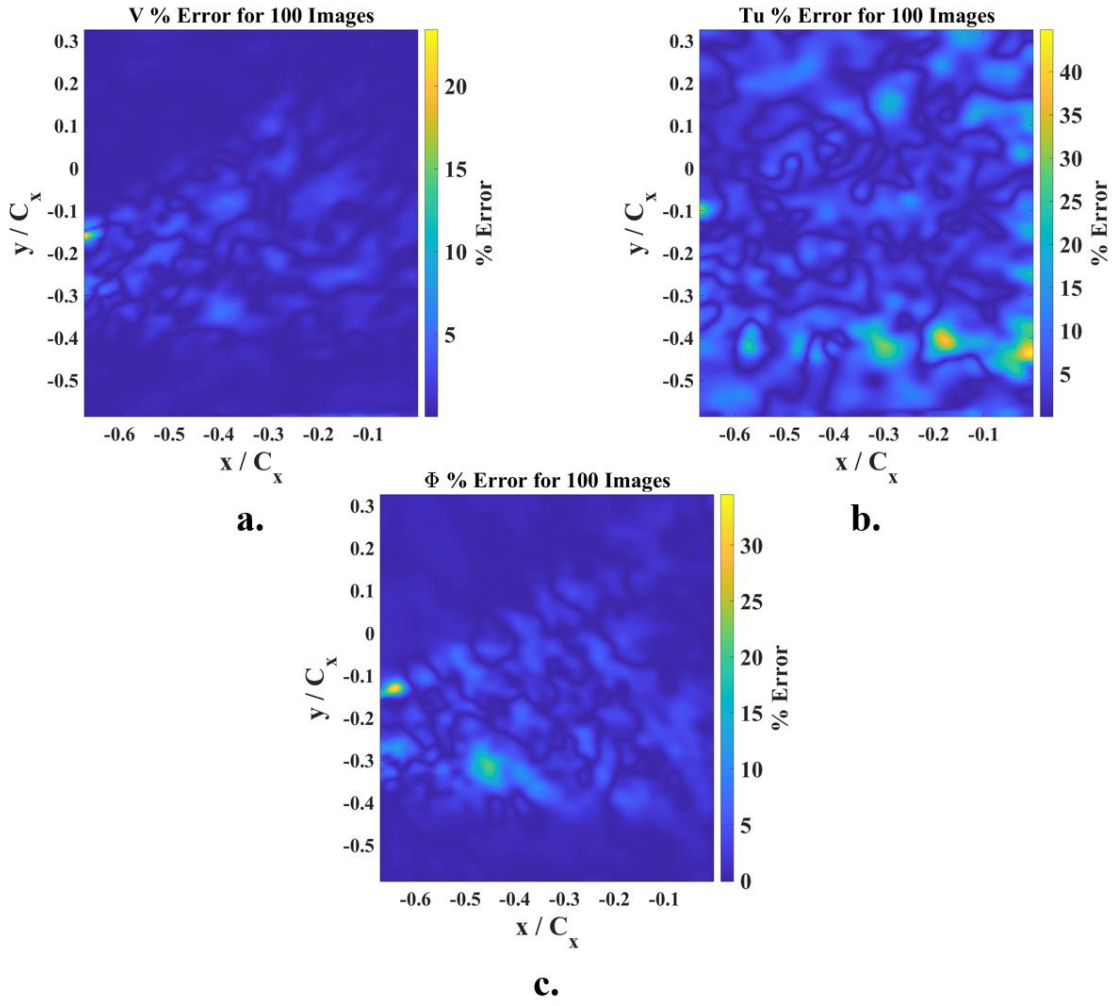

Figure A.2 Percent error of a) velocity magnitude, b) turbulence intensity, and c) incidence angle for 100 images captured

Figure A.3 shows the percent error computed for 2,000 images ensemble averaged of velocity magnitude, turbulence intensity, and incidence angle. It is important to note that he colorbar axis limits changed when comparing the percent error for 100 versus 2,000 images. The percent errors for all three components were all less than 5% error, with the velocity magnitude percent error be less than 1%. Turbulence intensity did show the most variation out of the three parameters, with random pockets of large percent errors. Velocity magnitude and incidence angle all had low percent errors with the PUG and disturbance heavily influencing these values.

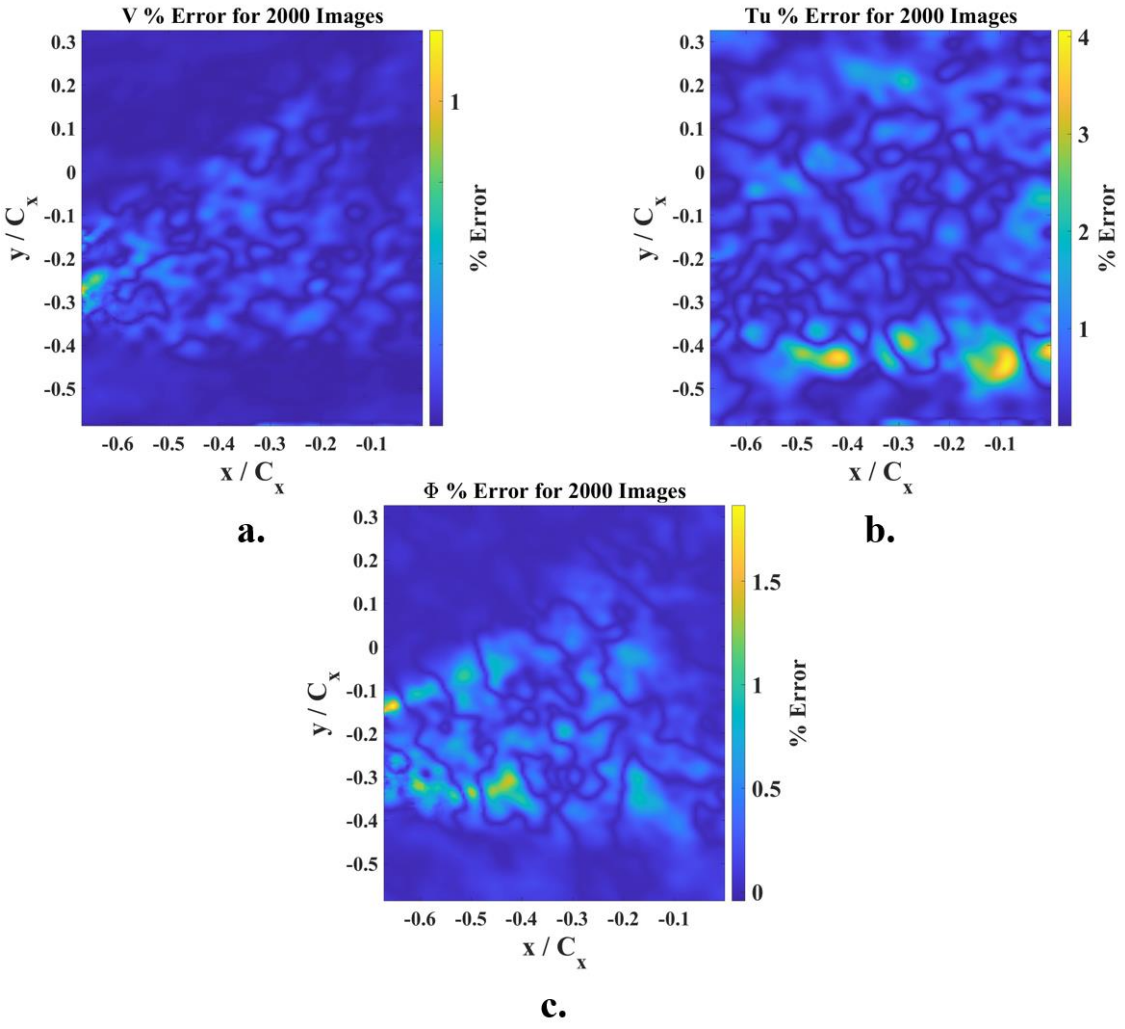

Figure A.3 Percent error of a) velocity magnitude, b) turbulence intensity, and c) incidence angle for 2,000 images captured

For the single-phase ensemble averaged, the line at $x/C_x = -0.3$ was heavily used for determining hardware settings and characterizing the disturbance. Each image set was plotted along this line for the three standard parameters: nondimensionalized velocity, turbulence intensity, and incidence angle. Figure A.4 shows these line plots for each image sample size. Besides the twenty and one-hundred image set, the majority all the other image sets match almost exactly along the line. The one-hundred image set does match the 2,500 image set for the majority of the line for all three quantities, but it deviates slightly for turbulence intensity and incidence angle. In the single-phase measurements, 2,000 images

were gathered for this analysis, and the 2,000 image set exactly matches the 2,500 image set. Therefore, the analysis performed along $x/C_x = -0.3$ where 2,000 images were ensemble averaged is not influenced by the number of images gathered.

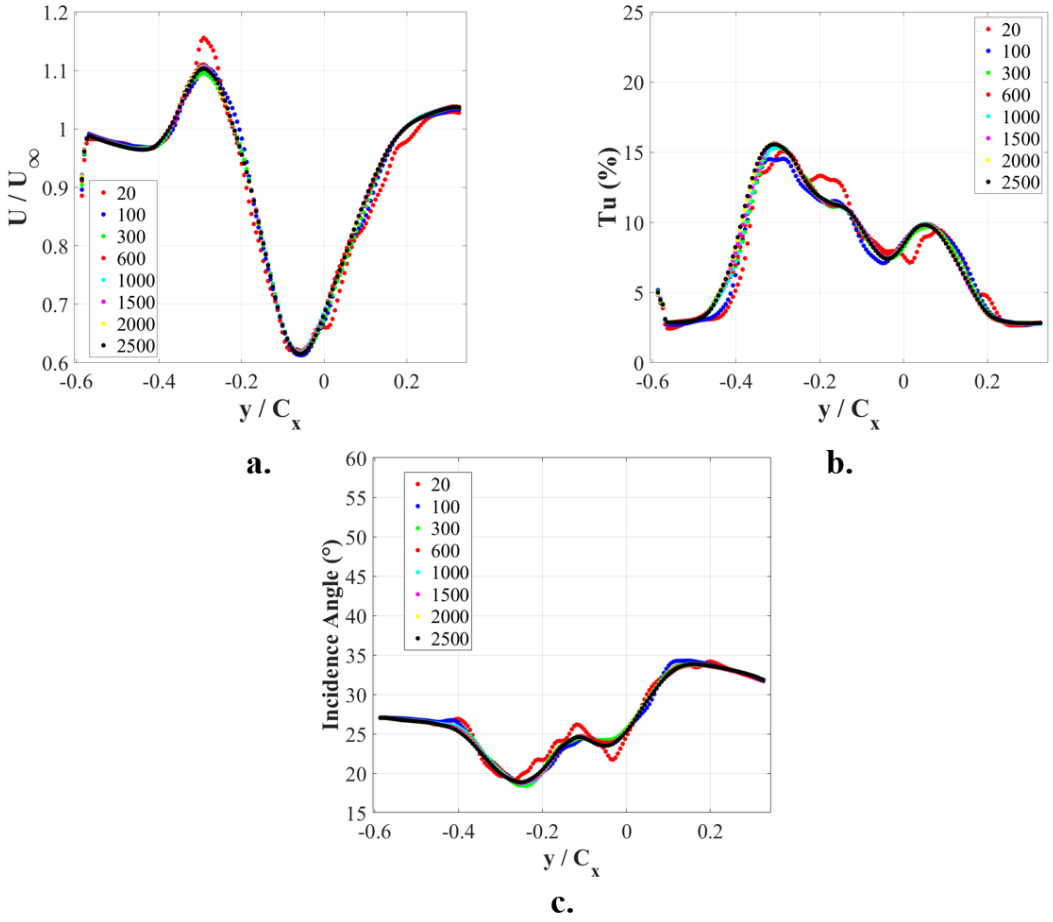

Figure A.4 Number of images comparison at $x/C_x = -0.3$ for a) nondimensionalized velocity, b) turbulence intensity, and c) incidence angle

For the multiphase data sets, the line at $x/C_x = -0.1$ was heavily used for this analysis. The space-time data and plots were both generated using the data gathered along this line, which is why the influence on the number of images gathered per phase is studied here. This line is substantially closer to the LE, which might explain why even the 300 image set showed some slight deviation from the 2,500 image set. The large velocity

gradient interacting with the disturbance requires additional images to help resolve the velocity and turbulence values here. In the multiphase data analysis, 100 images per phase were captured due to storage limitations. This analysis does show some variation between the 100 image set and the 2,500 image set primarily in the nondimensionalized velocity and turbulence intensity measurements. The majority of y/C_x locations show these two image sets matching closely, but at $y/C_x = -0.2$ Figure A.5a shows the nondimensionalized velocity measurement show some deviation. Additionally, at $y/C_x = -0.2, 0, 0.1,$ and 0.25 the turbulence intensity deviates between these two cases. Fortunately, the magnitude along each line still remains very close even where the 100 image set deviates the most from the 2,500 image set.

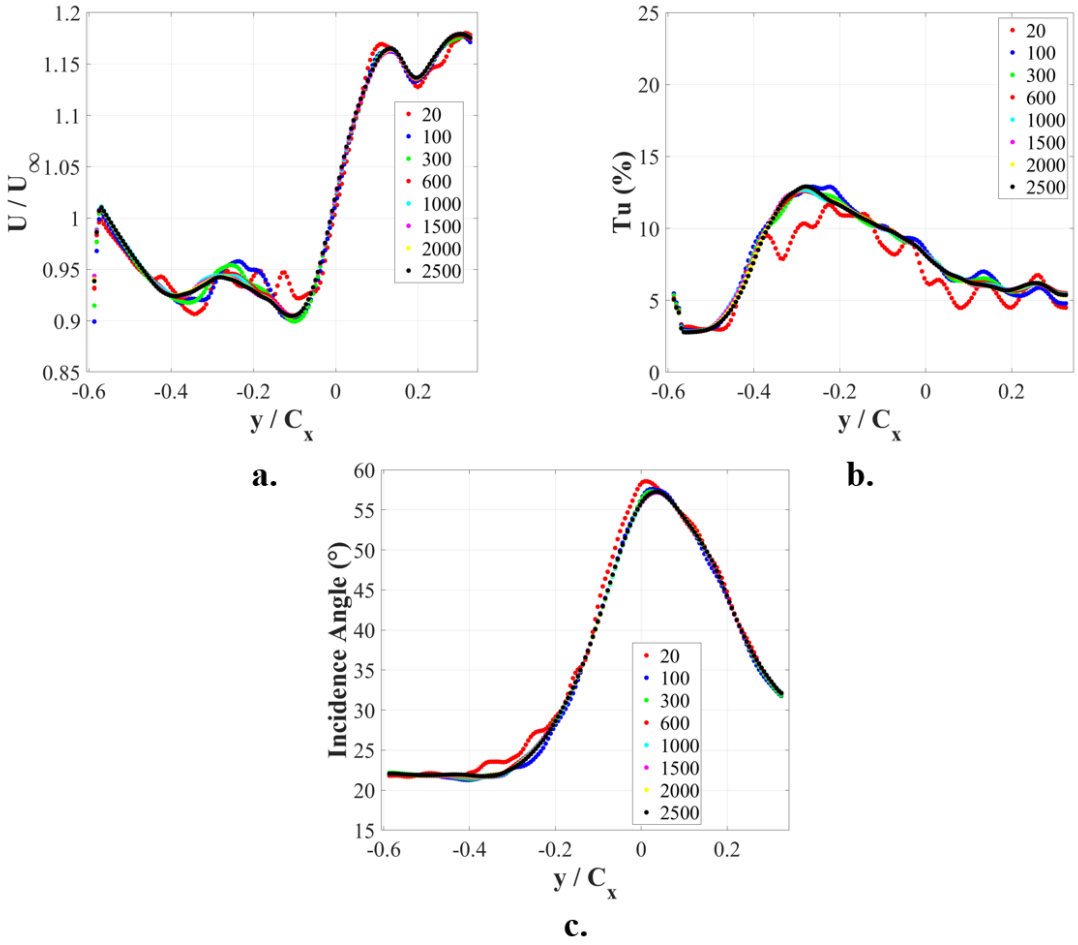

Figure A.5 Number of images comparison at $x/C_x = -0.1$ for a) nondimensionalized velocity, b) turbulence intensity, and c) incidence angle

Appendix B

Hotwire Comparison with 2D2C PIV Measurement

A hotfilm or a hotwire probe uses thermal anemometry to measure one, two, or three-dimensional velocity data. Thermal anemometry relates changes in heat transfer from a small, electrically heated element, to the velocity of the fluid's flow around the element. In most cases, a known constant voltage is placed across the wire with a measured current to create a constant temperature across the hotfilm. As a fluid flows across the hotfilm, it extracts heat that requires additional current to maintain the constant temperature. A calibration establishes how a change in current relates to a change in velocity by using an energy balance.

To check the accuracy of the 2D2C PIV measurement taken upstream of the LE, a hotfilm was used. The hotfilm used was a 1210-20 with SN of 021044. This hotfilm is a general-purpose probe used for one-dimensional flow measurements with a regular diameter of probe body closest to the sensor of 3.2 mm. The maximum exposure temperature of the probe body is 150°C. It was connected using a hotwire probe holder and a 30 ft TSI BNC cable joined by a BNC union connected to 15 ft TSI BNC cable to Channel 1 Probe of TSI IFA 300. The IFA 300 is connected to an NI SCXI-1305 DAQ card by a TSI BNC cable, and the card is installed in an NI PXI 1052 chassis daisy-chained to a NI PXIe-1078 chassis. These two chassis are daisy-chained by a PXI-8364 DAQ card connected by an ethernet cord where the PXIe-1078 is the master and the PXI-1078 is the

slave in the configuration. Both chassis and their associated DAQ cards are accessible from the main computer via an ethernet cord using LabVIEW.

The hotfilm sensor was mounted in the tunnel coming from downstream of the LE, through the passage, and located in the 2D2C PIV plane. The film portion of the hotfilm was located at $x'/C_x = -0.414$ and $y'/C_x = -0.417$ aligned vertically so that its center is the same distance above the endwall as the PIV plane: $z/H = 0.089$. This position was chosen to be far away from the LE to be within a steady flow close to the freestream velocity measured by the pitot static probe. Figure B.1a shows the probe holder positioned downstream of the blade set, and Figure B.1b shows a closeup view of the hotfilm.

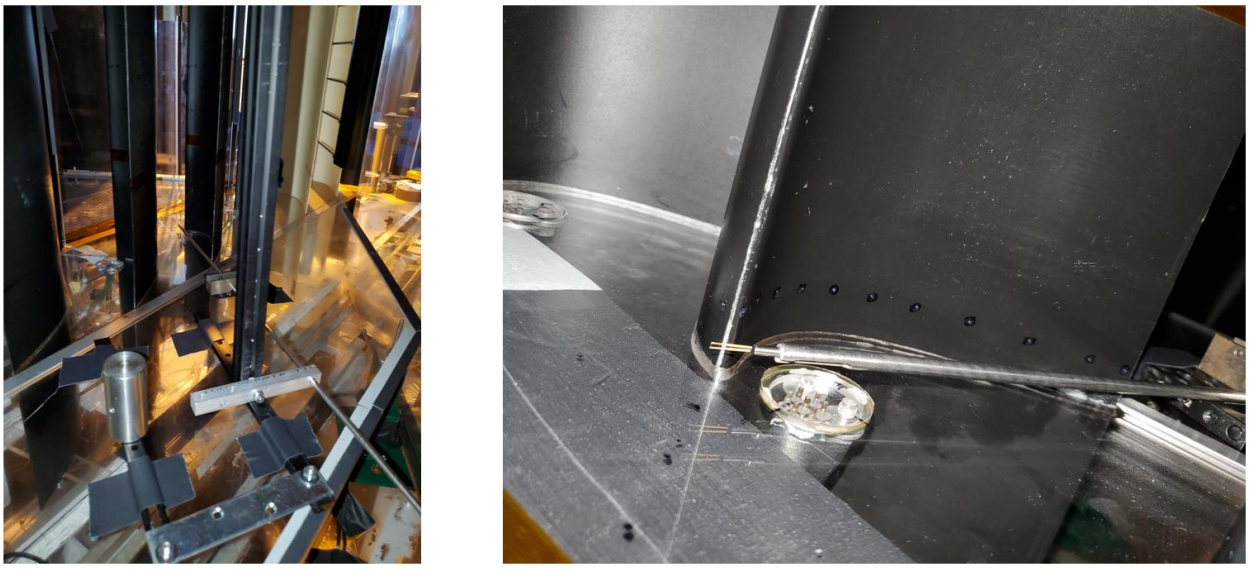

a. **b.**

Figure B.1Hotfilm a) probe holder location downstream of the blades through the passage with the probe just ahead of the LE at approximate a 60° angle relative to the flow and b) a closeup view of the hotfilm ahead of the LE in the PIV plane oriented so that the film portion is vertical to provide optimal velocity readings

The calibration process for a hotfilm used a TSI velocity calibrator with pressure transducer that allows the user to place the hotfilm over a 10 mm nozzle. A type J thermocouple and 0.0625-inch pressure tubing connected to a -0.2-0.8 inch H_2O GE

pressure druck placed upstream of the nozzle's outlet provides reference readings for the calibration. The temperature of the inlet air is crucial since heat transfer analysis is used here to develop the relations. The pressure readings are used to determine the velocity of the air stream by using Bernoulli's equation, shown by Equation B.1. The reference port of the pressure druck is connected to the static pressure port of the velocity calibrator, and the measurement port of the pressure druck is connected to the total pressure port. Total pressure represents the static pressure plus the dynamic pressure, where the dynamic pressure is the term containing velocity in Bernoulli's equation: $0.5\rho V^2$. Therefore, the resulting measurement would just contain the velocity and density. Density can be calculated using the ideal gas equation shown by Equation B.2.

$$P_1 + 0.5\rho V_1^2 + \rho g h_1 = P_2 + +0.5\rho V_2^2 + \rho g h_2 \tag{B.1}$$

$$\rho = \frac{P}{RT} \tag{B.2}$$

The hotfilm sensor was calibrated at an angle of 60° to account for its position in the tunnel. The velocity points used for the calibration were 0.5, 1.0, 1.5, 2.0, 3.0, 4.0, 4.5, 5.0, 5.5, 6.0, 7.0, 8.0, 9.0, 10.0, 11.0, 12.0, and 13.0 m/s. These points were restricted to a range of low values because the measured freestream velocity of previous runs were hovering around 5-5.5 m/s. Being close to the endwall, the velocity value is likely close to the or lower than the free-stream value, which means that calibrating the sensor in a small range around the expected readings should improve its accuracy. The resulting calibration coefficients are $C = 1.76472$ and $D = 1.56116$ with a mean-square error of $1.12 \cdot 10^{-3}$.

2D2C PIV measurements were taken with the probe holder in its position, but the hotfilm was retracted into the probe holder to avoid any potential damage the laser might

cause the sensor. Figure B.2 shows the resulting nondimensionalized velocity contour plot produced from the PIV measurement. The hotfilm probe is marked by the large red dot, and the nearest PIV data point was marked with a smaller blue dot. These two points appear almost exactly on top of each other, and they are located in a region with a minor velocity gradient. Therefore, the points not being exactly the same should have a minor impact on the results. Please notice that the probe holder did have an impact on the flow in the plane, lowering the velocity magnitude around the probe holder.

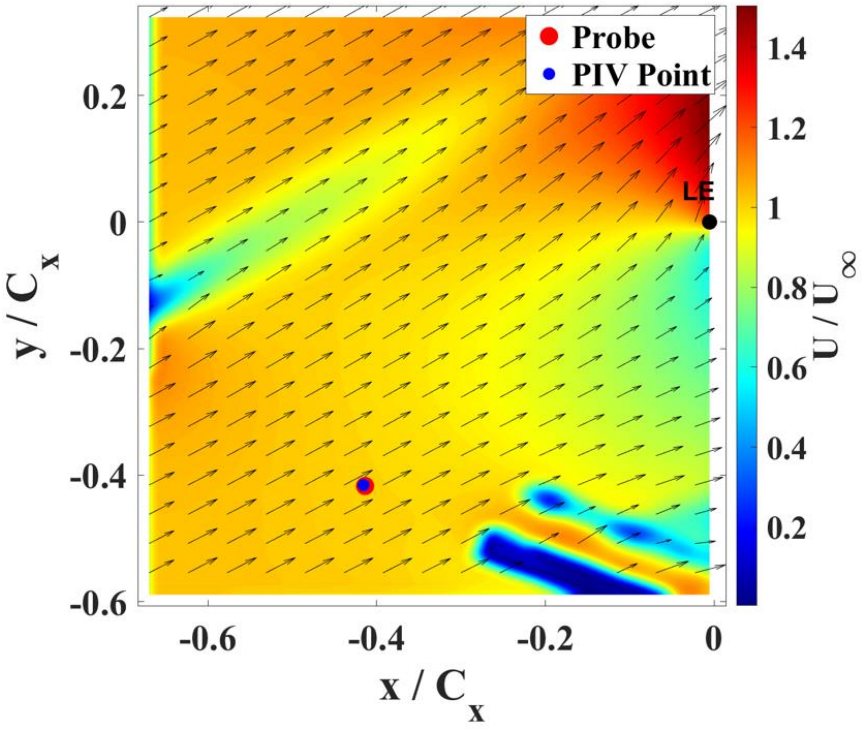

Figure B.2 Nondimensionalized velocity contour of 2D2C PIV taken with the hotfilm probe holder installed showing the hotfilm probe location and accompanying nearest PIV point

Ten sets of hotfilm data were taken over the span of two days with the data taken at varying times throughout the day. Some sets of data were taken within the same run as others to verify consistency from the hotfilm. At the start of each run, the hotfilm was re-zeroed to account for the any difference in temperature compared to the calibration. The calibration was used to convert the voltage measurement received from the TSI IFA 300

to a velocity measurement. The hotfilm was sampled at a rate of 10 kHz for 10 seconds to acquire 100,000 samples, which were all averaged to produce a single velocity reading at this point. Since the PUG's LE jets were turned off and the hotfilm probe was sufficiently far away from the PUG's profile wake and the LE, it should capture a value close to the freestream measurement computed from the pitot static probe. This offered quick verification that the hotfilm sensor was reading accurate measurements, and the values were always close. All measurements were nondimensionalized with the freestream velocity calculated based off the pitot static probe to allow for an accurate comparison. As the temperature, pressure, relative humidity, or other characteristics of the air in the experimental facility changed between runs, the variable speed motor controlling the fan close to the outlet of the linear cascade adjusts the freestream velocity to maintain a consistent Reynolds number of 50,000. Nondimensionalizing the velocity measurements eliminates differences caused by maintaining a consistent Reynolds number for testing, and, since the localized velocity is proportional to the freestream velocity, two data points gathered at different freestream velocities can be accurately compared. The percent error of the PIV measurements was computed by assuming the hotfilm measurements as the exact result. This calculation was performed for the nondimensionalized velocity and turbulence intensity.

Five measurements were taken one day that was sunny and clear skies, and five measurements were taken the next day where it rained all day. On day one, two measurements were taken in the same run (the wind tunnel was not turned off) with the TE jets of the PUG set to 17 psia, and the LE jets were turned off. For this measurement, new PIV data was not taken with the probe holder installed in the tunnel. The

nondimensionalized velocity percent error was consistently around 4.9%, but the percent difference in turbulence intensity ranged from 0.2 to 4.9%. After the tunnel was turned off and 30 minutes had passed, the tunnel was restarted and set to a Reynolds number of 50,000. For this run and the remaining runs, the PUG TE and LE jets were both off. Three data sets were taken during this run with all three percent errors of the nondimensionalized velocities consistently around 4.6%, but the percent difference in turbulence intensity ranged from 2-5%. The following rainy morning, the tunnel was set to a Reynolds number of 50,000 and the PUG LE and TE jets were both left off. Three data sets were collected during this run, and, later in the day, two more data sets at the same conditions. All five measurements showed an average percent error for nondimensionalized velocity of 7%, but the average percent error was consistently around 1-2%.

These results draw a link between the weather and the accuracy of the measurement. On the day with clear skies, the velocity measurement of the hotfilm was consistently closer to the velocity measurement of the PIV, but the turbulence intensity measurement was further apart and less consistent. When the weather changed to humid and raining, the velocity measurement was consistently further apart, but the turbulence intensity was consistently close to the PIV calculation. Except for turbulence on the first day, the measurements were all consistent for both velocity and turbulence for each day but differed from one day to another. This could be caused by the substantial change in weather, or another stimulus may have the caused the change in accuracy of either the hotfilm or the PIV.

Appendix C

Verification the Disturbance Penetrates into the BL

Previous work has identified the significant role the boundary layer plays in the strength of the PV. Justifying that the disturbance penetrates into the BL helps validate that these disturbances should produce a noticeable impact on the PV. In order to verify that the disturbance penetrates into the BL, the same hotfilm configuration described in Appendix B was used, except the location of the hotfilm. It was moved to $x/C_x = -0.260$, $y/C_x = -0.0825$, and $z/\delta_{BL} = 0.57$ with the same calibration, probe holder, BNC cables, and channel on the IFA 300. Data was collected with each PUG setting to evaluate if the acquired hotfilm data produced any noticeable peak at the same frequency as the actuation frequency of the PUG. For this experiment, the hotfilm was sampled at a rate of 10 kHz for 10 seconds producing 100,000 data points. This signal was split into four Hamming windows and then Welch's method was used to produce PSD plots. Figure C.1 shows these plots just for the $F_{PUG}^{+} = 0.41$ small and large cases because the other disturbance cases yielded similar results. The large case shown by Figure C.1b shows a clear peak at the PUG actuation frequency, but the small case shows only a band of frequencies centered around the actuation frequency. The small disturbance has a smaller impact on the velocity, turbulence intensity, and spanwise vorticity around the LE, which might explain the differences seen.

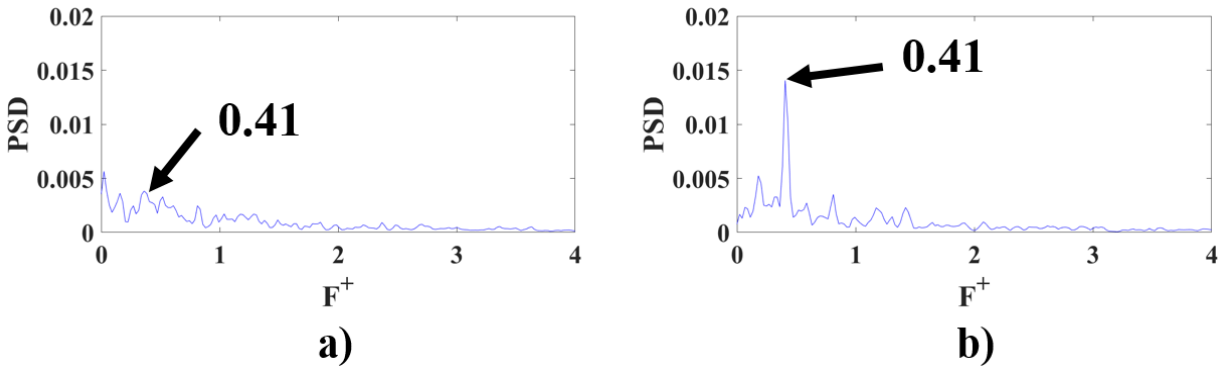

Figure C.1 PSD of the hotfilm at $x/C_x = -0.260$, $y/C_x = -0.0825$, and $z/\delta_{BL} = 0.57$ for $F^+_{PUG} = 0.41$ a) small and b) large disturbance cases

To evaluate if the frequency band is not a product of the PUG, but naturally occurs in this area, the baseline case ($F^+_{PUG} = 0$ with just the TE jets on) was also captured. These results are shown in Figure C.2, which reveals two peaks at $F^+ = 0.36$ and 0.47, but there is a noticeable dip at $F^+ = 0.41$. Therefore, the peak at $F^+ = 0.41$ in Figure C.2a, does appear to be a product of the disturbance produced by the PUG. The same process was repeated for the other small cases, and they all yielded the same result: they are penetrating into the BL, but their impact is considerably smaller and less noticeable by the hotfilm when compared to the large cases.

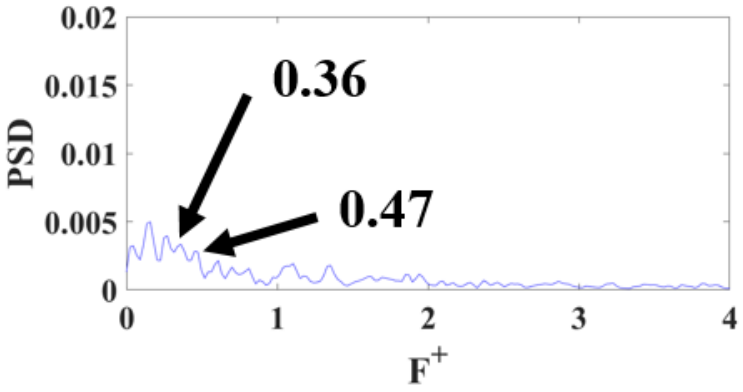

Figure C. 2 PSD of hotfilm at $x/C_x = -0.260$, $y/C_x = -0.0825$, and $z/\delta_{BL} = 0.57$ for $F^+_{PUG} = 0$ baseline case

This analysis shows that the disturbance penetrates into the BL upstream of the LE. It does not quantify or make any discernable description of how the BL flow changes because of the disturbance. The study is limited to analyzing a PSD plot from a hotfilm at $z/\delta_{BL} = 0.57$ close to the line $x/C_x = -0.3$ at the projected LE location in the plane. The hot-films also can be used to verify these results as they are located along the endwall. Their results closely matched the results presented here when analyzing sensor EW2c (the one closest to the LE), and they were discussed in Section 5.1.

References

[1] Curtis, E. M., Hodson, H. P., Banieghbal, M. R., Denton, J. D., Howell, R. J., and Harvey, N. W., “Development of blade profiles for low-pressure turbine applications,” Journal of Turbomachinery, Vol. 119, No. 3, 1997, pp. 531-538.

[2] Miao, X., Zhang, Q., Wang, L., Jiang, H. and Qi, H., "Application of riblets on turbine blade endwall secondary flow control." Journal of Propulsion and Power, Vol. 31, No. 6, 2015, pp.1578-1585.

[3] Ingram, G., Gregory-Smith, D. and Harvey, N., "Investigation of a novel secondary flow feature in a turbine cascade with end wall profiling." Journal of Turbomachinery, Vol. 127, No. 1, 2005, pp. 209-214.

[4] Aunapu, N., Volino, R., Flack, K., and Stoddard, R., "Secondary flow measurements in a turbine passage with endwall flow modification." Journal of Turbomachinery, Vol. 122, No. 4, 2000, pp. 651-658.

[5] Simpson, R. L., “Junction flows,” Annual Review of Fluid Mechanics, Vol. 33, No. 1, 2001, pp. 415-443.

[6] Devenport, W. J. and Simpson, R. L., “Time-dependent and time-averaged turbulence structure near the nose of a wing-body junction,” Journal of Fluid Mechanics, Vol. 210, 1990, pp. 23-55.

[7] Praisner, T. J. and Smith, C. R., “The dynamics of the horseshoe vortex and associated endwall heat transfer—Part I: Temporal behavior,” Journal of Turbomachinery, Vol. 128, No. 4, 2006, pp. 747-754.

[8] Paik, J., Escauriaza, C., and Sotiropoulos, F., "On the bimodal dynamics of the turbulent horseshoe vortex system in a wingbody junction," Physics of Fluids, Vol. 19, No. 4, 2007, pp. 045107.

[9] Gross, A., Marks, C. R., and Sondergaard, R., "Numerical Investigation of Low-Pressure Turbine Junction Flow," AIAA Journal, 2017, pp. 3617-3621.

[10] Hodson, H. P. and Howell, R. J., "Bladerow interactions, transition, and high-lift aerofoils in low-pressure turbines," Annu. Rev. Fluid Mech., Vol. 37, 2005, pp. 71-98.

[11] Murawski, C. G. and Vafai, K., "Effect of wake disturbance frequency on the secondary flow vortex structure in a turbine blade cascade," Journal of fluids engineering, Vol. 122, No. 3, 2000, pp. 606-613.

[12] Ciorciari, R., Kirik, I., and Niehuis, R., "Effects of unsteady wakes on the secondary flows in the linear T106 turbine cascade," Journal of Turbomachinery, Vol. 136, No. 9, 2014, pp. 091010.

[13] Lei, Q., Zhengping, Z., Huoxing, L., and Wei, L., 2010, "Upstream wake–secondary flow interactions in the endwall region of high-loaded turbines," Computers & Fluids, Vol. 39, No. 9, 2010, pp. 1575-1584.

[14] Sharma, O. P., Butler, T. L., Renaud, E., Millsaps Jr., K., Dring, R. P., and Joslyn, H. D., "Rotor-stator interaction in multistage axial-flow turbines," AIAA 24th Joint Propulsion Conference, 1988, pp. 3013.

[15] Blackwelder, R.F., and Kaplan, R.E., "On the wall structure of the turbulent boundary layer," Journal of Fluid Mechanics, Vol. 76, No. 1, 1976, pp. 89-112.

[16] Tardu, S. “Characteristics of single and clusters of bursting events in the inner layer,” Experiments in fluids 20, No. 2, 1995, pp. 112-124.

[17] Kim, J., “On the structure of wall-bounded turbulent flows,” The Physics of fluids 26, No. 8, 1983, pp. 2088-2097.

[18] Gross, A., & Robison, Z., “Numerical Simulations of Turbulent Junction Flow.” Fluid Dynamics Conference, 2018, pp. 3866.

[19] Lu, L.J., “Image processing of hydrogen-bubble flow visualization for quantitative evaluation of hairpin-type vortices as a flow structure of turbulent boundary layers,” Lehigh Univ., Bethlehem, PA (USA), 1988.

[20] Fletcher, N., Wolff, M., and Marks, C., "Turbine Secondary Flow Response to Upstream Periodic Unsteadiness." AIAA Scitech 2020 Forum. 2020, (p. 0834).

[21] Atsuchi, S., Tiwari, S., and Kalburgi, V., “Investigation of drag reduction on a two-dimensional circular cylinder by ejecting a jet from the rear stagnation region,” 36th AIAA Aerospace Sciences Meeting and Exhibit, 1997, pp. 674.

[22] Schumm, M., Berger, E., and Monkewitz, P. A., “Self-excited oscillations in the wake of two-dimensional bluff bodies and their control,” Journal of Fluid Mechanics, Vol. 271, 1994, pp. 17-53.

[23] Ghee, T. A. and Leishman, J. G., “Unsteady circulation control aerodynamics of a circular cylinder with periodic jet blowing,” AIAA journal, Vol. 30, No. 2, 1992, pp. 289-299.

[24] McQuilling, M.W., “Design and validation of a high-lift low-pressure turbine blade,” Ph.D. Dissertation, Wright State University, Dayton, OH, 2007.

[25] Veley, E., “Measurement of Unsteady Characteristics of Endwall Vortices Using Surface-Mounted Hot-film Sensors,” Wright State University, 2018.

[26] Donovan, M. H., Wolff, M., Marks, C. R., Sondergaard, R., and Veley, E., “Periodic Forcing of an Endwall Vortex in a Highly Loaded Low Pressure Turbine,” AIAA Scitech Forum, 2019, pp. 0621.

[27] Gross, A., Romero, S., "Numerical Investigation of Low-Pressure Turbine Stage with Unsteady Wakes." In AIAA Scitech 2020 Forum, p. 0836. 2020.

[28] Wang, H. P., Olson, S. J., Goldstein, R. J., and Eckert, E. R., “Flow visualization in a linear turbine cascade of high performance turbine blades,” *ASME 1995 International Gas Turbine and Aeroengine Congress and Exposition*, 1995, pp. V004T09A007-V004T09A007.

[29] Gross, A., Marks, C. R., Sondergaard, R., Bear, P. S., and Wolff, M., “Experimental and Numerical Characterization of Flow Through Highly Loaded Low-Pressure Turbine Cascade,” *Journal of Propulsion and Power*, Vol. 34, No. 1, 2017, pp. 27-39.

[30] Langston, L. S., “Secondary flows in axial turbines—a review,” Annals of the New York Academy of Sciences, Vol. 934, No. 1, 2001, pp. 11-26.

[31] Michelassi, V., Chen, L. W., Pichler, R., and Sandberg, R. D., “Compressible Direct Numerical Simulation of Low-Pressure Turbines—Part II: Effect of Inflow Disturbances,” Journal of Turbomachinery, Vol. 137, No. 7, 2015, pp. 071005.

[32] Volino, R. J., “Effect of unsteady wakes on boundary layer separation on a very high lift low pressure turbine airfoil,” Journal of Turbomachinery, Vol. 134, No. 1, 2012, pp. 011011.

[33] Schobeiri, M. T., Öztürk, B., and Ashpis, D. E., "Effect of reynolds number and periodic unsteady wake flow condition on boundary layer development, separation, and intermittency behavior along the suction surface of a low pressure turbine blade," Journal of Turbomachinery, Vol. 129, No. 1, 2007, pp. 92-107.

[34] Meyer, R. X., "The effect of wakes on the transient pressure and velocity distributions in turbomachines," ASME Journal Basic Engineering, Vol. 80, No. 7, 1958. pp. 1544-1552.

[35] Hodson, H., Huntsman, I., and Steele, A. B., "An Investigation of Boundary Layer Development in a Multistage LP Turbine," Journal of Turbomachinery, Vol. 116, No. 3, 1994, pp. 375–383

[36] Curtis, E. M., Hodson, H. P., Banieghbal, M. R., Denton, J. D., Howell, R. J., and Harvey, N. W., "Development of Blade Profiles for Low Pressure Turbine Applications," Journal of Turbomachinery, Vol. 119, No. 3, 1997, pp. 531–538.

[37] Prasiner, T., Grover, E., Knezevici, D. C., Popovic, I., Sjolander, S. A., Clark, J. P., and Sondergaard, R., "Toward the Expansion of LowPressure-Turbine Airfoil Design Space," Proceedings of the ASME 2008 Turbo Expo Conference, American Soc. of Mechanical Engineers Paper GT2008-27537, Fairfield, NJ, 2007

[38] LaGraff, J. E., and Ashpis, D. E. (eds.), "Minnowbrook III: 2000 Workshop on Boundary Layer Transition and Unsteady Aspects of Turbomachinery Flows," NASA Rept. CP-2001-210888, Aug. 2001.

[39] Prakash, C., Cherry, D. G., Shin, H. W., Machnaim, J., Dailey, L., Beacock, R., Halstead, D., Wadia, A. R., Guillot, S., and Ng, W. F., "Effect of Loading Level and Distribution on LPT Losses," Proceedings of the ASME 2008 Turbo Expo

Conference, American Soc. Of Mechanical Engineers Paper GT2008-50052, Fairfield, NJ, 2008.

[40] Denton, J. D. “Loss Mechanisms in Turbomachines,” Journal of Turbomachinery, Vol. 115, 1993, pp. 621-656.

[41] Sharma, O. P. and Butler T. L., “Predictions of endwall losses and secondary flows in axial flow turbine cascades,” Journal of Turbomachinery, Vol. 109, 1987, pp. 229–236.

[42] Duan, W., Qiao, W., Wei, Z., Liu, J., & Cheng, H., “The Influence of Different Endwall Contouring Locations on the Secondary Flow Losses in a Highly Loaded Low Pressure Turbine,” Turbo Expo: Power for Land, Sea, and Air, American Society of Mechanical Engineers, Vol. 51005, 2018, June, p. V02BT41A018.

[43] Ciorciari, R., Kirik, I. and Niehuis, R., “Effects of unsteady wakes on the secondary flows in the linear T106 turbine cascade,” Journal of Turbomachinery, Vol. 136, No. 9, 2014

[44] Romero Martinez, S.R. and Gross, A., “Numerical Investigation of Low-Pressure Turbine Stage with Unsteady Wakes,” AIAA Scitech 2020 Forum, 2020, p. 0836.

[45] Steurer, A., Benton, S.I. and Bons, J.P., “Effect of endwall boundary layer thickness on losses in a LPT cascade with unsteady wakes,” Turbo Expo: Power for Land, Sea, and Air, American Society of Mechanical Engineers, Vol. 45639, 2014, June, p. V02DT44A037.

[46] Lyall, M. Eric. Effects of front-loading and stagger angle on endwall losses of high lift low pressure turbine vanes. Air Force Inst of Tech Wright-Patterson Air Force

Base, Ohio, Graduate School of Engineering and Management, 2012. No. AFIT/DS/ENY/12-05.

[47] Sieverding, C. H., "Recent progress in the understanding of basic aspects of secondary flows in turbine blade passages." J. Eng. Gas Turbines Power, Vol. 107, no. 2, 1985, pp. 248-257.